A 3-dimensional kinetic particle simulation of the Martian hot coronae and upper atmosphere: mechanism, structure, variability, and atmospheric loss

by

Yuni Lee

A dissertation submitted in partial fulfillment
of the requirements for the degree of
Doctor of Philosophy
(Atmospheric, Oceanic and Space Sciences)
in the University of Michigan
2014

Doctoral Committee:

Professor Michael R. Combi, Co-Chair
Associate Research Scientist Valeriy M. Tenishev, Co-Chair
Professor Stephen W. Bougher
Professor Edward W. Larsen

"The planet was known under the name of Harmakhis in Ancient Egypt, where it was also called Har decher, that is to say the Red One, because of its colour. The Chaldaeans gave it the name of Nergal — the Babylonian Mars, the great hero, the king of conflicts, the master of battles and the champion of the gods; and the planet was known on the banks of the Euphrates under the names of Allamou and Almou.

The Greeks called it Ares (Mars), name of the God of War, and apparently it was also known sometimes as Hercules. Moreover, it was regarded as fiery and impetuous. Proclus Diadochus called it 'celestial fire', and added that it symbolised fire. The sign ♂ represents, so far as we know, the spear and shield.

The Arabs, the Persians and the Turks named it Mirikh, which signifies a torch, iron, steel, and a long arrow thrown to a great distance. It was also known in Persia under the name of Bahram and Pahlavani Siphir, or the celestial warrior.

Among the Indians Mars was called Angaraka (from angara, burning coal), and they also called it Lohitanga, the red body, from loliita, red, and anga, body. Its astrological influence was regarded as being essentially malign."

- *The Planet Mars,* E. M. Antoniadi.

사랑하는 어머니께

Acknowledgements

This dissertation would not have been possible without the tremendous encouragement and support of my thesis advisor, Prof. Michael Combi. I would like to express my deepest gratitude to his advice and constant faith in me throughout my Ph.D. study. The seeds of my interest in planetary science could be planted via an undergraduate research opportunity to work with Dr. Combi before I started my Ph.D. He has been always positive and available for any questions by sharing his vast knowledge and expertise in planetary atmosphere and computational study, which aided me to creatively think and research. Without his guidance, I would not have found this study of Mars as an extraordinarily exciting field of study.

I would like to thank my dissertation committee members, co-chair Dr. Valeriy Tenishev, Prof. Stephen Bougher, and Prof. Edward Larsen for their careful reading and valuable comments and suggestions, which helped this thesis to be completed and let my defense be an enjoyable moment.

My immeasurable appreciation for the help and support is extended to Dr. Valeriy Tenishev, who developed AMPS, the generic core code for kinetic particle simulation. His priceless advice and teaching during my Ph.D. study have deepened my knowledge and enthusiasm and have prepared me for future challenges. Had there not been his help, I would not have been able to explore all the sophisticated Martian upper atmosphere research.

I am also very grateful to Prof. Stephen Bougher, who provided the Martian thermosphere and ionosphere (MTGCM and M-GITM) for the Martian hot corona simulation. I appreciate his brilliant comments and constant support on my research. He has always willingly shared his time and knowledge, and I have always felt enlightened and motivated.

I am privileged to be part of the MAVEN team. I am extremely excited for the upcoming remote measurements that will be compared with our simulation results. I have not been able to come to this point without the support of so many people in so many ways. I would like to thank all scientists with whom I had opportunities to meet and have discussion at scientific conferences, project science group meeting, and teleconferences.

I acknowledge that all simulations in this thesis have been supported by NASA Mars Fundamental Research Program grant NNX09AL26G. Resources have been provided by the NASA High-End Computing Capability (HECC) project at NASA Advanced Supercomputing (NAS) Division.

Lastly, I would like to express my sincere appreciation to the water fountain (the one across from the Donahue Conference Room) for being very close and supplying continuous and endless hydration when I get thirsty while researching in room 2418, and to my bike and laptop for not being broken and surviving at least for ~2 years before I finish my Ph.D.

Table of Contents

List of Figures

Figure

List of Tables

Table

List of Abbreviations / Acronyms

AL	Aphelion Low solar activity
AMPS	Adaptive Mesh Particle Simulator
AMR	Adaptive Mesh Refinement
ASPERA-3	Analyser of Space Plasma and Energetic Atoms
AU	Astronomical Unit
BG	Background
BR	Branching Ratio
CM frame	Center-of-mass frame
DR	Dissociative Recombination
DSMC	Direct Simulation Monte Carlo
EL/EH	Equinox Low solar activity/Equinox High solar activity
EQE	Equatorial East
EUV/UV	Extreme Ultraviolet/Ultraviolet
FUV	Far-Ultraviolet
FW	Forward scattering
HS	Hard Sphere collision (isotropic scattering)
IR	Infrared
JPL	Jet Propulsion Laboratory
LAB frame	Laboratory frame
LMD-MGCM	Laboratoire de Météorologie Dynamique Martian General Circulation Model
L_s	Solar Longitude
LT	Local Time
LTE	Local Thermodynamic Equilibrium
M-GITM	Mars Global Ionosphere Thermosphere Model
MAVEN	Mars Atmosphere and Volatile EvolutioN
MF-MHD	3D Multifluid MHD code
MGCM	NASA Ames Mars General Circulation Model
MHD	Magnetohydrodynamics
MTGCM	Mars Thermosphere General Circulation Model
NASA	National Aeronautics and Space Administration
NCAR	National Center for Atmospheric Research
NLTE	Non - Local Thermodynamic Equilibrium
NP	North Pole
PD	Photodissociation

PL/PH	Perihelion Low solar activity/Perihelion High solar activity
RT	Radiative Transfer
SMAX	Solar maximum (high solar activity)
SMIN	Solar minimum (low solar activity)
SP	South Pole
SPICAM	Spectroscopy for Investigation of Characteristics of the Atmosphere of Mars
SWMF	Space Weather Modeling Framework
SZA	Solar Zenith Angle
$V_{threshold}$	Threshold velocity
1/2/3D	one/two/three-dimension
-MIN/-MED/-MAX	-Low/-Moderate/-High solar activity
AEQU-/VEQU-/APH-/PER-	Autumnal equinox-/Vernal equinox-/Aphelion-/Perihelion-

Abstract

A 3-dimensional kinetic particle simulation of the Martian hot coronae and upper atmosphere: mechanism, structure, variability, and atmospheric loss

by

Yuni Lee

Advisor: Professor Michael Combi

The evaluation of the global atmospheric structure, variation, and loss rate is key to a better understanding of the physics that drives the current state of the Martian atmosphere. The production of energetic particles in the Martian upper thermosphere and exosphere results in the formation of the hot coronae, where most of the escape of neutral atoms occurs. The characterization of this hot population becomes challenging and complicated, since Mars has a strongly coupled atmospheric system from the lower to upper atmospheres, which requires a description of the transition from the collision-dominated regime to the collisionless regime.

This thesis presents results of the 3D study of the Martian hot atomic coronae by introducing the significantly improved kinetic particle model, AMPS, and by coupling with the thermosphere/ionosphere model for various Martian conditions. The first comprehensive investigations of the 3D hot carbon corona are carried out by using the coupled framework linking the Mars-AMPS and MTGCM codes for different solar cycle and seasonal cases. The

first coupling of the Mars-AMPS and M-GITM codes was completed for the hot oxygen corona study. The important source mechanisms described in simulations are analyzed by studying their dependencies on the local atmospheric variations. Utilizing the solar flux and orbital parameters, the solar cycle and seasonal variations are found to influence the hot coronae in different ways, requiring both two- or three-dimensional aspects of the macroscopic parameters from a local to global perspective.

In this study of the hot carbon corona, the effects of the background atmosphere on the resulting hot carbon distribution have been examined by characterizing the local atmospheric structure and conditions. The spatial distributions of the parent molecule and ion of hot carbon are provided in comparison with the major thermospheric and ionospheric species. The oxygen distribution and the escape probability have been simulated for a wide range of the model parameters. The computed OI 1304Å brightness from our hot O corona shows both reasonable agreement and some discrepancies in comparisons with available observations. The current lack of data will be greatly alleviated by the *in situ* and remote measurements from the MAVEN mission.

Chapter I

Introduction

It is always astonishing to discover where we are. Astronomical observational evidence and the advancement of supercomputing power have provided great tools for sophisticated modeling techniques to investigate the physics behind the evolution of the universe. Modern cosmology suggests that the origin of our universe from the Big Bang dates back about 13.7 billion years, when all fundamental physical forces were united. The separation of the forces due to the rapid expansion and cooling of the universe seeded the structural evolution of the universe, which provided the basis for the formation of the first stars, galaxies, and planets. The birth of the solar system was around 4.6 billion years ago, during the process of the transformation to the present form of a highly complicated universe.

The accretion in the protosolar disk around the Sun sprouted the formation of the various planets, satellites, and small body objects in our solar system. The solar system (figure 1.1) consists of a star, the Sun, and eight planets with satellites orbiting around the Sun with many small solar system objects such as asteroids and comets. Depending on the material and physical condition around the planet formation sites at that time, the four inner planets – Mercury, Venus, the Earth, and Mars (in the order of the increasing distance from the Sun) – became the "rocky" or "terrestrial" planets, and the four outer planets – Jupiter, Saturn, Uranus, and Neptune – became the "giant" planets or the "gaseous" planets, located beyond the asteroid belt where

debris and small objects are populated like in the Kuiper belt and Oort cloud surrounding our solar system.

The solar system is surrounded by an extensive region of space, the heliosphere, which is filled with the solar wind, the streams of plasma released constantly outward from the sun. The solar wind expands radially and blows against the interstellar medium, forming a bubble-like region. At the termination shock, the solar wind abruptly slows down to subsonic speed and eventually stops at the heliopause, the theoretical boundary of our solar system. On August 25, 2012, it was reported that Voyager 1 became the first spacecraft to cross the heliopause and explore the interstellar medium.

Figure 1.1. Solar system (not to scale) (Image courtesy of NASA/JPL).

Among the eight planets, Mars is known as the 'red planet.' Orbiting the Sun at a distance of about 1.5 AU (227,000,000 km or 141 million miles), this red planet is the fourth farthest away from the Sun and the second smallest planet in the solar system. Mars is about 4.5 billion years old, about 40 million years younger than the Earth, and is a very unique planet for humans since the space exploration age has begun. This is largely due to the fact that Mars is the only planet in the solar system that has the closest habitable atmospheric condition, resembling that on the Earth. Mars also owns two small moons, Phobos and Deimos, while the Earth has one moon. Mars has a mass of about 6.4×10^{23} kg, only ~10% of the Earth, and its volume is about 15% of the Earth volume. The size of Mars at the equator is about half of the Earth (~53% of the Earth's Equatorial radius, 3396.2 km). Because of its lighter mass and smaller size, the surface gravity is only about 38% of that on the Earth, which is 3.71 m/s^2. (So, you can easily move around a 220 lb treadmill by yourself on Mars).

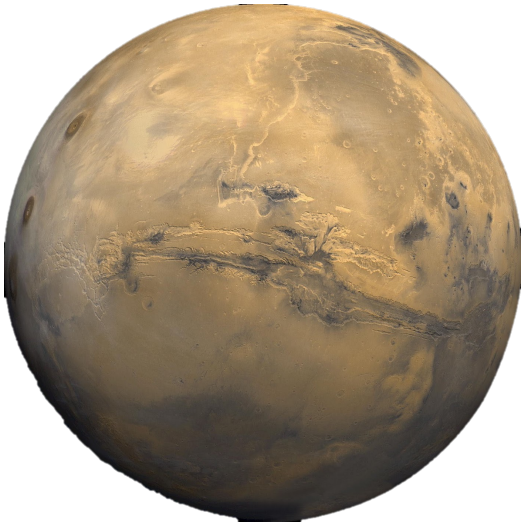

Figure 1.2. Mars. The fourth planet from the Sun and second smallest planet in the solar system.

The present Mars is cold, dry, and hostile. The surface of Mars is desert, covered with red iron-rich soil and rocks. Due to the lack of an appreciable magnetic field, Mars has a very thin atmosphere (100 times thinner than the Earth's atmosphere), composed predominantly of CO_2. Mars' orbit is the second most eccentric in the solar system, where a Mars year is about 687 earth days and 669 sols. A Mars day lasts about 24 hours and 37 minutes, which is close to that of the earth. The current axial tilt of Mars, about 25.19°, is also similar to that of the Earth, resulting in seasons on Mars (figure 1.3).

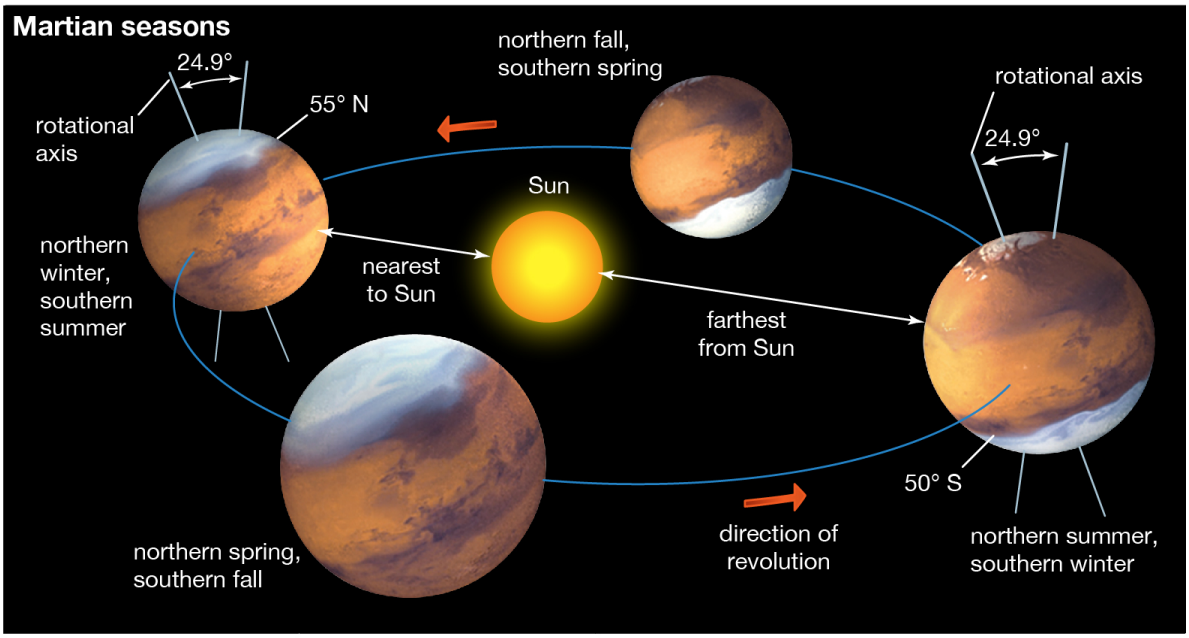

Figure 1.3 Diagram of different Martian orbital positions around the Sun. The axial tilt of the planet is about 25.19° instead of 24.9° indicated in the figure.

The total atmospheric pressure is ~6 mbar, only ~0.6% of the Earth's atmospheric pressure, and the partial pressure of water vapor in the atmosphere is about 10^{-3} mbar [*Jakosky and Phillips*, 2001]. The average atmospheric temperature is 220 – 230 K, >50 degrees below

zero Celsius globally. The surface temperature varies from region to region and from season to season. Measured by the Viking landers 1 and 2 at 1.5 m above the surface, the surface temperatures range from about -178 °F (-117 °C and 156K) to 1 °F (-17.2 °C and 256 K). The highest soil temperature estimated by Viking Orbiter was about 81 °F (27 °C and 300 K), and the lowest was about -225 °F (-143 °C and 130 K), at the winter polar cap region.

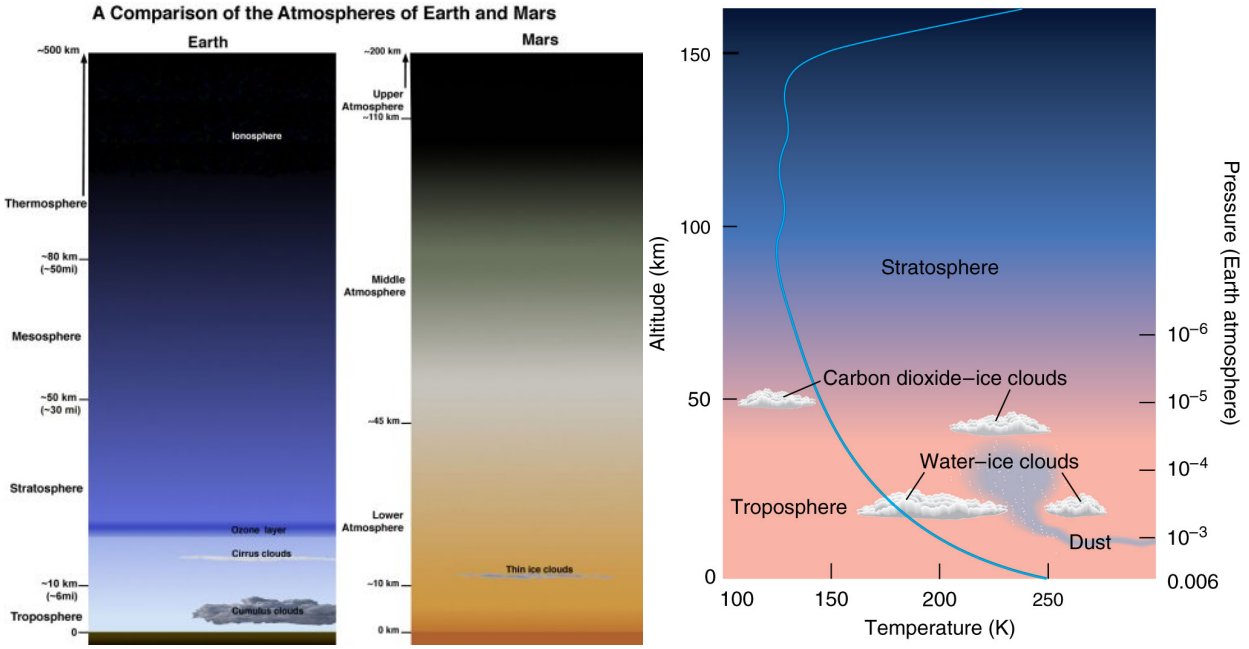

Figure 1.4. Temperature and pressure variation in the Martian atmosphere as a function of altitude. (Image courtesy Pearson Education, Inc.).

I.1. Past missions to Mars

The majority of the presently available information about the Martian upper atmospheric structure and composition was gained by the measurements from the early Mars missions of Mariner 4 (flyby) [*Kliore et al.,* 1965; *Fjeldbo et al.,* 1966]; Mariner 6, 7 (flyby), and 9 (1st orbiter) [*Strickland et al.,* 1972; *Anderson and Hord*, 1971; *Anderson,* 1974]; Viking 1 and 2 (landers) [*Hanson et al.,* 1977; *Nier and McElroy,* 1977]. In the 1990's, our understanding about

the Mars' atmospheres has significantly improved by measurements returned from the Mars Global Surveyor (MGS) [*Acuña* et al., 2008; *Bougher et al.,* 1999; *Keating et al.,* 1998] and Phobos-2 [*Rosenbauer et al.,* 1990] missions.

Aerobraking data from Mars Global Surveyor (MGS), Mars Odyssey, and Mars Reconnaissance Orbiter (MRO) allowed detailed analyses of the properties of the Martian upper atmosphere. Moreover, images with resolution higher than ever before were returned by Mars Odyssey, and Mars Express, an orbiter launched in 2003, observed the recent volcanism activity on Mars.

I.2. Past modeling efforts

Exploring the physical processes that affect the volatiles in Martian atmosphere will help provide a better understanding of the water and CO_2 inventories on Mars [*e.g.*, *Carr*, 1986; *Pepin*, 1994; *Jakosky and Jones*, 1997; *McElroy*, 1972]. Throughout the Martian history, the loss mechanisms and the escape rates of the Martian atmosphere have changed [*Chassefiére et al.*, 2007; *Luhmann*, 1992; *Melosh and Vickery*, 1989]. Observations from spacecraft and analyses of the Martian geomorphology suggest that the early Martian atmosphere was much warmer, wetter, and abundant in water and CO_2 than the current atmospheric conditions [*e.g., Chassefiére et al.*, 2007; *Jakosky,* 1991]. The current deficiency of water and CO_2 in the current atmosphere raises questions as to the processes that led to the loss of volatiles and their subsequent fate. Among several possible processes, escape of heavy neutral species by nonthermal mechanisms is posited as a significant factor in the loss on the basis of the current volatile content. Heavy species, such as atomic O and C, can escape through these nonthermal mechanisms, resulting in the formation of hot coronae in the upper atmosphere of Mars.

A number of numerical approaches have been carried out to estimate the current global escape rate of hot heavy neutral species, in particular, O [*Cipriani et al.*, 2007; *Fox and Hać*, 1997b; *Fox and Hać*, 2009; *Hodges*, 2000; *Hodges,* 2002; *Kim et al.*, 1998; *Valeille et al.*, 2009a, 2009b; *Valeille et al.*, 2010a, 2010b; *Yagi et al.*, 2012, *Fox and Hać*, 2014], C [*Cipriani et al.*, 2007; *Fox,* 2004; *Fox and Bakalian*, 2001; *Fox and Hać*, 1999; *Nagy et al.*, 2001], and N [*Bakalian*, 2006; *Fox,* 1993*; Fox and Hać*, 1997a], which are important for understanding the inventory of water, CO_2 and N_2 in an evolutionary aspect. The list of past models and their estimates of atmospheric loss is in table 1.1.

Models	Atmospheric loss (a) Escape rate (s^{-1}) / (b) Escape flux (cm^{-2} s^{-1})
O ((a) 10^{25} s^{-1})	
Hodges (2000)[a]	(a) 2.8
Hodges (2002)[b]	(a) 4.4
Krestyanikova and Shematovich (2005)[c]	(a) 0.13
Krestyanikova and Shematovich (2005)[d]	(a) 9.9
Krestyanikova and Shematovich (2005)[e]	(a) 1.3
Krestyanikova and Shematovich (2006)[f]	(a) 0.33
Krestyanikova and Shematovich (2006)[g]	(a) 0.45
Cipriani et al. (2007)	(a) 2.1
Chaufray et al. (2007)	(a) 1.0
Valeille et al. (2009)[h]	(a) 6.0
Fox and Hać (2009)[i]	(a) 0.71
Fox and Hać (2009)[j]	(a) 14.4
Yagi et al. (2012)[k]	(a) 4.7
Fox and Hać (2014)[l]	(a) 0.65
C ((a) 10^{24} s^{-1}; (b) 10^{4} cm^{-2} s^{-1})	
Fox and Hać (1999)[m]	(b) 0.19
Fox and Bakalian (2001)	(b) 2.1
Nagy et al. (2001)	(b) 5.3
Fox (2004)	(b) 11.1
Cipriani et al. (2007)[n]	(a) 0.00046

	N((b) 10^5 cm^{-2} s^{-1})
Fox (1993)	(b) 2.0
Bakalian (2006)	(b) 3.03

Table 1.1. Summary of the different neutral particle loss rates for various studies at low solar activity.

[a] Mars-L case
[b] Account for collisional quenching and excitation transfer of $O(^1D)$ and $O(^1S)$; day-only ionosphere case.
[c] Isotropic solid sphere collisions.
[d] Model A case; differential scattering cross section for elastic channels only.
[e] Model B case; differential scattering cross section for elastic and inelastic channels; includes the excitation of rotational-vibrational levels of the CO_2 molecule.
[f] Model A case; elastic and inelastic channels; without quenching O-O and O-CO_2 collisions; includes the excitation of rotational-vibrational levels of the CO_2 molecule.
[g] Model B case; elastic and inelastic channels; without quenching O-O and O-CO_2 collisions.
[h] Atmospheric input is the MTGCM (full 3D thermosphere/ionosphere model).
[i] Eroded ionosphere and isotropic case; assumes that O escape flux at SZA 60° is average over the dayside.
[j] Eroded ionosphere and forward scattering case; assumes that O escape flux at SZA 60° is the average over the dayside.
[k] Four different seasons at average solar condition are considered.
[l] Model 1, eroded.
[m] Eroded ionosphere case.
[n] Considers dissociative recombination of CO^+ only as the source of hot carbon; uses Kim atmosphere [*Kim et al.*, 1998].

I.3. Current ongoing investigation

Exosphere models have been significantly improved and have extensively investigated the source mechanisms of hot atomic species. However, the approaches so far to study the hot coronae in the atmosphere of Mars have been limited to one-dimensional numerical schemes and/or thermospheric inputs for fixed orbital positions. The processes that characterize the Martian upper thermosphere and exosphere occur deep within the thermosphere and ionosphere, where complicated local variations occur as an inevitable result of the pure 3D planetary influences. For example, asymmetries in the thermosphere/ionosphere structure, planetary

rotation, winter polar warming as well as interhemispheric dynamics [*e.g., Bougher et al.*, 2000, 2004, 2006, 2008, 2009, 2014a] have been successfully described. The upward propagating gravity waves and tides from the lower atmosphere modify the energy and momentum budgets in the upper atmosphere, changing the atmospheric circulation and horizontal distributions of atmospheric constituents. These dynamical effects have been neglected in the past 1D and 2D models. Consequently, the previous models may have over/underestimated the overall loss rate and density of hot species in the upper Martian atmosphere and hot corona. In order to overcome these limitations of the previous models, a global model with a self-consistent thermosphere-ionosphere-exosphere description is required.

A 3D simulation of the Martian hot corona and hot species in the thermosphere were performed by using our DSMC code [*Tenishev et al.,* 2008] and the 3D Mars Thermosphere General Circulation Model (MTGCM) [*Bougher et al.*, 2006, 2009]. The first application of this coupled framework was completed by a series of studies on the variation of the hot O corona with solar activities, seasons, and geologic times [*Valeille et al.,* 2009a, 2009b, 2010a, 2010b]. These studies successfully finished the first fully 3D implementation of the DSMC code.

Subsequently, our DSMC code, officially re-named the Adaptive Mesh Particle Simulator (AMPS) [*Tenishev et al.*, 2013], has been greatly improved in its numerical performance by incorporating the adaptive mesh refinement technique with cut cell methods, which utilizes a Cartesian coordinate system. This thesis started by implementing a new Mars' exosphere model into AMPS. All the physics and model parameters are incorporated in the exosphere model to investigate the Martian upper atmosphere and exosphere using the DSMC method.

The AMPS code with the Martian exosphere model (Mars-AMPS) is used to explore hot carbon with a complete 3D description for the first time. This first comprehensive investigation

of the hot C corona is conducted for studying its source mechanisms and structure [*Lee et al.,* 2014a] for the case of the equinox and low solar activity condition. In this work, we have studied the effect of source mechanisms on the spatial distribution of hot carbon. The solar cycle and annual variabilities of the hot carbon corona have been studied for two solar activity cases (low and high) and three seasonal cases (aphelion, equinox, and perihelion) [*Lee et al.*, 2014b]. The results of these works make up a significant part of this thesis and are described in Chapters 5 and 6.

Another significant part of this thesis is the revision of the hot oxygen model previously implemented by *Valeille et al.* [2009a, 2009b]. The basic physics of the Martian hot corona is enhanced and successfully incorporated into AMPS with a new thermosphere/ionosphere model, Mars Global Ionosphere Thermosphere Model (M-GITM) [*Bougher et al.,* 2014b]. This new hot oxygen model has been used in preparation for the new Mars mission, MAVEN, for which a model library is being constructed using Mars-AMPS for a complete model parameter study of hot O and intercomparison with other models. Some model parameters, such as cross sections for collision pairs, were found to be significant for determining the structure and the loss of the atmosphere. For instance, the collisions between hot and cold neutrals in the upper atmosphere is crucial for estimation of the atmospheric loss. The description of the collisions must be carefully handled by considering realistic scattering schemes and up-to-date collision cross sections.

Replacing the MTGCM,, output from the newly improved thermosphere and ionosphere model, M-GITM [*Bougher et al.,* 2014b], is incorporated into the AMPS code. M-GITM overcomes the previous limitation in the MGCM-MTGCM framework and models the whole Martian thermosphere and ionosphere from the surface to the upper atmosphere. The explicit treatment of the vertical momentum equation provides a more precise description of the localized

physics. Furthermore, the extended input domain range from M-GITM allows Mars-AMPS to capture more of the lower atmospheric features, such as the ionospheric peak of O_2^+.

For the hot O study described in this thesis, M-GITM was used to calculate the distribution of the gas in the thermosphere for a total of 12 cases, which corresponds to the combination of three solar activity levels and four seasons by utilizing the solar flux and orbital position parameters. The coupled framework of Mars-AMPS and M-GITM is able to simulate the structure of the hot corona with the selective set of model parameters. Using the combination of different solar activity and seasonal cases, the solar cycle and annual variabilities of the hot O corona and their correlation can be also investigated using the M-GITM thermosphere/ionosphere at different solar activity and seasons. Taking advantage of 3D simulations, the hot O corona simulation is performed for computing OI 1304Å brightness to compare with the measurement taken by the ALICE instrument onboard *Rosetta* [*Feldman et al.,* 2011]. The brightness has been estimated for different solar conditions and seasons for examining the variation. The simulated 12 cases of the hot O corona are successfully coupled into the Multifluid–Magnetohydrodynamics (MF-MHD) plasma model [*Dong et al.,* 2014a; *Dong et al.,* 2014b], where the initial investigation of the one-way coupling is currently completed. The AMPS code is underway for integration into the Space Weather Modeling Framework (SWMF) [*Tóth et al.,* 2012], which allows the two-way coupling between AMPS and M-GITM by exchanging information simultaneously during the simulation.

In this thesis, a 3D global approach of modeling is presented using a one-way coupling strategy linking the 3D kinetic particle simulator and 3D atmospheric models to investigate the mechanisms, structure, and variabilities of the hot neutral coronae and its loss rates. The appropriate model parameters are extensively tested and chosen to improve the description of the

hot corona. A full 3D study of the exosphere provides a detailed description of the Martian upper atmosphere and a better understanding of the Martian hot atomic coronae. The 3D MTGCM and M-GITM provide all the necessary background thermospheric/ionospheric parameters as inputs to the 3D Mars-AMPS code. Thus, the combination of the 3D thermosphere/ionosphere (MTGCM and M-GITM) and 3D Mars' exosphere kinetic particle model (Mars-AMPS) framework provides a self-consistent evaluation of the Martian hot coronae.

For both hot C and hot O, the resulting spatial distribution of hot species shows the effects that the background temperatures and global atmospheric circulation have on thermospheric/ionospheric constituents. The local production rate and local thermalization rate operate as the main source and loss of hot atoms, which are strongly dependent on the model parameters. The estimated C loss rates from the first fully 3D investigation of hot C range from about 5.2×10^{23} s^{-1} to 57.1×10^{23} s^{-1} for the aphelion and solar low case to perihelion and solar high case, showing reasonable agreement with some of the previously published model results. The hot O study has been greatly improved by adopting more realistic description of the collision between hot O and cold O and by including additional thermospheric species in the background atmosphere. The revised global escape rates of hot O now show good agreement with other model results, which are estimated to range from about 1.14×10^{25} s^{-1} to 5.18×10^{25} s^{-1}.

I.4. Outline of thesis

This first chapter provides the reviews of the past missions to Mars and past modeling efforts for the Martian hot corona and introduces current ongoing research along with the motivation of this thesis. Several important analytical classical models are reviewed in chapter 2. As a connection to the mechanisms for hot particles, the descriptions and example of the

collisions between hot particles and ambient atmosphere are given in the rest of the chapter. The descriptions of two atmospheric models are given in chapter 3, followed by the detailed description of the kinetic particle simulator. The main assumptions and methods are discussed in the last section. The mechanisms for producing hot atomic species in the Martian upper atmosphere are presented in chapter 4. Chapter 5 and 6 present the first comprehensive investigation on mechanisms and structure of the hot carbon corona and its solar cycle and seasonal variation. The descriptions of the two atmospheric models used in this thesis are presented in chapter 7, along with the improvements in the new model. The detailed study on the effects of model parameters on the hot O corona is given in chapter 8 with the newly improved hot O corona investigation with M-GITM and comparison with the ALICE/*Rosetta* measurements. The remaining topics that need to be studied utilizing the coupled framework are introduced in chapter 9 as the next step from the end of this thesis, and this thesis concludes in chapter 10.

Chapter II

Analytical models and collisions

In the classical models of the planetary atmosphere, the exospheric densities were computed by assuming a critical level, a spherically-symmetric, uniform atmosphere over the globe, and no planetary rotation. The analytical models for the planetary exosphere and corona have been extensively developed by taking various effects into account. More realistic simulations became possible by applying Monte Carlo methods. In this chapter, several analytical models will be reviewed. Some of their calculations will be used to predict the thermal O densities in the exosphere and will be compared with the results from the current sophisticated atmospheric model (M-GITM). In connection with our kinetic particle simulator, important collision mechanisms will be reviewed followed by the detailed analysis of O_{hot}-O_{cold} collisions.

II.1. Analytical (classical) models for the planetary exosphere

The density and pressure of planetary atmospheres decrease exponentially with increasing altitude. While the lower atmosphere is dominated by rigorous mixing process (about 0 – 35 km altitude in the Martian atmosphere), the upper atmosphere is characterized by a transition from the well-mixed and relatively dense atmosphere to the diffusing and rarefied atmosphere. Extending from the upper thermosphere to exosphere, the planetary corona (the planetary hot neutral corona) is a region in which atmospheric species may travel large distances

along their ballistic trajectory, undergoing very infrequent collisions with other local atmospheric species, or escape to space.

The kinetics and chemistry of hot atoms or molecules in the upper atmosphere and the hot corona region determine the overall shape and structure of the planetary corona. The hot population (suprathermal population) in the hot corona is produced deep in the thermosphere via a number of source mechanisms. Heavy neutral species, such as O, C, and N, can form this hot corona only from nonthermal mechanisms. The shape of the hot corona formed by these hot populations has a spheroid shape that is elongated toward North and South Pole. In the hot corona, the particles may fall back toward the planet, due to the lack of energy to overcome the planet's gravitational attraction, or may escape the planet's atmosphere by attaining energy exceeding the escape energy.

Nascent particles produced from nonthermal mechanisms in the thermosphere can encounter numerous collisions with other atmospheric constituents. Some of them can reach a level of altitude, at which the scale height of the atmosphere becomes about the same as the mean free path. Classical models defined this level of altitude as the 'exobase,' a theoretical abrupt boundary between a collision-dominated regime, the thermosphere, and a collisionless regime, the exosphere or hot corona. In the region above this exobase, the exosphere, the density of the atmosphere is so low that particles move along their ballistic trajectories in the planet's gravitational field without any interaction with ambient atmosphere. The Knudsen number, K_n, the ratio between the mean free path and the scale height of the atmosphere, theoretically determines the altitude of the exobase, where $K_n \sim 1$. Analytical classical models of the Martian atmosphere assume that collisions above the exobase are entirely absent and treat the distribution

of atmospheric constituents below the exobase as a complete Maxwellian velocity distribution, which is a highly collisional region [*e.g., Öpik and Singer*, 1959; *Chamberlain,* 1963].

The classical models of the planetary hot corona [*e.g., Öpik and Singer*, 1959, 1961; *Chamberlain,* 1963; *Hagenbuch and Hartle*, 1969] developed a theory for a simple exosphere model with spherical symmetry. The simplest classical model had a non-rotating uniform atmosphere over the globe with a collisionless region above a critical level, which is designated within the model. The exospheric density of the specific species was computed by integrating the velocity distribution of the species at the critical level below which the atmosphere remains highly collisional. These simple models were improved by extending to 2D and 3D and taking into account various planetary effects, such as a non-uniform atmosphere, planetary rotation, and transitional domain. In following sections, previous classical models are described and revisited by comparing the exospheric oxygen densities calculated from the models' application to the Martian atmosphere.

II.1.1. Simple model

Before the advent of computing power, classical theoretical models were developed to estimate density in the planetary exosphere and coronae. Classical models [*e.g., Öpik and Singer*, 1959; *Herring and Kyle,* 1961] computed exospheric neutral density distributions using various assumptions. The simplest type of classical model was derived by utilizing the idealized physical conditions. The main assumption for the idealized conditions is a sharp transition level, the "critical level," below which the gas velocity distribution is a complete isotropic Maxwellian distribution and above there are no collisions. The complete collisionless assumption is used for the region above the base of the exosphere, since the collisions between constituents are

extremely infrequent. *Öpik and Singer* [1959] assumed that the particles at the base of the exosphere are distributed according to a truncated Maxwellian distribution, where there are particles with velocities exceeding the escape speed. The modeled atmosphere (1-dimension) was assumed to have no latitudinal / longitudinal and diurnal effects, no rotation, and a spherically symmetric structure over the globe; there is no azimuthal bulk motion.

Many theoretical studies [*e.g., Chamberlain,* 1963; *Herring and Kyle,* 1961] have estimated the exospheric densities by directly using Liouville's theorem. This is a fundamental theorem that describes the conservation of particle distribution function in phase space in Hamiltonian mechanics. According to this theorem, the density and momentum distributions of particles, $f(\boldsymbol{r}, \boldsymbol{v})$, remains constant along the dynamical trajectories of particles, which can be expressed as,

$$f(\boldsymbol{r}, \boldsymbol{v}) = f(\boldsymbol{r_c}, \boldsymbol{v_c}). \tag{2.1}$$

In this formulation, $f(\boldsymbol{r}, \boldsymbol{v})$ represents the velocity distribution function where a particle has the speed $\boldsymbol{v}$ at radial position $\boldsymbol{r}$. The same particle posses the speed $\boldsymbol{v_c}$ at the critical level, $\boldsymbol{r_c}$, which is basically a radial position on the base of the exosphere. From the conservation of energy and angular momentum, one can obtain the following relations,

$$v_c^2 - v^2 = \frac{2MG}{r_c}(1 - y) = 2g(r_c)r_c(1 - y), \tag{2.2}$$

$$v = \sqrt{v_c^2 - \frac{2MG}{r_c}(1 - y)}, \tag{2.3}$$

$$\frac{v \sin\theta}{y} = v_c \sin\theta_c, \tag{2.4}$$

where M, G, and $g(r_c)$ are the mass of the planet, the gravitational constant, and the gravitational acceleration at the critical level, respectively. θ and θ_c, the traveled angle, are measured from the radius vector at the position of a particle, and $y = r_c/r$ (figure 2.1).

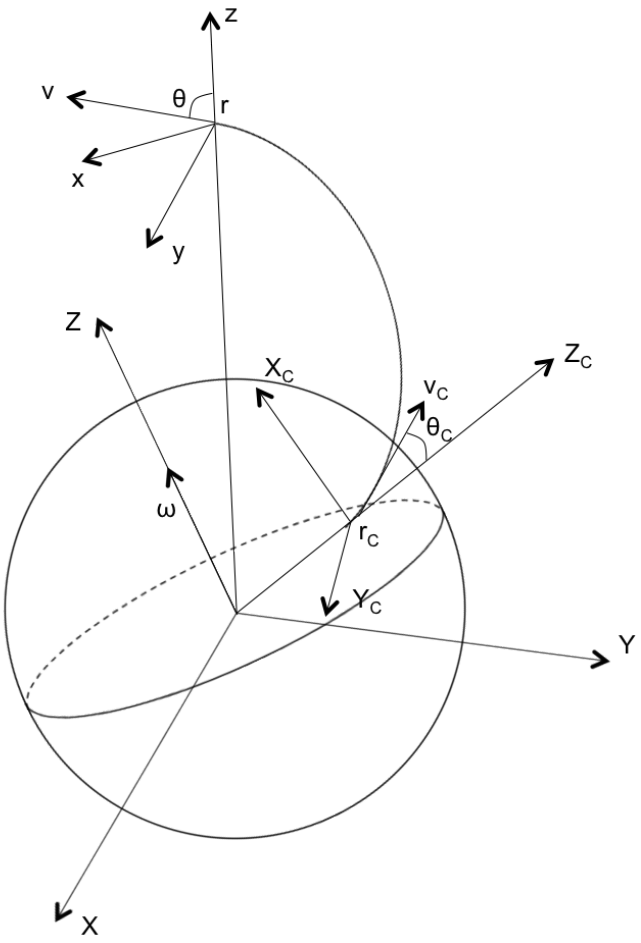

Figure 2.1. Illustration of the geometry of a particle moving from a position $\mathbf{r}_C$ at the critical level (exobase) to a position **r** in the exosphere. This diagram is the reproduction of figure 1 in *Kim and Son* [2000] with appropriate labels for this study.

Following the derivation by *Herring and Kyle* [1961], the Martian exospheric oxygen density is numerically computed. *Herring and Kyle* [1961]'s formulation is based on Liouville's theorem. They calculated the density of particles traveled from the base of the exosphere and integrated the density profiles to obtain the depth of the exosphere. The spatial density is found to be,

$$\rho(r) = y^2 \int f(\boldsymbol{R}, \boldsymbol{v_0}) \frac{v_0^3 \cos\theta_0 \sin\theta_0 d\theta_0 dv_0}{\sqrt{v_0^2(1 - y^2 \sin^2\theta_0) - \frac{2MG}{R}(1 - y)}} \,. \tag{2.5}$$

Equation 2.5 (equation 6 in *Herring and Kyle* [1961]'s study) shows the integral that calculates the spatial density, $\rho(r)$, is equal to the equation 12 in the study of *Öpik and Singer* [1959] if $f(\boldsymbol{r_c}, \boldsymbol{v_c})$ is replaced by a truncated Maxwellian distribution**.** For the Martian exospheric oxygen, the thermal oxygen density at 200 km from M-GITM is chosen for the density of oxygen at the critical level. Since the model formulation is based on the assumption of a one-dimensional isotropic atmosphere, the chosen critical level density is extracted at solar zenith angle (SZA) of 60° on the equator, where the density at this location can serve as an average over the dayside atmosphere.

II.1.2. Chamberlain model

A model developed by *Chamberlain* [1963] classified the exospheric density by three types: (a) ballistic orbits, (b) satellite orbits, and (c) escaping orbits. The *Chamberlain model* also assumes the idealized physical condition as in previous simple models and examines the particle trajectory to investigate the exospheric density precisely. The term *planetary corona* was first used by this model to specifically represent the portion of a planetary atmosphere above the critical level. The critical level was also treated importantly to describe the altitude at which collisions vanish.

Important mechanics considered for the spatial and momentum distribution of particles is addressed in Liouville's theorem. The distribution function of particles at any height is expressed by the Hamiltonian,

$$f(r, p_r, P_\chi) = \frac{N_C e^{-(\lambda_C - \lambda)} e^{-v_r^2/2MkT_C} e^{-P_\chi^2/2MkT_C r^2}}{(2\pi MkT_C)^{3/2}},$$

(2.6)

where r is distance measured from the center of the planet, and p_r and P_χ are the radial and angular component of momentum, respectively. The subscription *C* indicates the corresponding values at the critical level. T and λ are the neutral temperature and the gravitational potential energy, GMm/kTr (M = the planetary mass; m = the atomic mass), respectively. After performing the integration over all phase space for equation 2.6, the density $N(r)$ is expressed by introducing a partition function, $\zeta(\lambda)$,

$$N(r) = N_C e^{-(\lambda_C - \lambda)} \zeta(\lambda). \tag{2.7}$$

This partition function is used to describe the specific orbit of particles in the absence of collisions in the planetary exosphere, where the total partition function is addressed as,

$$\zeta = \zeta_{bal} + \zeta_{sat} + \zeta_{esc}. \tag{2.8}$$

ζ_{bal} describes the particles with ballistic orbits, which travel from the critical level in their elliptic orbits and fall back to the base of the exosphere. The expression of ζ_{bal} is,

$$\zeta_{bal} = \frac{2}{\pi^{1/2}} \left[\gamma\left(\frac{3}{2}, \lambda\right) - \frac{(\lambda_C^2 - \lambda^2)^{1/2}}{\lambda_C} e^{-\psi_1} \gamma\left(\frac{3}{2}, \lambda - \psi_1\right) \right],$$

(2.9)

where

$$\psi_1 = \frac{\lambda^2}{\lambda + \lambda_C}, \tag{2.10}$$

and γ is the incomplete Γ function, which is given by,

$$\gamma(\alpha, x) \equiv \int_0^x y^{\alpha-1} e^{-y} dy. \tag{2.11}$$

Also, ζ_{sat} represents the satellite orbits of particles that remain only in the satellite orbits, and it is given by,

$$\zeta_{sat} = \frac{2}{\pi^{1/2}} \frac{(\lambda_C^2 - \lambda^2)^{1/2}}{\lambda_C} e^{-\psi_1} \gamma\left(\frac{3}{2}, \lambda - \psi_1\right). \tag{2.12}$$

The satellite orbits are not often considered in the theoretical estimation due to the assumption of complete absence of collisions above the critical level (*i.e.,* particles never intersect the critical level).

Lastly, ζ_{esc} describes the particles that escape from the boundary of the exosphere,

$$\zeta_{esc} = \frac{1}{\pi^{1/2}} \left\{ \Gamma\left(\frac{3}{2}\right) - \gamma\left(\frac{3}{2}, \lambda\right) - \frac{(\lambda_C^2 - \lambda^2)^{\frac{1}{2}}}{\lambda_C} e^{-\psi_1} \left[\Gamma\left(\frac{3}{2}\right) - \gamma\left(\frac{3}{2}, \lambda - \psi_1\right) \right] \right\}, \tag{2.13}$$

where $\Gamma(\alpha) \equiv \gamma(\alpha, \infty)$ is the complete Γ function.

Figure 2.1 shows the estimated spatial densities of the Martian exospheric oxygen, as computed by performing the integration in the *Herring and Kyle* [1961] and *Chamberlain* [1963] models. Given the density of SZA 60° thermal O at an altitude of 200 km from M-GITM at autumnal equinox and solar low activity, the Chamberlain model estimates the O density that matches with the M-GITM O density for an altitude range of 200 km – 500 km, where the result by Herring and Kyle model shows some deviation from the others.

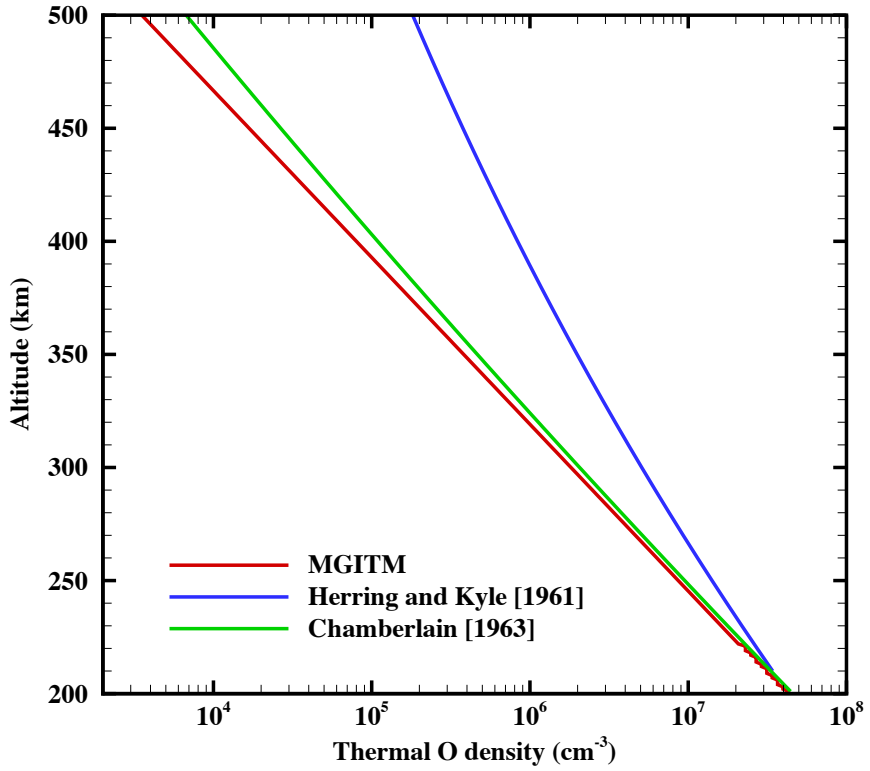

Figure 2.2. Thermal O densities estimated by using *Chamberlain* [1963] model (green) and *Herring and Kyle* [1961] model (blue). Thermal O density extracted at SZA 60° (equatorial east) at autumnal equinox and solar low activity condition modeled by M-GITM (red) is plotted together for comparison purpose.

II.1.3. Addition of the planetary rotation

Planetary exosphere models became more sophisticated and capable of implementing more realistic descriptions. The simplest form of the classical models dramatically improved on the description of the mechanics in the exosphere by considering various effects: rotation of the model atmosphere below the base of the exosphere at constant angular velocity (*i.e.,* the planet + atmosphere below the critical level) [*Hagenbuch and Hartle*, 1969; *Hartle*, 1971; *Kim and Son,* 2000], non-uniform atmospheric structure (2D and 3D) [*Vidal-Madjar and Bertaux,* 1972], non-

uniform exobase condition [*Vidal-Madjar and Bertaux,* 1972], and thermospheric winds [*Hartle and Mayr*, 1976]. Today, increases in computing power and resources make it possible to use the Monte Carlo method, which is the numerical approach most widely used for the planetary corona simulations.

II.2. Collision mechanisms

Collisions are key kinematics in the planetary thermosphere and exosphere. Immediately after the production, a hot particle moves through the ambient atmosphere and can exchange momentum and energy with other atmospheric particles in collisions. Depending on the conservation of kinetic energy, the type of a collision can be either elastic or inelastic. An elastic collision is defined as a collision in which the mass, momentum, and kinetic energy of the encountering particles are conserved. In contrast, some kinetic energy is turned into other forms of energy in an elastic collision, such as vibrational energy.

In the Mars' thermosphere and ionosphere, a nascent hot particle, such as hot O and C, collides with the major neutral atmospheric species, such as CO_2, O, CO, and N_2. As well as the source mechanisms, the most significant and fundamental process for the formation of the hot corona is collisions between hot particles and the neutral atmosphere. A hot atom or molecule can (1) be thermalized by the transfer of the energy to its collision partner, becoming a part of thermospheric constituent, or having very small probability to escape; (2) knock out a particle from the background atmosphere and make a secondary hot particle; or (3) maintain its energy above the escape energy and manage to escape to space. In the exosphere models, the collision model and its parameters are carefully chosen and examined by adopting the latest available cross sections to describe the energy and momentum transfer between hot particles and the

neutral atmosphere as realistic as possible. However, the description of nascent hot particle collisions is premature because of the lack of accurate data on the collisions.

The typical relative collision energy of the hot particles is about on the order of a few electron volts, which is considered as a relatively low collision energy. This low energy collision dominantly leads to an elastic collision. Among various collision schemes used by different exosphere models, the following subsections investigate "hard sphere" isotropic scattering and forward scattering differential collision cross sections for hot O and C atoms with the local background species.

II.2.1. Scattering

If two particles are considered as a projectile and a target, a projectile is a newly produced hot atom from its source mechanism, and a target is a local neutral background atom or molecule. The schematics of the collision geometry in the laboratory frame and the center-of-mass frame are shown in figures 2.2 and 2.3. A projectile and a target, which are a hot atom and a cold neutral background atom (or a molecule), are labeled with subscripts 1 and 2, respectively. The masses of hot and cold particles, 1 and 2, are denoted as m_1 and m_2, while the velocities are denoted as $\vec{\boldsymbol{v}}_1$ and $\vec{\boldsymbol{v}}_2$, and the primed quantities indicate post-collision status.

II.2.1.1. Center-of-mass frame (CM frame)

The center-of-mass frame (hereafter, the CM frame) is an inertial frame of reference in which the origin of the system is situated at the center of mass, $\vec{\boldsymbol{r}}_{cm}$. The CM frame is a convenient reference of frame for the computation of a collision system between two particles. The CM system moves with the respect to the laboratory frame, and the center of mass is located

at the origin of the CM frame. In the CM frame, the center of mass, by definition, is at rest, and the center of mass velocity is zero. Figure 2.2 shows a diagram of two atoms, resembling two billiard balls with radius of $\boldsymbol{R_1}$ and $\boldsymbol{R_2}$ – for the case of O_{hot}-O_{cold} collisions, $\boldsymbol{R_1} = \boldsymbol{R_2}$.

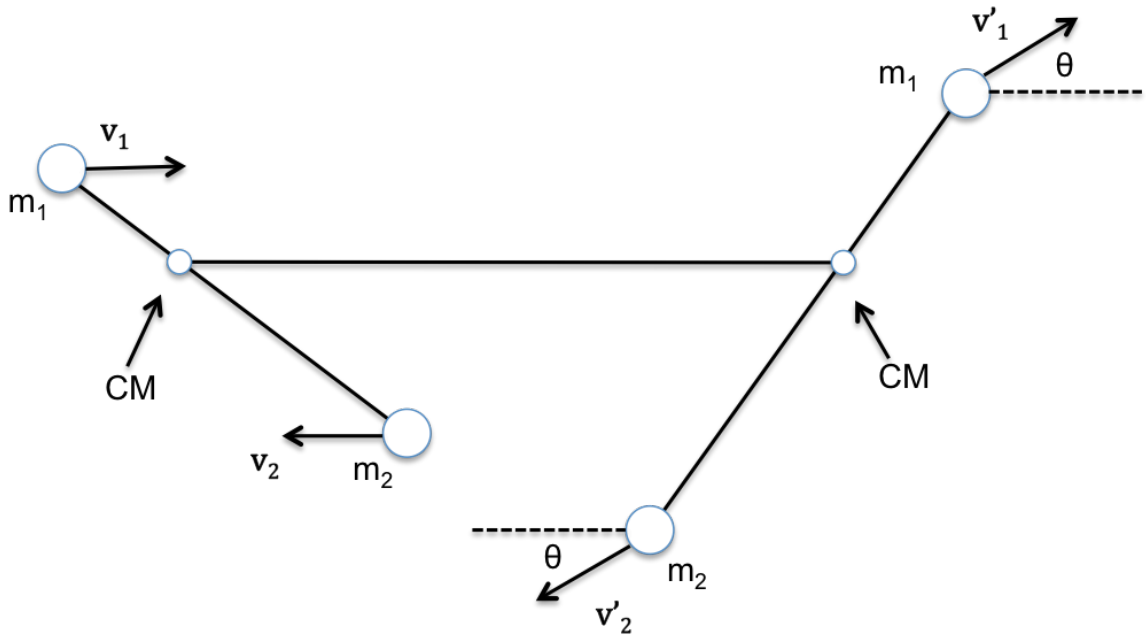

Figure 2.3. Diagrams of the projectile and target before and after the collision in the center of mass frame.

The total momentum in the CM frame before and after collision are equal to zero. According to the conservation of momentum,

$$\vec{\boldsymbol{P}}_{1,CM} + \vec{\boldsymbol{P}}_{2,CM} = m_1\vec{\boldsymbol{v}}_1 + m_1\vec{\boldsymbol{v}}_2 = 0 = \vec{\boldsymbol{P}}_{tot,CM}, \tag{2.14}$$

where the momentum before the collision for each particle are equal in magnitude but in opposite in sign. Obviously, after the collision, the sum of the momenta also vanish to zero at all times,

$$\vec{\boldsymbol{P}}'_{1,CM} + \vec{\boldsymbol{P}}'_{2,CM} = m_1\vec{\boldsymbol{v}}'_1\cos\theta + m_1\vec{\boldsymbol{v}}'_2\cos\theta = 0 = \vec{\boldsymbol{P}}'_{tot,CM}. \tag{2.15}$$

In the CM frame, the distinction between a projectile and a target is not necessary, and both particles approach each other. The total energies of the system before and after the collision are also conserved,

$$\frac{\vec{P}_{1,CM}^{2}}{2m_1} + \frac{\vec{P}_{2,CM}^{2}}{2m_2} = \frac{\vec{P}_{1,CM}^{\prime 2}}{2m_1} + \frac{\vec{P}_{2,CM}^{\prime 2}}{2m_2} = \frac{m_1}{2}, \tag{2.16}$$

II.2.1.2. Laboratory frame (Lab frame; planetocentric frame)

If the target species (cold atom or molecule) is assumed to be at rest in the laboratory frame, the collision occurs when the projectile species (hot atom) moves toward the target species with velocity of, $\vec{v}_1$, as shown in diagrams in figure 2.3.

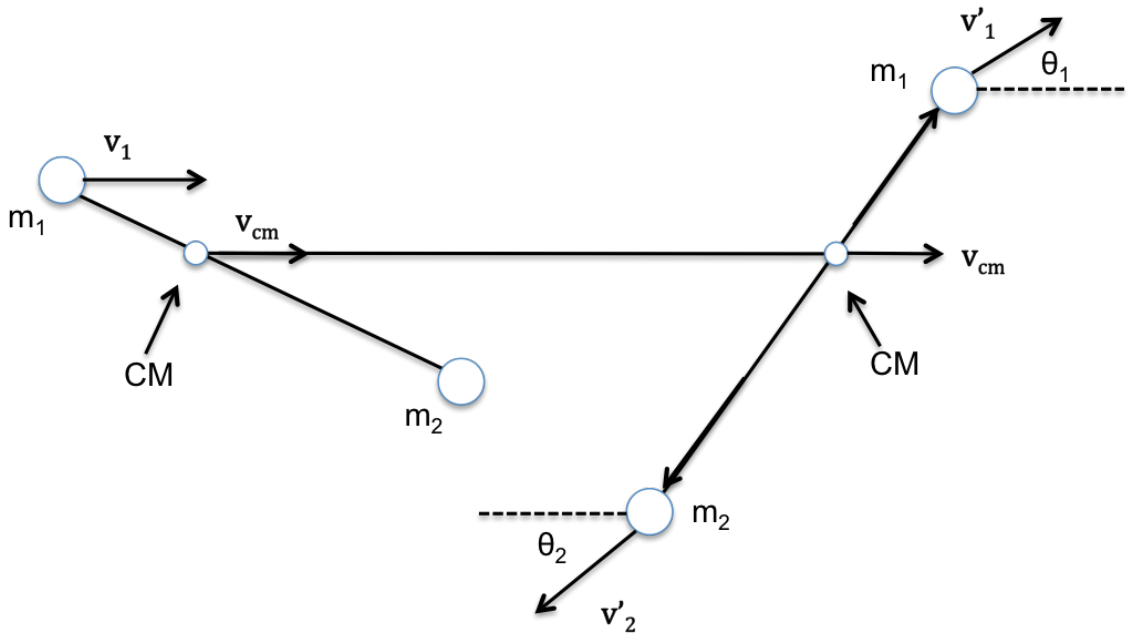

Figure 2.4. Diagrams of the projectile and target before and after the collision in the laboratory frame.

In the laboratory frame, the center of mass of two particles moves with the center of mass velocity $\vec{\boldsymbol{V}}_{cm}$, which is given by,

$$\vec{\boldsymbol{V}}_{cm} = \frac{\sum_{i=1}^{2} m_i \vec{\boldsymbol{v}}_i}{\sum_{i=1}^{2} m_i} = \frac{m_1 \vec{\boldsymbol{v}}_1}{m_1 + m_2}, \tag{2.17}$$

$$= \vec{\boldsymbol{v}}_1 \frac{M_\mu}{m_1},$$

Where M_μ is the reduced mass of the pair of colliding particles and expressed as,

$$M_\mu = \frac{m_1 m_2}{m_1 + m_2}. \tag{2.18}$$

For example, for O_{hot}-O_{cold} collisions, the reduced mass, M_μ, becomes a half of the mass of O. The center-of-mass vector is defined as,

$$\vec{\boldsymbol{r}}_{cm} = \frac{\sum_{i=1}^{2} m_i \vec{r}_i}{\sum_{i=1}^{2} m_i} = \frac{m_1 \vec{r}_1 + m_2 \vec{r}_2}{m_1 + m_2}. \tag{2.19}$$

Assuming the collision in two dimensions, the energy and linear momentum (in x- and y-directions) in the system are conserved during the collision,

$$\frac{m_1 v_1^2}{2} = \frac{m_1 v_1'^2}{2} + \frac{m_2 v_2'^2}{2}, \tag{2.20}$$

$$m v_1 = m v_1' \cos\theta_1 + m v_2' \cos\theta_2, \tag{2.21}$$

$$0 = m v_1' \sin\theta_1 - m v_2' \sin\theta_2. \tag{2.22}$$

Knowing the initial velocity of the projectile, v_1, and the corresponding scattering angles of the particles, these three independent equations enable to obtain the final velocities of the pair particles,

$$v_1'^2 = v_1^2 \left(1 - \frac{4M_\mu^2}{m_1 m_2} \cos^2\theta_1\right), \tag{2.23}$$

$$v_2' = 2 v_1 \frac{M_\mu}{m_2} \cos\theta_2. \tag{2.24}$$

Lastly, the deflection angle of the target particle is given by,

$$\theta_2 = \cos^{-1}\left(\frac{mv_1 - mv_1' \cos\theta_1}{mv_2'}\right). \tag{2.25}$$

In three dimensions, post-collision velocities of the particles require two angles, θ and φ, to be specified.

II.2.1.3. Energy and momentum transfer

The momentum transfer rate or energy diffusion rate is the rate of momentum transferred from a particle to a particle when a projectile collides with a target. The change of momentum in the center-of-mass frame is,

$$\Delta \boldsymbol{p} = m\boldsymbol{v}(1 - \cos\theta), \tag{2.26}$$

where $\Delta \boldsymbol{p}$ is the net momentum change, and θ is polar scattering angle. Since the momentum change is heavily weighted in the backward direction (θ = 180°), the energy diffusion is more favorable in backward scattering. This momentum transfer and energy diffusion are adequately described by a scattering cross section called momentum transfer cross section, σ_M,

$$\begin{aligned} \sigma_M &= \frac{(\text{Total momentum transferred per second})}{(\text{Unit incident momentum flux})}, \\ &= \text{A cross section for the momentum transfer rate,} \end{aligned} \tag{2.27}$$

which is expressed in terms of the differential cross section.

$$\begin{aligned} \sigma_M &= \int (1 - \cos\theta) \frac{d\sigma}{d\Omega}(\theta, \phi) d\Omega, \\ &= 2\pi \int (1 - \cos\theta) \frac{d\sigma}{d\Omega}(\theta) d\theta, \end{aligned} \tag{2.28}$$

where θ denotes the scattering angle; and $\frac{d\sigma}{d\Omega}(\theta, \phi)$, the differential scattering cross section, is the fraction of particles scattered into an element of solid angle, $d\Omega = \sin\theta d\theta d\phi$, in (θ, ϕ) direction per unit time. The fractional loss of momentum during a collision is described by the term $(1 - \cos\theta)$ in the collision integral above, which is in the direction of the pre-collision and is dependent on the scattering angle. Use of this momentum transfer cross section allows detailed analyses of various types of scattering collisions. In the following sections, two types of elastic collision: isotropic scattering hard sphere collision, and forward scattering differential cross section, are investigated and compared.

II.2.2. Scattering schemes

II.2.2.1 Isotropic hard sphere scattering scheme

The hard sphere isotropic scattering scheme is an idealized collision model for two encountering atoms or molecules. In an isotropic hard sphere collision, the probability of a particle scattered into solid angle, $d\Omega$, is isotropically the same in the center-of-mass frame. The isotropic hard sphere collision scheme is employed to describe a collision between a hot O or hot C atom with a radius of R_{hot} and a cold background species, the neutral background atmospheric species, with a radius of R_{cold}.

In the situation of a hard sphere collision, the scattering is isotropic, and the collision cross section is independent of the scattering angle, θ. The total collision cross section, σ_T, for the hard sphere collision scheme is defined as,

$$\sigma_T = \int \frac{d\sigma}{d\Omega} d\Omega. \tag{2.29}$$

Since $\frac{d\sigma}{d\Omega}$ is independent of θ for the isotropic scattering case, the momentum transfer cross section, σ_M, is then,

$$\sigma_M = \sigma_T. \tag{2.30}$$

II.2.2.2. Forward scattering differential cross sections

"Forward scattering" is a more realistic description of the scattering model of collisions between a hot atom and a cold background species. In this scheme, a particle after a collision is likely to be scattered into small angles, the forward direction with respect to the pre-collision direction of the projectile, resulting in a high peak in the distribution of differential scattering cross sections or angular differential cross section, $\frac{d\sigma}{d\Omega}(\theta, \phi)$. The momentum transfer cross section considerably differs from the total scattering cross section, σ_T, since the scattering is highly anisotropic. In our calculations, we use the angular differential cross section computed by *Kharchenko et al.* [2000] for collisions of O_{hot}-O_{cold} with the collision energy of 3 eV (figure 2.4).

The total scattering cross section is an integration of the differential cross section over solid angle,

$$\sigma_T = \int \frac{d\sigma}{d\Omega}(\theta, \phi) d\Omega, \tag{2.31}$$

where $\frac{d\sigma}{d\Omega}$ is dependent on the scattering angle. The scattering is assumed to be isotropic in azimuthal direction. The momentum transfer cross section in the forward scattering scheme then,

$$\sigma_M = \int (1 - \cos\theta) \frac{d\sigma}{d\Omega}(\theta, \phi) d\Omega, \tag{2.32}$$

where the term, $(1 - \cos\theta)$, represents the loss of momentum with respect to the pre-collision momentum in the center-of-mass frame.

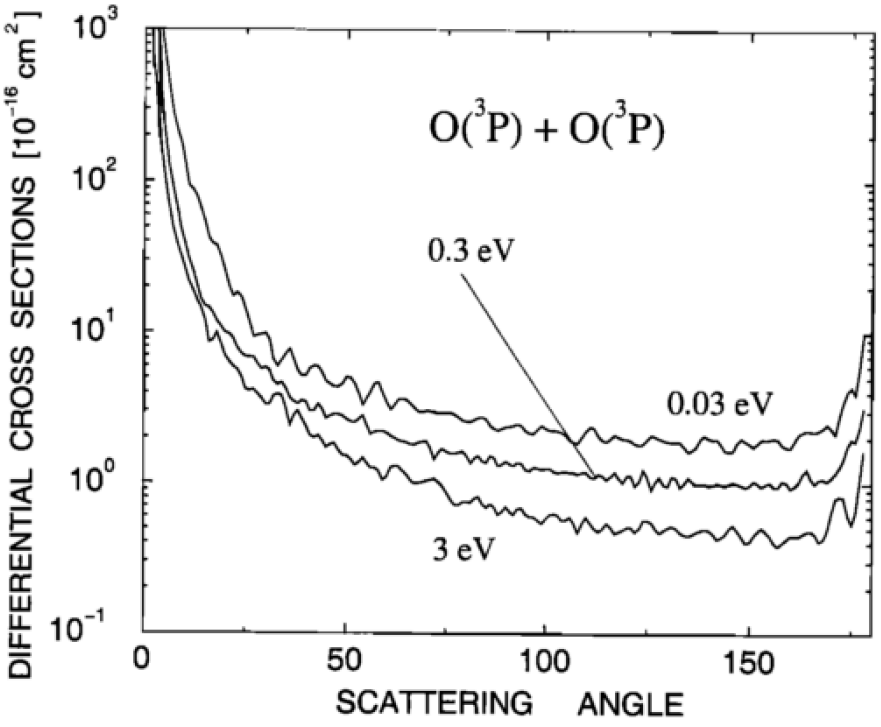

Figure 2.5. Differential cross section of elastic collisions of O atoms at different collision energies (0.03eV, 0.3eV, and 3eV). This is figure 3 in *Kharchenko et al.* [2000].

The computed σ_M for the scattering with a huge cross section in the forward direction is always smaller than the total cross section (*i.e.,* $\sigma_M < \sigma_T$). Conversely, $\sigma_M > \sigma_T$ for the backward scattering.

On Mars, other collision partners, such as O, CO_2, CO, and N_2, are considered in model simulations as background neutral species that undergo collisions with a newly produced hot O or hot C atom. Presently, the exact differential scattering cross sections are not available for other collision cases (*i.e.,* collisions between a hot atom and other cold neutrals other than O). It is certainly important to have accurate angular differential cross section distributions for collisions between various cold neutrals for more realistic description of the mechanisms in the Martian hot corona.

II.2.3. O_{hot}-O_{cold} Collision

In the upper atmosphere of Mars, two hot O atoms are produced mostly from dissociative recombination of O_2^+ via five different exothermic channels. The newly-born O atoms share the excessive energy obtained from the corresponding channel and become nascent hot O atoms (more details on the source mechanism are in chapter 4). O_{hot} participates in collisions with thermal (cold) atoms and molecules. The most frequent collision partners among all the thermospheric species are the major neutrals, which are thermal oxygen and carbon dioxide, O_{cold} and $CO_{2,cold}$. The collisions with these two species must be included in the model for the hot O, since O_{hot}-O_{cold} and O_{hot}-$CO_{2,cold}$ collisions play an important role in determination of thermalization and the local neutral heating in the ambient atmosphere and the structure of the Martian hot O corona. It is, thus, crucial to examine and understand these collisions in detail to model the hot O corona accurately.

The models for the Martian hot O corona have adapted several different schemes for describing the collisions between a hot atom and a thermospheric species. A majority of models have used the isotropic scattering approximation by treating the collision as hard sphere collision. To describe the collisions more realistically, a collision model would need differential scattering information. A recent study by *Kharchenko et al*. [2000] have analyzed the differential scattering cross section for O_{hot}-O_{cold} collisions that have been considered in recent hot O simulations [*Fox and Hać*, 2009; *Fox and Hać*, 2014].

Particularly, this section focuses on O_{hot}-O_{cold} collisions to investigate difference in mechanisms resulted from different types of collision schemes. All other collision pairs and the effects of using two different collision schemes on the hot O corona are discussed in the study of

the hot O corona later in chapter 8. This section compares the effect that the cross sections and energy and momentum transfer during collisions have on the thermalization of hot O.

Figure 2.5 shows both the hard sphere cross section and the angular differential cross section for O_{hot}-O_{cold} collisions with collision energy of 3 eV, computed by *Kharchenko et al.* [2000]. The differential cross section in angle for the hard sphere scheme (green line) is constant over all scattering angles, representing isotropic scattering. Integration is performed to calculate the total cross section for the forward scattering scheme (blue line), which shows the highly peaked scattering in the forward direction (in small angles).

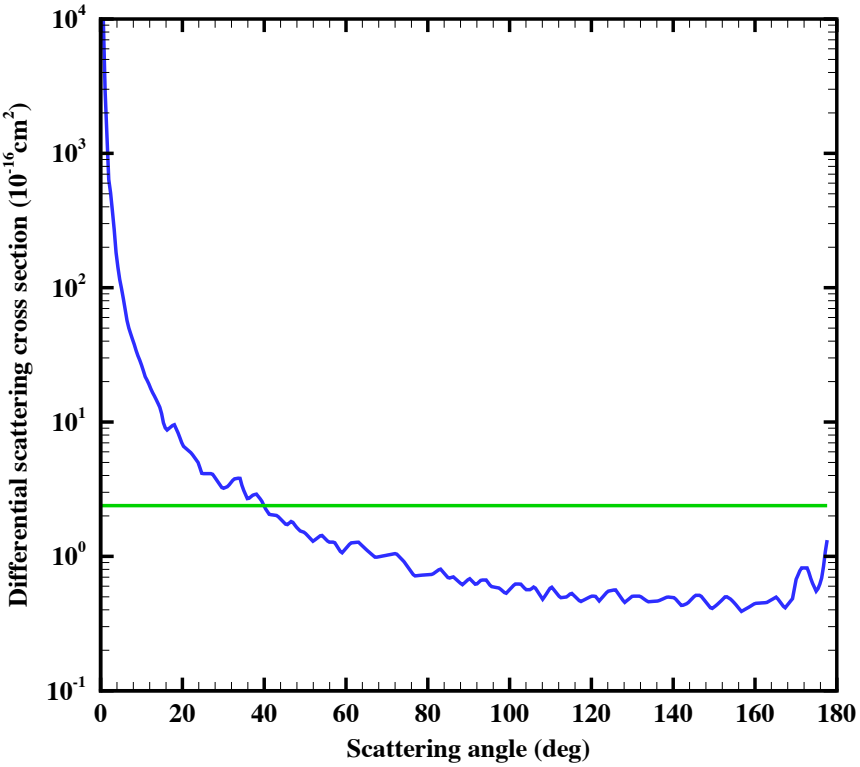

Figure 2.6. Angular differential scattering cross sections for hard sphere collision and forward scattering schemes. *Kharchenko et al.* [2000].

The cross sections for the momentum transfer rate during a collision are shown in figure 2.6 for both scattering schemes. In both scattering schemes, all scattering in the angles smaller than about 40° participate in only a small momentum transfer. With increasing scattering angle, the isotropic hard sphere scattering produces a significant transfer of momentum to the scattering center, and the momentum transfer cross section decreases in the angles larger than ~120°. For the forward scattering scheme, differential momentum transfer cross section shows only a relatively small variation, nearly isotropic, over the scattering angles.

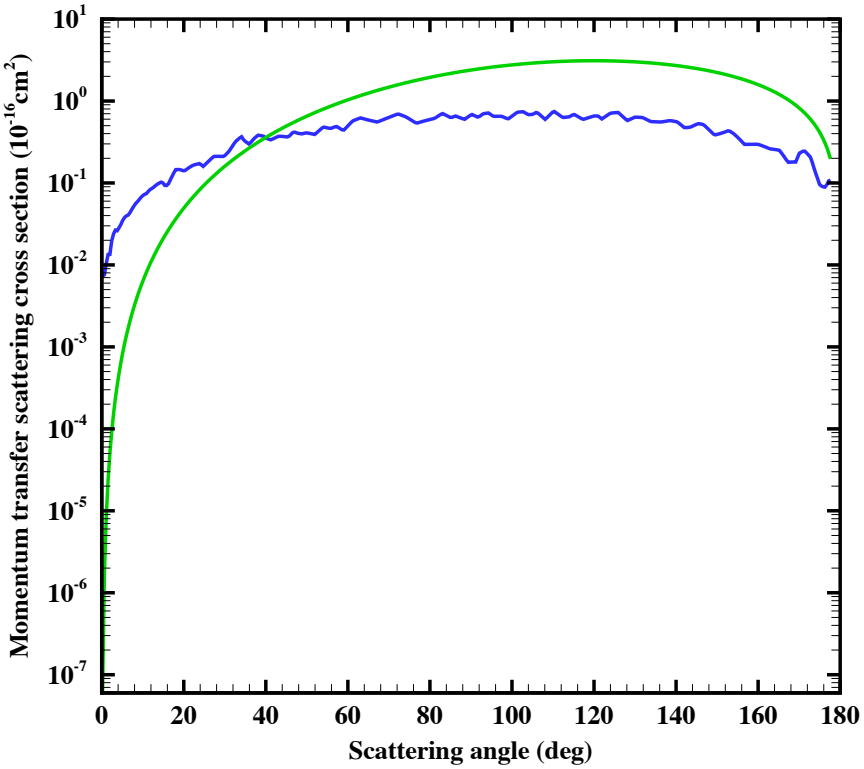

Figure 2.7. Angular differential momentum transfer cross sections for hard sphere collision and forward scattering schemes.

As shown in table 2.1, the computed total collision cross section for the forward scattering collision is a factor of ~2 larger than that for the isotropic scattering collision. However, momentum transfer is much smaller in forward scattering collision. Consequently, the isotropic scattering scheme describes a more effective momentum and energy transfer to the collision partner (thermospheric constituent), which indicates a more active thermalization of hot oxygen. In spite of the larger collision cross section, the momentum and energy transfer in the forward scattering scheme is not as efficient as in the isotropic scattering scheme, resulting in a relatively low thermalization of hot oxygen via O_{hot}-O_{cold} collisions.

σ (cm^2)	Isotropic scattering	Forward scattering
Total collision cross section (σ_T)	3.0×10^{-15} cm^2	6.4×10^{-15} cm^2
Total momentum transfer cross section (σ_M)	3.0×10^{-15} cm^2	8.5×10^{-16} cm^2

Table 2.1. The computed total collision cross sections, σ_T, and total momentum transfer cross section, σ_M, for the isotropic scattering and forward scattering schemes.

Since the cross sections for collisions and momentum transfer are known, it is important to discuss the energy distribution of O before and after the collisions. In order to investigate further the difference in the energy loss processes, the energy distributions are normalized to show probability density, computed as a function of altitude (100 km – 500 km). This probability density describes the relative likelihood for a nascent O to have a certain amount of energy. Figure 2.7a and figure 2.8a show the energy distribution of nascent O in 3D and 2D, where the color contour indicates the probability density of the particles. The nascent O is produced from dissociative recombination of O_2^+, and O obtains its energy from the exothermicities of the

channels in the source reaction (more details in chapter 4). The peaks in the distribution of the nascent O energies become broadened at high altitudes (> ~240 km) with increasing ion temperature.

This energy distribution is used to compute the initial energy of the particle in the isotropic and forward scattering cases. The isotropic scattering scheme uniformly distributes scattering angles, which allows the efficient thermalization of colliding atoms. The energy distribution shown in figures 2.7b and 2.7c and figures 2.8b and 2.8c represent the energy distribution of the particles after one collision event, with the initial energy given from the source reaction. The isotropic scattering case is shown in figure 2.7b and figure 2.8b in 3D and 2D. The post-collision energy of O is completely different from the initial energy distribution. Most of O the atoms after the collision have an energy below the escape energy (indicated by a solid white vertical), and only a few O atoms maintain their energy near or above the escape energy. Contrarily, in the energy spectrum that results from using the forward scattering scheme, there is a high probability density of the population of particles remaining in the energy range ~1.5 eV – 2.5 eV, where the two high peaks in the initial energy distribution are located. The populated area becomes broadened at high altitudes.

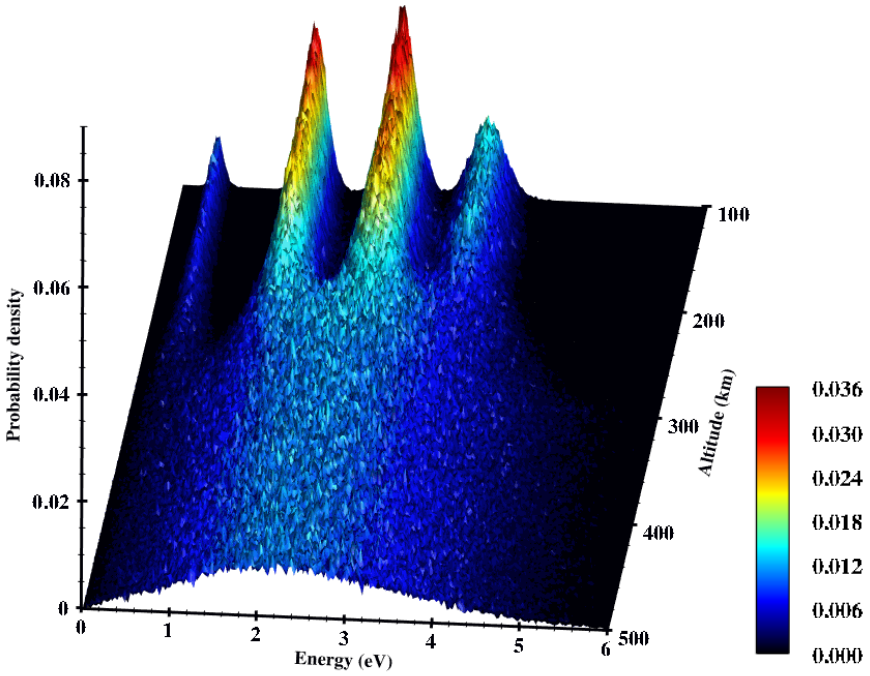
Probability density
0.08
0.06
0.04
0.02
0
0
1
2
3
4
5
6
Energy (eV)
100
200
300
400
500
Altitude (km)
0.036
0.030
0.024
0.018
0.012
0.006
0.000

(a)

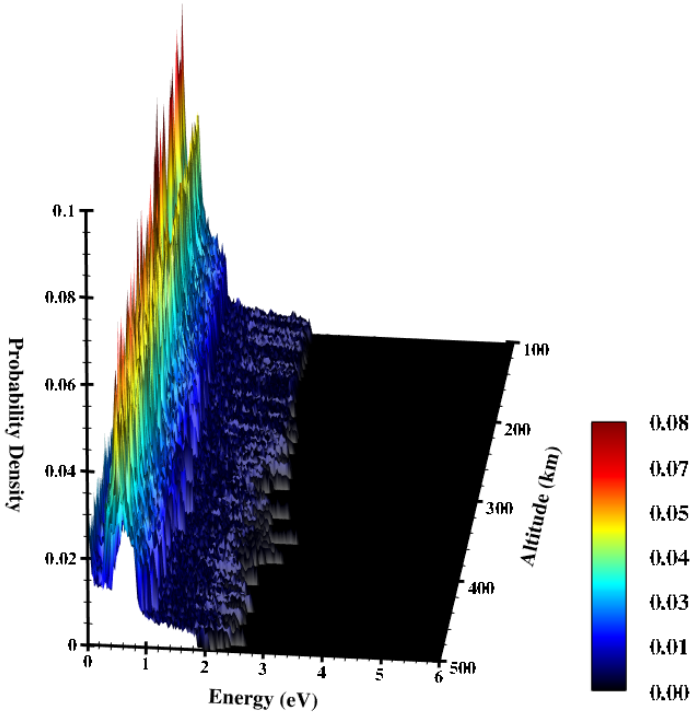
Probability Density
0.1
0.08
0.06
0.04
0.02
0
0
1
2
3
4
5
6
Energy (eV)
100
200
300
400
500
Altitude (km)
0.08
0.07
0.05
0.04
0.03
0.01
0.00

(b)

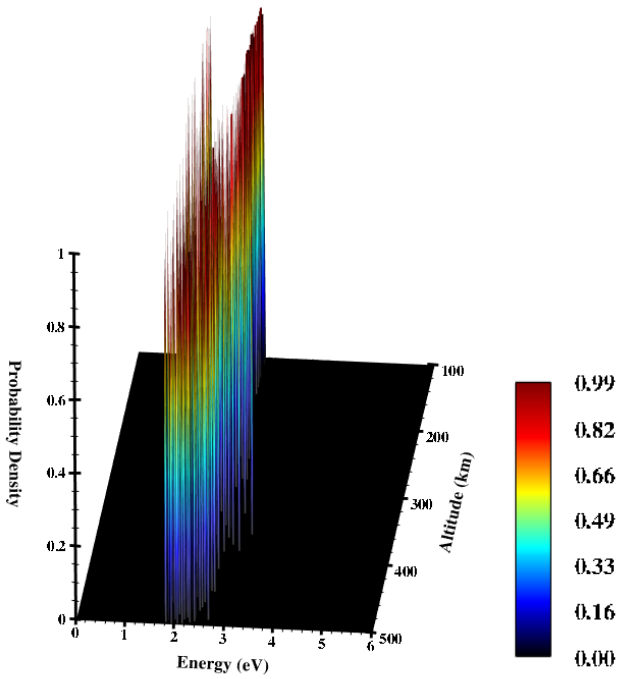

(c)

Figure 2.8. 3-dimensional altitude variation of the energy distributions of particles (a) before collisions and (b) after collisions assuming isotropic scattering and (c) forward scattering. The color contours indicate the probability density for particles in energy bins.

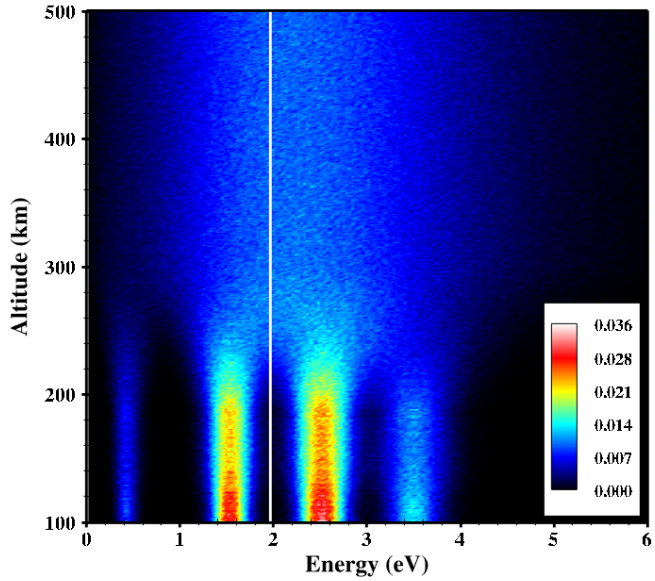

(a)

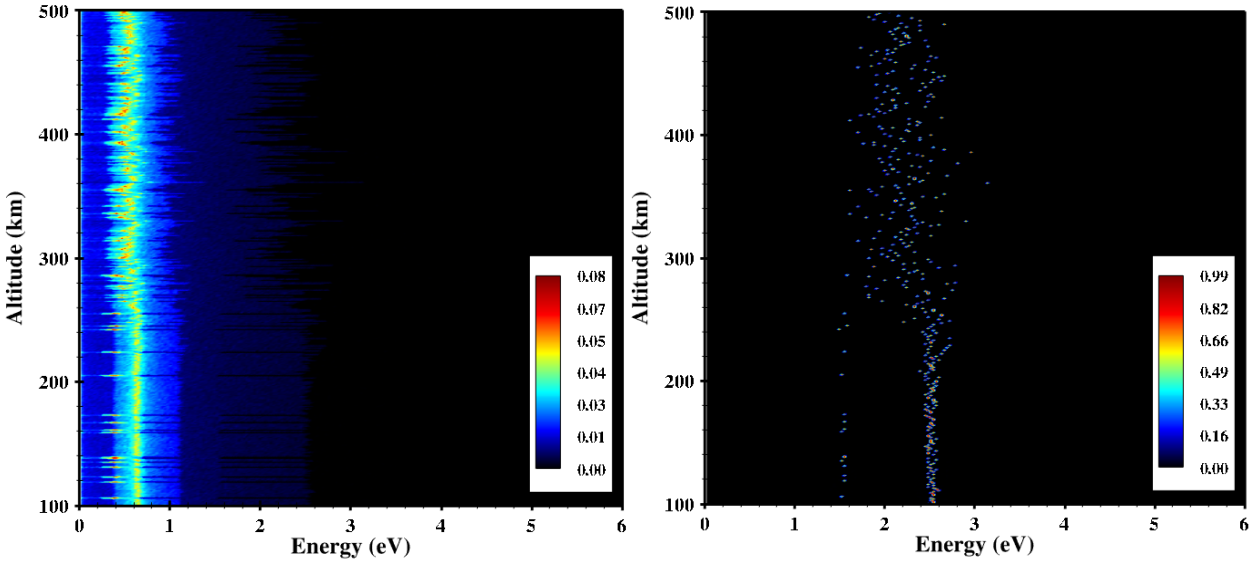

(b) (c)

Figure 2.9. 2-dimensional altitude variation of the energy distributions of particles (a) before collisions and after collisions assuming (b) isotropic scattering and (c) forward scattering. The color contours indicate the probability density for particles in each energy bin. The white solid vertical line corresponds to the escape energy (~1.97 eV).

The extracted energy spectra from the pre- and two post-collision energy distributions are shown in figure 2.9. Under the isotropic scattering assumption, the nascent O energy effectively lost its energy via the collision and scattered into the full range of the angles around the particle. The high peak of the isotropic scattering spectrum describes the large energy loss after the collision and the high probability of thermalization of O atoms. On the other hand, a strong peak in the forward scattering spectrum indicates the highly probable chance for the O atom to remain with its initial energy by scattering into forward direction. Therefore, the collision with the isotropic scattering assumption provides a higher probability for O atoms to lose its energy and momentum and become thermalized than that with the forward scattering assumption. In reality, a hot O atom undergoes numerous collisions with the background particles including O, CO_2, CO, and N_2, and these collisions modify the energy distribution of O. The typical cross sections of hard sphere isotropic scattering used in simulations are a factor of 2 or 3 smaller than that of the forward scattering. This would tend to reduce the aforementioned large difference in the results after the initial collision, since fewer of the isotropic scattering collisions would occur given the original population of hot O.

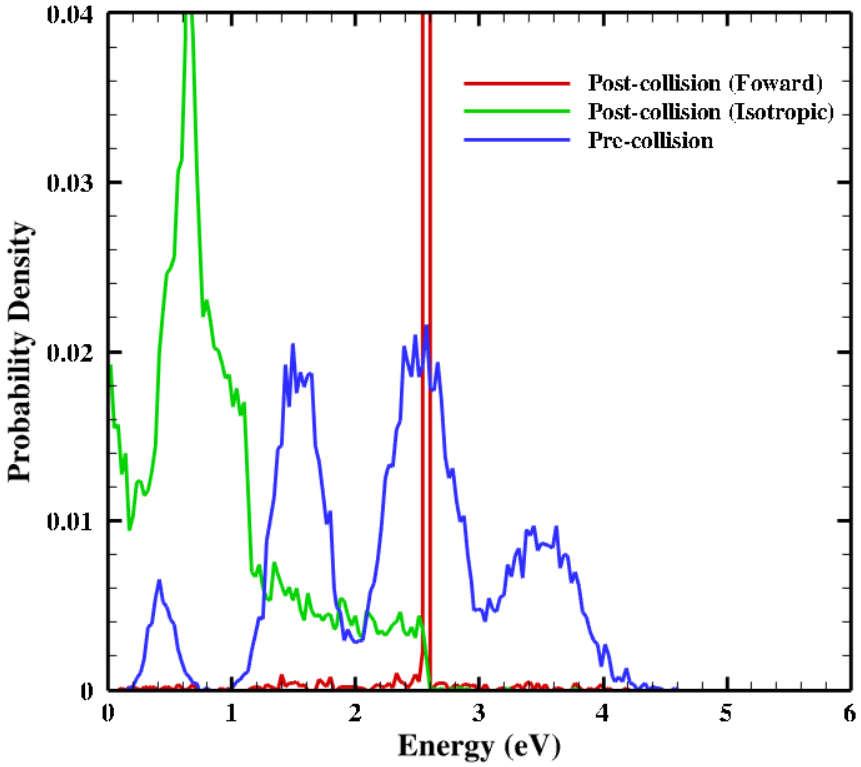

Figure 2.10. Spectra of nascent O energy from the dissociative recombination reaction (blue) and post-collision O energy resulted from using the isotropic scheme (green) and forward scattering scheme (blue) at an altitude of 200 km.

Chapter III

Models and framework

This chapter presents two thermosphere/ionosphere models and our kinetic particle simulator. The thermosphere/ionosphere models are employed in the kinetic particle simulator for the simulation of the Martian hot atomic coronae. The model description sections are followed by the detailed description of the coupled framework.

III.1. Thermosphere/ionosphere models

III.1.1. Mars Thermosphere General Circulation Model (MTGCM)

The Mars Thermosphere General Circulation Model (MTGCM) is a 3D finite difference primitive equation (thermodynamic, eastward momentum, northward momentum, composition, hydrostatic, and continuity equations; see also *Bougher et al.* [1988, 1990]) model that self-consistently solves for time-dependent neutral temperatures, neutral-ion densities, and three component neutral winds over the globe [*Bougher et al.*, 1999, 2000, 2002, 2004, 2006, 2009]. Above the 1.32 μbar level (33 pressure level), corresponding to an altitude range of about 70 – 300 km for solar maximum conditions, prognostic equation fields for the major neutral species (CO_2, CO, N_2, and O), selected minor neutral species (Ar, He, and O_2), and photochemically produced ions (*e.g.*, O_2^+, CO_2^+, O^+, CO^+ and NO^+ below 180 - 200 km) are simulated on a 5° latitude and 5° longitude grid resolution. The MTGCM has log-pressure vertical coordinate with 0.5 scale height spacing. The important feedback of simulated O atoms upon CO_2 cooling rates

is captured by implementing a fast Non-Local Thermodynamic Equilibrium (non-LTE) 15-μm cooling scheme with corresponding near-IR heating rates [*e.g.*, *Bougher et al.*, 2006; *López-Valverde et al.*, 1998]. The F10.7 index (solar EUV/UV flux variation), the heliocentric distance, and solar declination, key parameters for Martian seasons and solar cycle variations can be adjusted to customize MTGCM cases for different purposes of study.

The MTGCM is currently an upward-coupling model that is driven from below by the NASA Ames Mars General Circulation Model (MGCM) code [*e.g.*, *Haberle et al.*, 1999] at the 1.32 μbar level. At this pressure level, key variables, such as zonal and meridional winds, temperatures, and geopotential heights, are passed upward (only) from the MGCM crossing the lower boundary of the MTGCM on a 2-minute time step. This one-way coupling provides a realistic description of the Martian lower atmosphere to the MTGCM by including the continuous effects of upward propagating migrating and nonmigrating tides and the seasonal effects of the expansion and contraction of the lower atmosphere. Various applications of this coupled MGCM-MTGCM framework have successfully (1) reproduced observed thermospheric polar warming features [*Bougher et al.*, 2006, 2008], (2) derived exospheric temperatures [*Bougher et al,* 2000, 2009], (3) reproduced measured nightside mesopause temperatures [*McDunn et al.* 2010], and (4) reproduced measured longitude variations of the thermosphere and ionosphere density structure [*e.g., Bougher et al.* 2004]. The MTGCM can, thus, provide a realistic simulation of the Martian upper atmosphere structure.

III.1.2. Mars Global Ionosphere Thermosphere Model (M-GITM)

The Mars Global Ionosphere Thermosphere Model (M-GITM) [*Bougher et al.,* 2014b] is a newly developed Mars thermosphere and ionosphere model. This new single framework of the

whole Martian atmosphere allows overcoming the limitation in descriptions of dynamical coupling processes liking the lower and upper atmospheres in the coupled MGCM-MTGCM framework. The new M-GITM model is developed based on the Earth GITM code that is a 3D spherical model for terrestrial thermosphere and ionosphere system. M-GITM simulates the Mars' atmosphere from the surface to the exosphere, the whole atmosphere from ~ 0 km to 250 km, where the formulations and subroutines have largely been taken from the NASA Ames' Mars General Circulation Model and NCAR MTGCM codes.

M-GITM is also a self-consistent finite difference primitive model, which solves for time-dependent neutral temperatures (ion and electron temperatures are based upon Viking measurements), neutral and ion densities, and three components of neutral global winds. The M-GITM code simulates key neutral species (CO_2, CO, O, N_2, O_2, and Ar at present, and N(^{4}S), N(^{2}D), NO, He, and H_2 in the future) and key photochemical ion species (O^+, O_2^+, CO_2^+, N_2^+, and NO^+), solving fluid equations in a 3D spherical coordinate system. Typical simulations are conducted on a 5° × 5° latitude and longitude horizontal grid with a constant 2.5 km vertical altitude resolution (about 0.25 scale height spacing). For the atmosphere below an altitude of ~ 80 km, a "stretched" vertical grid is used to capture the variable terrain. A state-of-the-art radiation (RT) code from the MGCM is incorporated into M-GITM to provide solar heating, seasonally variable aerosol heating, and CO_2 15-μ cooling scheme in the LTE region of the Martian lower atmosphere (0 km – 80 km). For the upper atmosphere (~80 km – 250 km), an existing fast NLTE CO_2 15-μ cooling and a correction for NLTE near-IR heating rates (~80 km – 120 km) are implemented into M-GITM [*e.g., Lopez-Valverde et al.,* 1998; *Bougher et al.,* 2006; *Bougher et al.,* 2014b]. The M-GITM model simulation can be run for different combinations of

Martian seasons and solar conditions by varying parameters for various orbital position, solar cycle, and dust conditions.

The M-GITM code is unique by its relaxation of the assumption of hydrostatic equilibrium and separation of the vertical and horizontal fields. Like in the GITM code, M-GITM solves the Navier-Stokes equation in the radial direction independently from the horizontal directions (detailed descriptions of the coupled Navier-Stokes equations are provided by *Bell et al.* [2010] and *Ridley et al.* [2006]). The relaxed hydrostatic equilibrium assumption, non-hydrostatic atmosphere, allows each neutral species to have its own self-consistent vertical continuity and momentum equations. The present M-GITM model describes a photochemical ionosphere only, but the ionospheric transport will be included in the future.

III.2. Kinetic particle simulator – Adaptive Mesh Particle Simulator (AMPS)

Unlike the Earth's atmosphere, the Martian atmosphere is tenuous and has a low surface pressure of about 6 mbar; this is likely due to both to Mars' lower gravity (small size and mass) and the absence of a permanent magnetic field since an early epoch of the solar system [*Acuña et al.,* 1998; *Smith et al.,* 1965]. Especially, in the upper atmosphere, the exponential decrease of density with increasing altitude reaches a point where energy transitions are no longer dominated by collisions, deviating from local thermodynamic equilibrium (LTE), and so numerical modeling of this region is challenging [*Combi*, 1996]. This region is a rarefied multispecies gas flow regime under non-thermodynamic equilibrium conditions, which can be appropriately described by the Boltzmann collision integral equation,

$$\frac{\partial f_s}{\partial t} + \boldsymbol{v_s} \cdot \nabla f_s + \boldsymbol{a_s} \cdot \nabla_{\boldsymbol{v}} f_s = \frac{\delta f_s}{\delta t} = \sum_p \int_\infty \int_0^{4\pi} [f_s^* f_p^* - f_s f_p]\, g_{sp} \sigma_{sp} d\Omega d\boldsymbol{v_p}, \qquad (3.1)$$

where $f_s \equiv f_s(t, \boldsymbol{x}, \boldsymbol{v_s})$ denotes the phase space distribution function of species of type 's,' the asterisk represents the post-collision state, $\boldsymbol{x}$ is the spatial coordinate, $\boldsymbol{v_s}$ is the velocity, $\boldsymbol{a_s}$ is the acceleration, Ω is the solid angle, σ_{sp} is the total collision cross section between species *s* and *p*, and $g_{sp} \equiv |\vec{\boldsymbol{v}}_{\boldsymbol{s}} - \vec{\boldsymbol{v}}_{\boldsymbol{p}}|$. The Boltzmann equation is an integro-differential equation, which contains the collisional integral and describes the evolution of the distribution function of macroscopic characteristics.

The collisional integration usually makes solving the Boltzmann equation intractable either analytically or numerically; thus, a numerical and kinetic particle approach that does not require the formulation of an integro-differential equation is needed. The standard method for solving the Boltzmann equation in cases like this has been developed using the Direct Simulation Monte Carlo (DSMC) [*Bird,* 1994] method. As a key feature, the DSMC method separates the translational motion of species from the intermolecular interaction, allowing a description of a much wider relaxation scheme than the Boltzmann equation does. During the relaxation stage, the velocity coordinates of collision partners from the same cell can be changed due to a chosen probabilistic relaxation model.

The Monte Carlo method allows development of the numerical algorithm that is based on a simulation of the relaxation process of the distribution function in a rarefied gas. The Monte Carlo scheme is generally described by a Markov chain, a discrete-time process, which assumes that the future behavior only depends on the present. As a continuous-time version, the Markov process [*Hochstim*, 1969] is used to describe the evolution of the distribution function, $f(v, t)$, which is represented in the integral from,

$$f(\boldsymbol{v}, t + \Delta t) = \int f(\boldsymbol{v} - \Delta \boldsymbol{v}, t) P(\boldsymbol{v} - \Delta \boldsymbol{v}, \Delta \boldsymbol{v}) d(\Delta \boldsymbol{v}), \tag{3.2}$$

together with the normalization,

$$\int P(\boldsymbol{v}, \Delta\boldsymbol{v}) d(\Delta\boldsymbol{v}) = 1. \tag{3.3}$$

The function evolves as the probability, $P(\boldsymbol{v}, \Delta\boldsymbol{v})$, for the velocity of v of a particle at time t converges to the velocity of $\boldsymbol{v} + \Delta\boldsymbol{v}$ at time $t + \Delta t$, without being affected by the previous history.

This Monte Carlo simulation computes an averaged value of macroscopic functions, including density, velocity, and flux, over defined regions of the phase space using the standard kinetic theory definitions. Since a probabilistic relaxation scheme is based on collisions; the total collision frequency, $\boldsymbol{\nu}$, is a key quantity. $\boldsymbol{\nu}$ can be defined from the Boltzmann collision integral as

$$\boldsymbol{\nu} = \frac{n}{N} \sum_{i<j} \int \omega\left(\boldsymbol{\nu_i} \boldsymbol{\nu_j} \rightarrow \boldsymbol{\nu_i'} \boldsymbol{\nu_j'}\right) d^3\boldsymbol{\nu_i} d^3\boldsymbol{\nu_j} = \frac{n}{N} \sum_{i<j} \sigma_t(g_{ij}) g_{ij}, \tag{3.4}$$

where $\sigma_t\left(g_{ij}\right)$ is the total collision cross section, g_{ij} is the relative speed between species i and j, and ω is the total momentum cross section. The summation is performed over $N(N-1)/2$ possible pairs for collisions. The post-collision velocities are computed in accordance with the laws of conservation of mass, momentum, and energy in every intermolecular interaction.

The DSMC method separates the translational motion of species from the intermolecular and uses a Markov chain scheme to describe the evolution of the velocity distribution function. The total collision frequency is a key quantity in the development of the relaxation scheme of the model. The probabilistic relaxation scheme is based on a representative sampling of actual intermolecular collisions. The post-collision velocities are computed in accordance with the laws of the conservation of mass, momentum, and energy in every interaction. The Monte Carlo simulation then computes an averaged value of macroscopic functions, including density, velocity, and flux, over defined regions of phase space using the usual definitions from standard kinetic theory.

Using the DSMC method allows incorporation of complex physical processes without a significant complication of the numerical procedure. The DSMC approach has been used in other applications, such as the investigations of the cometary coma and the upper atmospheres of other planets; examples are found in *Combi* [1996], *Crifo et al.* [2005], *Markelov et al.* [2006], and *Tenishev et al.* [2008, 2011, 2013].

A state-of-the-art 3D DSMC simulator, the University of Michigan Adaptive Mesh Particle Simulator (AMPS) code [*Tenishev et al.,* 2008, 2013] was first coded for solving the Boltzmann equation of the gas flow in the coma of a comet [*Tenishev et al.*, 2008]. AMPS is developed within the frame of the DSMC method, which employs a stochastic solver for both the linear and nonlinear Boltzmann equations. As a standard numerical method today, the DSMC method can represent the collisional dynamics of a finite number of model particles in a rarefied gas flow regime, such as Mars upper atmosphere. In place of solving the intractable Boltzmann equation, AMPS simulates the ensemble of model particles and captures the physics of the distribution of the gas species in the tenuous upper atmospheres, where the transitions from a local thermodynamic equilibrium (LTE) region to a non-LTE region occur. The cell size of the computational domain varies by the lower and upper limit of the cell sizes, which are pre-determined in the initialization process.

Utilizing the technique of the Adaptive Mesh Refinement (AMR) [*Berger and Colella*, 1989], which will be discussed in the next section, the cell size is the smallest only where the important production of hot particles and the interaction between nascent hot particles and background atmosphere take place. The nominal cell size is about 80 km at the bottom of the computational domain, and the maximum cell size is determined by the designated upper boundary of the domain. In general, the simulation scheme does not require the limitation of the

characteristic size of computational cells, since the simulation is rather closely related to the spatial distribution, gradient, and collision frequencies of the local background densities. The cell size matters only for averaging the macroscopic parameters and can be as large as 80 km at the bottom of the domain without affecting the overall computation. For the purpose of sampling the macroscopic parameters, a special treatment is discussed, which is applied on the mesh in the next section. The typical size of the domain can be set as small as about 2-3 Mars radii, which allows the reduction of computational time and resources to compute escape rates of neutral particles without underestimating the escape. The local time step is determined by the ratio between the smallest characteristic cell size and the upper limit of the hot carbon speed. Typically, the simulation runs fast enough with a local time step of about 2 seconds. This local time step is set large enough for the code to recognize a model particle in the same cell for at least a few iterations during the simulation.

III.2.1. 3D Adaptive Mesh Refinement (AMR) and auxiliary mesh

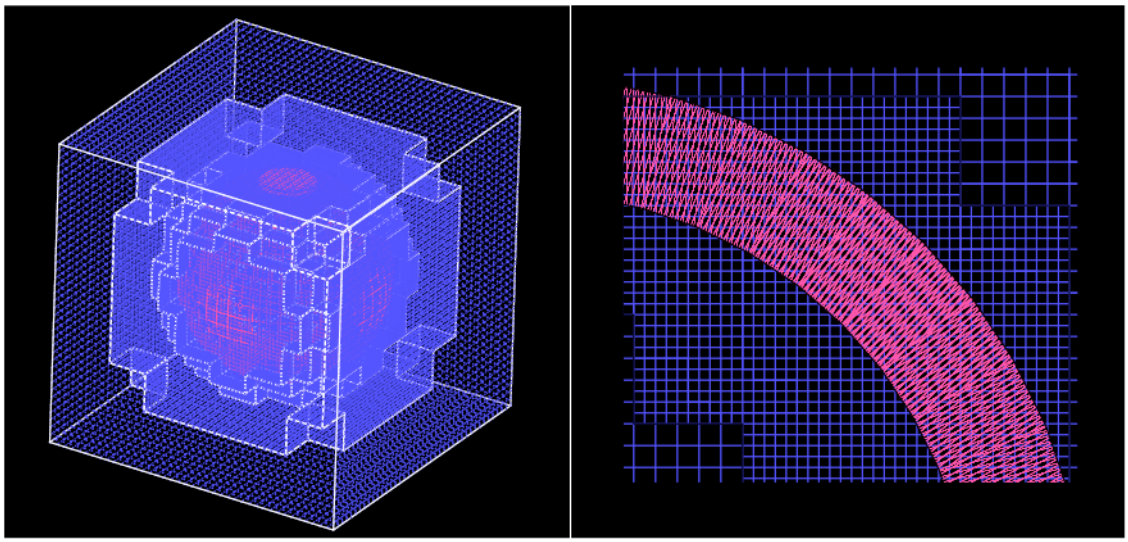

(a) (b)

Figure 3.1. (a) The 3D computational domain (cubic cells, blue) and overlaid spherical auxiliary mesh (pink), (b) a sectional view of the region of interest.

Modeling a large number of particles with realistic reactions and interactions in time- and region-dependent gas systems requires high computational cost. Prior to this work, the unstructured mesh of tetrahedral cells [*Valeille et al.*, 2009a, 2009b, 2010a, 2010b] method determined the local values at the points on the mesh, which is generated at the beginning of the simulation with fixed spacing. This approach had the advantage of a fine radial resolution (*e.g.*, about one half to one third of the local scale height in the transitional domain) capturing steep density gradients with altitude. However, to cover the critical details in the atmosphere, a simulation on this mesh demanded too much in computing time and resources, and even with this high resolution, the computation on the mesh could not guarantee satisfactory accuracy over the whole domain.

The model methodology now utilizes the technique of the Adaptive Mesh Refinement (AMR) [*Berger and Colella*, 1989], which is computationally efficient for realistic simulations of the atmosphere of Mars. This current mesh algorithm is capable of an appropriate description of the regions in the atmosphere with important features by minimizing the use of computational resources. Since a finer mesh is placed over a base coarse mesh covering the whole domain, the local enhancement of mesh resolution effectively handles the regions of interest with the local time step and cell size. At present, the use of this mesh drastically reduces the computation time and resources and increases the accuracy of the simulation.

The physical situation that needs to be modeled involves sharp density gradients in the lower altitude region (about 80 – 200 km). The macroscopic parameters, such as production rate and density, are difficult to sample and visualize in these regions since the cell is not small enough to capture the rate of change. For example, the density of CO^+ has an abrupt inflection point at around 140 km altitude and an exponential decrease after its peak density at an altitude of about 210 km (for the low solar activity case). The production rate of hot oxygen has a sharp radial gradient deep in the thermosphere. To sample these local features accurately, one can increase the resolution of the mesh in the lower altitude region. However, it is too costly in computation to increase the resolution of the cubic cell mesh just for a sampling purpose. The other solution, which has been applied in the mesh, is that an auxiliary mesh is overlaid, a spherical coordinate mesh, on the Cartesian coordinate mesh (figure 3.1; mesh in pink). In 3D, the overlapping mesh is like a shallow sphere centered at the origin of the simulation. This auxiliary mesh resembles the previous mesh [*Valeille et al.*, 2009a, 2009b, 2010a, 2010b], but it is a simple spherical mesh that permits taking the advantage of the fine radial resolution when sample macroscopic parameters are needed from the computational domain. The thickness of the

shell, which can be adjusted manually, is the range of the region of interest. This auxiliary mesh is used only for sampling purpose and not a part of the computational domain.

III.3. Coupling and framework

In this thesis, the 3D MTGCM and M-GITM simulate the exact Martian seasonal and solar cycle conditions considered, utilizing solar longitude (L_s) and solar EUV flux (F10.7) parameters. The densities of thermosphere-ionosphere species (O, CO, CO_2, N_2, CO^+ (only MTGCM), O_2^+, and e^-), temperatures (T_n, T_i, and T_e), and three-component neutral winds (zonal, meridional, and vertical winds) are compiled in the MTGCM and M-GITM codes in the frame of AMPS to be used as the necessary parameters for the production of hot carbon and hot oxygen and for the background atmosphere. As an atmospheric input, these thermosphere/ionosphere parameters are pre-calculated by the MTGCM (from 135 km to 200 km) and M-GITM (from ~100 km to ~300 km), and supplied to Mars-AMPS, achieving a one-way coupling between the MTGCM/M-GITM and Mars-AMPS codes. Above the input boundary (*i.e.,* 200 km and 300 km altitude for the MTGCM and M-GITM, respectively), the Mars-AMPS code extrapolates the density profiles using the local density scale height. It is safe to use this realistic extrapolation scheme to estimate the density beyond the upper boundary of the atmospheric inputs, since the important production of hot carbon and gradients occur within the input domain.

The contribution from the atmosphere below the lower boundary of the input domain is assumed to be negligible to the result. The exception is the production of hot C atoms in the dissociative recombination of CO^+, where CO^+ density could not be extrapolated as is done for the densities of other background species. However, the computed peak production rate of the dissociative recombination of CO^+ is still located below an altitude of 200 km because the

reaction is also dependent on the electron temperature and electron density, which vary significantly with altitude. The detailed description of the special treatment for CO^+ density is discussed in chapter 5.

The extrapolation scheme was used in the previous works by *Valeille et al.* [2009a, 2009b, 2010a, 2010b]. As mentioned in those previous works, the background atmosphere, which consists of the MTGCM inputs and the extrapolation, are in good agreement with the observations from the Viking Landers [*Hanson et al., 1977; Nier and McElroy*, 1977], Mars Global Surveyor (MGS) [*Withers et al.,* 2008; *Withers and Mendillo,* 2005], and Mars Express (MEX) [*Morgan et al.,* 2008].

The AMPS code considers a particle in the domain to be a hot atom when it satisfies the local velocity criterion, $V_{model\ particle} > V_{threshold}$. For computational purposes, this work sets $V_{threshold}$ to either twice the local thermal speed or the local escape speed. As noted by *Valeille et al.* [2010a], setting $V_{threshold}$ to twice the local thermal speed results in a hot population that is less than the hottest 1% of the Maxwellian distribution of thermospheric population. This setting is validated by *Valeille et al.* [2010a] as a best estimated $V_{threshold}$, ensuring a clear separation between the hot and cold populations. Separately, $V_{threshold}$ can be set to the local escape speed for the purpose of reducing resources and computational time without underestimating the escaping hot atoms. $V_{threshold}$ is one of the key parameters in the simulation of the Martian hot corona, which is set to slightly different values for other models. For example, *Yagi et al.* [2012] set an energy cut-off for their model particles to 1/15 of the escaping energy of hot species. This setting allows consideration of about 2% of the hottest end of the Maxwellian distribution of thermal population as nonthermal (hot) population.

AMPS is a DSMC model that runs in a test-particle Monte Carlo mode for the Martian hot atomic corona calculations. AMPS has been used in full DSMC mode for the simulation of cometary coma [*e.g., Tenishev et al.,* 2008; *Fougere et al*., 2013]. The motion of each hot particle is influenced by the gravitational field of Mars and affected by the collisions with background species on its way to escape to space or to become part of the cold population (*i.e.,* thermospheric population). The only collision case that is considered in the simulation is the collisions between hot species and background species. For example, the collisions between hot carbon atoms can be also possible. However, due to relatively low density of hot carbon, the collision frequency of C_{hot}-C_{hot} is much smaller than that of C_{hot}-background species (O and CO_2). The C_{hot}-O_{cold} collision frequency is on the order of 10^{-3} s^{-1} near an altitude of 200 km, and the upper limit of the C_{hot}-C_{hot} collision frequency is estimated to be on the order of 10^{-8} s^{-1}. Thus, the collisions between hot carbon atoms are safely disregarded, since their effect is negligible. Along the same lines, the O_{hot}-O_{hot} collision is also not considered in the study of hot oxygen corona, due to the relatively low collision frequency.

All scatterings occurring between a nascent hot carbon and background species in the simulation are assumed to be elastic hard sphere collisions (isotropic scattering). Both C_{hot}-O_{cold} and C_{hot}-$CO_{2,\ cold}$ collision cross sections are approximated to be 3×10^{-15} cm^2. Other current studies might suggest different cross sections and angular scattering models, such as an integrated cross section (*i.e.*, a forward scattering collision scheme). For hot oxygen, a few studies [*e.g., Krestyanikova and Shematovich,* 2005; *Fox and Hać*, 2009; *Fox and Hać*, 2014] have examined the effects of employing differential scattering cross sections for O_{hot}-O_{cold} and O_{hot}-$CO_{2,\ cold}$ collisions. This thesis also presents the investigation that compares the effects of using different scattering approximations (isotropic and forward scattering) on hot oxygen

population. As in the case of the hot carbon study, the cross section of O_{hot}-O_{cold} collisions is also approximated to be 3×10^{-15} cm^2. If a considerable reassessment is required for collisions, the overall result is expected to reflect the difference. For example, different collision frequencies resulting from using reassessed scattering models can affect the changes in the velocity distribution of nascent hot carbon and the total global escape rates. As has been done in other studies [*e.g., Fox and Hać*, 2009 – hot oxygen study], the effects of using different approximations for collisions on hot carbon escape should be investigated in the future and can easily be incorporated into AMPS without noticeable loss in computational efficiency.

In the coupled MTGCM/M-GITM and Mars-AMPS framework, the exobase is not designated as a fixed altitude that separates the collision (thermosphere) and collisionless (exosphere) regimes. Instead, this study considers the full transitional domain, which extends from the altitude where a hot particle produced in this region has a high probability to be thermalized to where the collision frequency is very low. The assumption is that this transitional domain exists from 135 km to 300 km altitude and has been confirmed by *Valeille et al.* [2010a] by a range of different test runs for hot oxygen production. In this region, the collision frequency that Mars-AMPS computes during the simulation decreases by an order of magnitude, which is from about a few 10^{-1} s^{-1} to 10^{-2} s^{-1}.

Chapter IV

Source mechanisms of hot O and hot C

The inventory of CO_2 and water on Mars is controlled mainly by the escape of C- and O-containing neutral atoms, molecules, and ions. In particular, heavy neutral atomic species, such as C and O, may escape from the atmosphere of Mars by nonthermal mechanisms that produce hot atoms with energy of the escape energy. In this chapter, major source mechanisms for hot C and hot O atoms, which are widely accepted by the majority of past modeling studies, are described. Other possible sources are also mentioned, but only the major source mechanisms are considered in the hot corona simulations in this thesis.

IV.1. Hot C source mechanisms

Carbon atoms are produced with enough energy to escape in the lower exosphere (around 200 km), through a number of photochemical mechanisms, such as photoelectron impact dissociation of CO, photodissociative ionization of CO, and photoelectron impact dissociative ionization of CO^+. Among these mechanisms, many of the previous studies have found that photodissociation of CO and dissociative recombination of CO^+ are the two important mechanisms that can produce suprathermal carbon with energy in excess of the escape energy of a carbon atom. *Nagy et al.* [2001] also considered the collision of hot oxygen with cold, thermal carbon as a potentially important source, but it was found to have negligible effect for Mars. Various sources were investigated with a 1D-spherical model by *Fox* [2004] using the solar

fluxes that were characterized with enhanced soft X-ray and different EUV fluxes. *Fox* [2004] concluded that the most important source of escaping carbon is predicted to be photodissociation of CO, followed by electron impact dissociation of CO and dissociative recombination of CO^+. While the main sources of hot carbon are not firmly agreed upon, this work assumes that photodissociation of CO and dissociative recombination of CO^+ are the two major sources of hot carbon in the Martian thermosphere. This assumption is based on the majority of the previous studies [*Cipriani et al.*, 2007; *Fox and Bakalian*, 2001; *Fox and Hać*, 1999; *Nagy et al.*, 2001]. Sputtering of the upper thermosphere by energetic pickup ions [*Leblanc and Johnson,* 2002] is also likely to be an important loss mechanism for atomic carbon, but including this in an equivalent full 3D description is beyond the scope of this study.

IV.1.1. Photodissociation of CO

The most prominent current source of escaping hot atomic carbon is expected to be photodissociation of CO, which is highly sensitive to the solar UV flux. It is assumed that, in the reaction,

$$CO(X^1\Sigma^+) + h\nu \rightarrow C(^3P) + O(^3P), \quad (4.1)$$

the produced C and O are both in their ground state with the excess energies [*Huebner et al.*, 1992] distributed in accordance with the laws of conservation of momentum and energy. Studies of this reaction [*e.g.*, *Krupenie,* 1965; *Fox and Black,* 1989; *Torr et al.,* 1979] have shown that the threshold for the dissociation of $CO(X^1\Sigma^+)$ to the ground states of C and O is at $\lambda = 1117.8$ Å. The dissociation occurs between $\lambda = 885$ Å and this threshold by line absorption. The photodissociation frequencies are adopted from *Fox and Black* [1989], which are $4.4 \times 10^{-7} s^{-1}$ and $1.21 \times 10^{-6}\ s^{-1}$ for the low and high solar activity cases, respectively (scaled to 1 AU

heliocentric distance). These frequencies are scaled to the Martian heliocentric distance for L_s = 180°. The attenuation of the solar flux by the atmosphere is not considered in this work since the photoabsorption cross sections for CO and CO_2 are about 2 orders of magnitude smaller than the collision cross section between a nascent hot carbon and background species ($\sigma_{photoabsorption} \sim 10^{-17}$ cm^2 [*Torr et al.,* 1979] for both CO and CO_2; $\sigma_{collision} \sim 10^{-15}$ cm^2). This implies that the altitude where the attenuation is important would be at lower altitudes, where the most of nascent hot carbon atoms are thermalized and have an extremely small probability to escape.

IV.1.2. Dissociative recombination of CO^+

The dissociative recombination of CO^+ results in a number of energetic channels,

$$CO^+(X^2\Sigma^+, v = 0) + e \rightarrow C(^3P) + O(^3P) + 2.90 \text{ eV [C1]},$$

$$CO^+(X^2\Sigma^+, v = 0) + e \rightarrow C(^1D) + O(^3P) + 1.64 \text{ eV [C2]},$$

$$CO^+(X^2\Sigma^+, v = 0) + e \rightarrow C(^3P) + O(^1D) + 0.94 \text{ eV [C3]}, \quad (4.2)$$

$$CO^+(X^2\Sigma^+, v = 0) + e \rightarrow C(^1S) + O(^3P) + 0.22 \text{ eV [C4]},$$

$$CO^+(X^2\Sigma^+, v = 0) + e \rightarrow C(^1D) + O(^1D) - 0.33 \text{ eV [C5]}.$$

CO^+ is one of the minor heavy ions, which has been known as a nonnegligible source of hot O and hot C through the dissociative recombination mechanism in the Martian upper atmosphere. The CO^+ ion is quite different from the O_2^+ ion, the major ion in the ionosphere. O_2^+ is a homonuclear diatomic molecular ion (*e.g.,* N_2^+) and has zero net dipole moment, since the symmetry never changes. The infrared transition from excited vibrational levels to the ground state is forbidden by the vibrational selection rule. Thus, O_2^+ may be nonthermal in excited

vibrational levels according to the vibrational distribution. The vibrational distribution of O_2^+ will be further discussed in the chapter for hot O study.

Unlike O_2^+, CO^+ is a heteronuclear diatomic molecular ion that owns a permanent dipole moment, which changes in magnitude as CO^+ vibrates. CO^+ in electronic and vibrational ground state has a sizable dipole moment of 2.77 D [*Rosén et al*., 1998], where the electric dipole moment is defined as charge times displacement in a CGS unit of D, the *debye* length. The radiative dipole-allowed transitions are more efficient for CO^+, limiting the actual fraction of vibrationally excited ions [*Fox and Hać,* 1999]. Since the ion temperature in the upper atmosphere is high enough for the radiative relaxation of the excited CO^+ ion, CO^+ is expected to be fully relaxed to the ground electronic and vibrational states under most conditions in the ionosphere before it recombines with an electron.

The energy released from the reaction depends on the exothermicity of the involved channel as shown in equation (4.2). The corresponding branching ratios for the channels have been measured by *Rosén et al*. [1998] at 0 eV relative energy between the CO^+ and the electron, which are 0.761, 0.145, 0.094, 0.0, respectively, from *C1* to *C4*, with *C5* being endothermic. The branching ratio is expected to vary with the center-of-mass collision energy. *Rosén et al*. [1998] carried out four different collision energy experiments to determine the final state distributions of the fragment from the dissociative recombination of CO^+. As shown in table 4.1, the higher collision energies allow an endothermic channel at 0 eV collision energy to become an exothermic with an enthalpy change in the reaction.

Center-of-mass collision energy (eV)	0	0.4	1.0	1.5
$C(^3P) + O(^3P)$ [*C1*]	76.1%	53%	39%	38%
$C(^1D) + O(^3P)$ [*C2*]	14.5%	34%	35%	35%
$C(^3P) + O(^1D)$ [*C3*]	9.4%	8%	15%	11%
$C(^1S) + O(^3P)$ [*C4*]	0.0%	0%	5%	5%
$C(^1D) + O(^1D)$ [*C5*]		5%	6%	11%
$C(^3P) + O(^1S)$				0%

Table 4.1. The final state distribution for four different relative collision energies. This table is Table 1 in the study done by *Rosén et al*. [1998].

The center-of-mass relative collision energy is defined as the detuning energy, which is calculated with the relative velocity between a parent ion and electron. Figure 4.1 shows the computed distribution of detuning energy, $E_d = \frac{m_e v_{ion-electron}^2}{2}$, as a function of altitude using the electron and ion temperature profile from MTGCM for the low solar activity case at equinox. As expected, the collision energy rapidly increases with increasing altitude due to larger ion and electron temperatures.

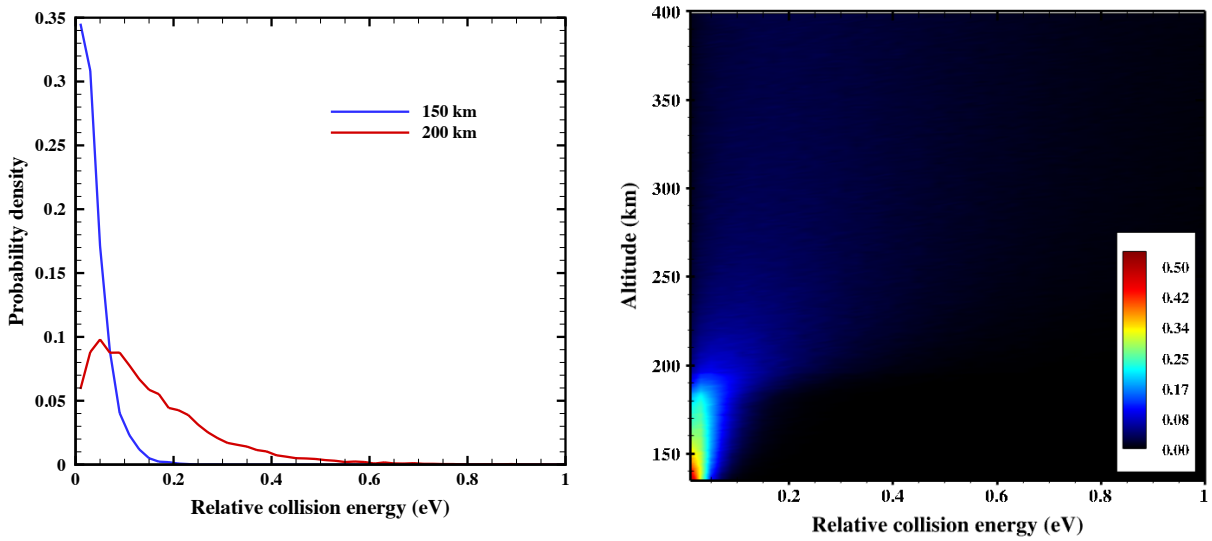

(a) (b)

Figure 4.1. (a) Distribution of the detuning energy, E_d, of parent ion and electron in dissociative recombination of CO^+ reaction at an altitude of 150 km (blue) and 200 km (red), and (b) detuning energy distribution in 3D for the altitude range of 100 km – 500 km for low solar activity at autumnal equinox.

The ion temperature does not exceed ~1000 K below an altitude of ~250 km, for instance, for the low solar activity case, the branching ratio variation from higher relative collision energies can be safely disregarded in the computation of dissociative recombination of CO^+ (*i.e.,* branching ratio is constant for all altitude range). Thus, this study considers only *C1* - *C4* at 0 eV relative collision energy as available exothermic channels for production of hot C.

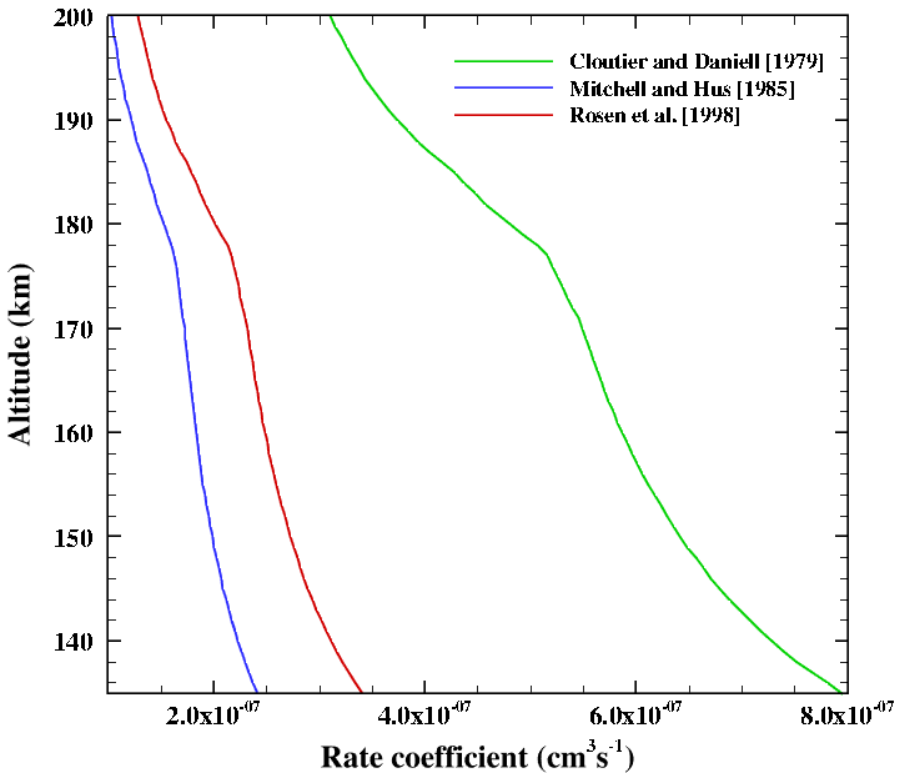

Figure 4.2. Altitude profiles of the rate coefficients for dissociative recombination of CO^+, computed for the equinox and low solar activity case at SZA 60°.

The rate coefficient chosen for this hot C study is,

$$\alpha(T_e) = 2.75\times10^{-7}\left(\frac{300}{T_e}\right)^{0.55} cm^3 s^{-1},$$

which is derived from an experiment by *Rosén et al*. [1998]. *Cloutier and Daniell* [1979] also reported $\alpha(T_e) = 6.47 \times 10^{-7} (300/T_e)^{0.53}$ cm^3 s^{-1}. *Mitchell and Hus* [1985] measured $\alpha(T_e) = 2.0 \times 10^{-7} (300/T_e)^{0.48}$ cm^3 s^{-1} in the merged electron-ion beam experiment (MEIBEI). Figure 4.2 shows the rate coefficients from these different groups. The largest rate coefficient is measured by *Cloutier and Daniell* [1979], which is more than twice larger than the one chosen for this study. This variation of the rate coefficients does not play an important role in the production of hot C. Since CO^+ and electron are lost via dissociative recombination of CO^+, the variation in the rate coefficients is adjusted with the change in the densities of CO^+ and electron.

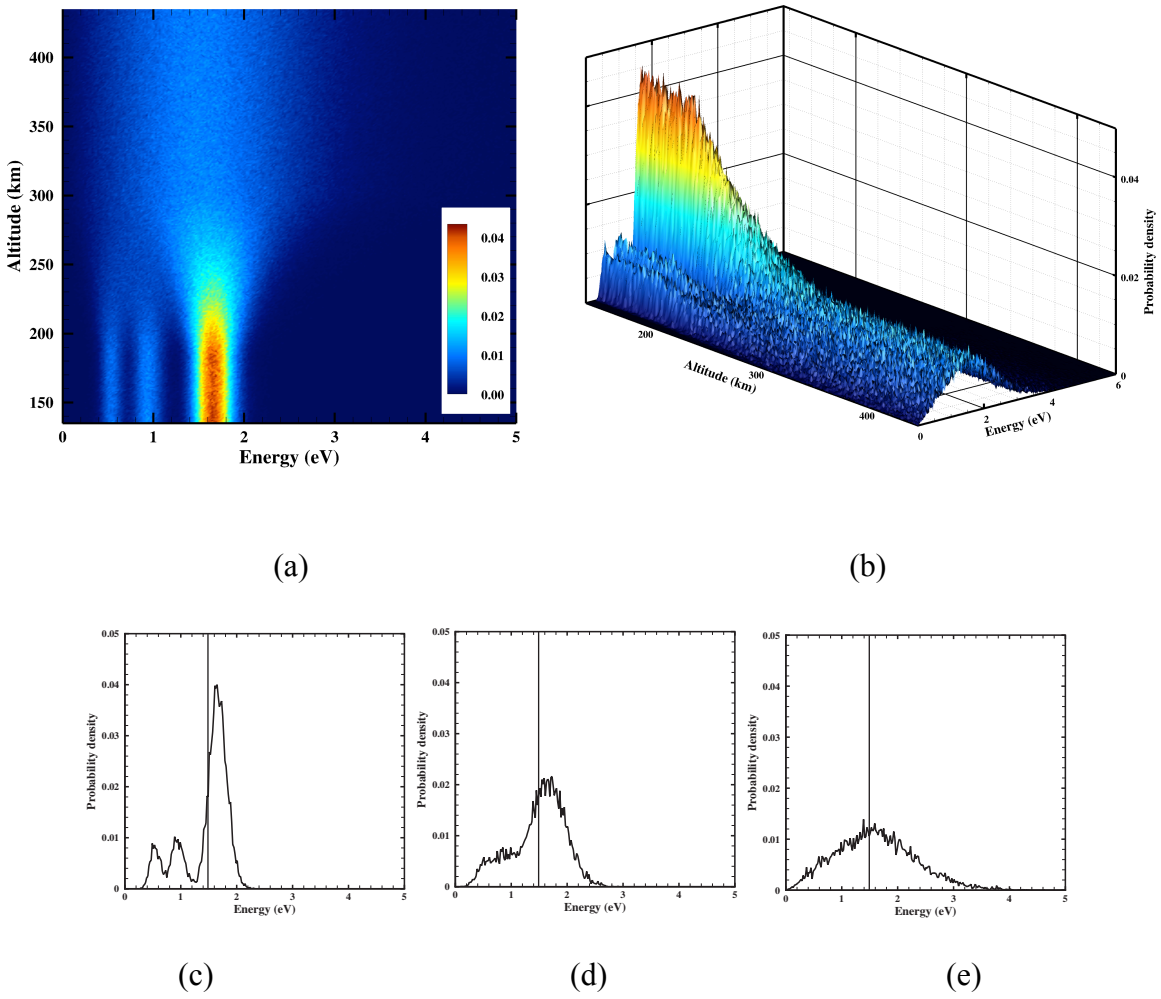

(a) (b)

(c) (d) (e)

Figure 4.3. Energy distribution of the nascent hot C from dissociative recombination of CO^+ in (a) 2D (the contour shows the probability density), (b) 3D, and 1D at altitudes of (c) 190 km, (d) 240 km, and (e) 300 km. The vertical line in 1D plots indicates the escape energy of hot C (~1.48 eV).

The energy distributions (velocity distribution) of nascent hot carbon atoms produced by dissociative recombination of CO^+ are shown for different altitudes in figure 4.2. Figure 4.2a and 4.2b visualize the changes in the structure of the energy distribution as a function of altitude. The peaks in figure 4.2 (c, d, e) correspond to the *C1*, *C2*, and *C3* channels in dissociative recombination of CO^+. The vertical line indicates the escape energy, ~1.48 eV, of a hot carbon

atom. CO^+ density in the ionospheric description always peaks above ~200 km where the electron density decreases exponentially. The computed production rate peaks in the altitude region between 150 km - 180 km and decreases by about an order of magnitude near an altitude of 200 km. Because of the ionospheric peak height of CO^+ density, the production of hot carbon is assumed to be still important in vicinity of an altitude of 200 km. Ion temperature increases as altitude increases, which results in the broadening of the peak as shown in figure 4.2 (c, d, e). As the probability density for the three available channels decreases with increasing altitude, the peaks are less distinctive and the average energy becomes larger.

IV.1.3. Possible other sources of hot C

In addition to photodissociation of CO and dissociative recombination of CO^+, as well as ion sputtering of the atmosphere discussed in chapter 5.3.5, a number of other nonthermal mechanisms have been reported as potential sources of hot C that may escape to space. The possible sources of hot C include [*McElroy,* 1977; *Fox and Bakalian,* 2001],

Photoelectron impact dissociation of CO,

$$\mathrm{CO} + e^* \rightarrow \mathrm{C} + \mathrm{O} + e, \tag{4.3}$$

Photoelectron impact dissociation of CO_2,

$$\mathrm{CO_2} + e^* \rightarrow \mathrm{C} + \mathrm{O_2} + e, \tag{4.4}$$

$$\rightarrow \mathrm{C} + \mathrm{O} + \mathrm{O} + e, \tag{4.5}$$

Dissociative recombination of CO_2^+,

$$\mathrm{CO_2}^+ + e \rightarrow \mathrm{C} + \mathrm{O_2}, \tag{4.6}$$

Photodissociative ionization of CO,

$$\mathrm{CO} + h\nu \rightarrow \mathrm{C} + \mathrm{O}^+ + e, \tag{4.7}$$

Photoelectron impact dissociative ionization,

$$CO + e^* \rightarrow C + O^+ + 2e, \quad (4.8)$$

Dissociative charge transfer reaction of O^{++} with CO,

$$O^{++} + CO \rightarrow C + O^+ + O^+. \quad (4.9)$$

Although all these processes are potential source mechanisms that produce escaping hot C, there is little information on the production of hot C from these processes. Moreover, except for the photoelectron impact dissociation of CO, these alternative potential mechanisms induce the escape of hot C about 1 – 3 orders of magnitudes less than the two source mechanisms assumed in this thesis (*i.e.,* photodissociation of CO and dissociative recombination of CO^+) [*Fox and Bakalian,* 2001]. In order to confirm the dominant source mechanisms for hot C, these various other source mechanisms need to be examined by our coupled framework.

IV.2. Hot O source mechanisms

IV.2.1. Dissociative recombination of O_2^+

At the current epoch, dissociative recombination of O_2^+ is known as a main source of generating the Martian hot oxygen corona. O atoms are produced with an energy above that of the local ambient O atoms via five different exothermic channels,

$$O_2^+(X^2\Pi_g, v = 0) + e \rightarrow O(^3P) + O(^3P) + 6.98 \text{ eV [C1]},$$

$$O_2^+(X^2\Pi_g, v = 0) + e \rightarrow O(^1D) + O(^3P) + 5.02 \text{ eV [C2]},$$

$$O_2^+(X^2\Pi_g, v = 0) + e \rightarrow O(^1S) + O(^3P) + 2.80 \text{ eV [C3]}, \quad (4.10)$$

$$O_2^+(X^2\Pi_g, v = 0) + e \rightarrow O(^1D) + O(^1D) + 3.05 \text{ eV [C4]},$$

$$O_2^+(X^2\Pi_g, v = 0) + e \rightarrow O(^1D) + O(^1S) + 0.83 \text{ eV [C5]}.$$

The excess energies are available from energetically allowed channels in the reaction, which are valid for the ground state of the parent ion, O_2^+. Due to conservation of momentum and energy, these excess energies are shared equally in the center of mass frame by the two nascent hot O atoms.

For ground state O_2^+ ions and cold electrons with 0 eV relative collision energy, *Kella et al.* [1997] have measured the quantum yield for the final states of O atoms, which are found to be 0.22, 0.42, 0.31, and 0.05 for the main branches, *C1*, *C2*, *C4*, and *C5*, respectively. As for dissociative recombination of CO^+ that produces a hot carbon atom, the relative collision energy for dissociative recombination of O_2^+ exhibits large peak at lower altitudes and decreases rapidly at higher altitudes.

IV.2.2. Rate Coefficients

The measurements of the rate coefficient for dissociative recombination of O_2^+ have been carried out by many studies. *Hodges* [2000] adopted the rate coefficient of $1.5 \times 10^{-7} (300/T_e)^{0.55}$ cm^3 s^{-1} for the dissociative recombination reaction. *Peverall et al.* [2005] performed experiments in a heavy ion storage ring (CRYRING) and, by averaging the dissociative recombination cross section, derived the rate coefficients of $\alpha(T_e) = 2.4 \times 10^{-7} (300/T_e)^{0.70\pm0.01}$ cm^3 s^{-1}. *Walls and Dunn* [1974] found $\alpha(T_e) = 1.9 \times 10^{-7} (300/T_e)^{0.66}$ cm^3 s^{-1} for the electron temperature range of $100 < T_e < 2500$ K in an ion-trap experiment. In this thesis, the rate coefficient reported by *Mehr and Biondi* [1969] is chosen following the majority of previous hot O investigation [*e.g., Cipriani et al.*, 2007; *Fox and Hać*, 2009; *Valeille et al.*, 2009a, 2009b; *Valeille et al.*, 2010a], which is $\alpha(T_e) = 1.95 \times 10^{-7} (300/T_e)^{0.7}$ cm^3 s^{-1} for $300 < T_e < 1200$ K and $7.39 \times 10^{-8} (1200/T_e)^{0.56}$ cm^3 s^{-1} for $1200 < T_e < 5000$ K.

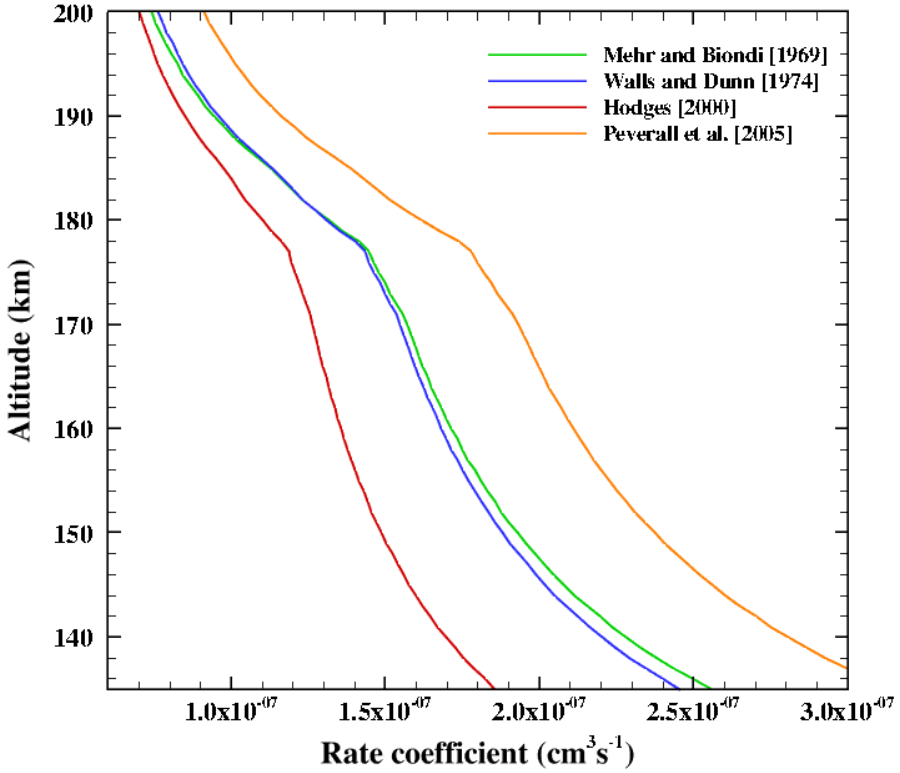

Figure 4.4. Altitude profiles of the rate coefficients for dissociative recombination of O_2^+, computed for the equinox and low solar activity case at SZA 60°.

As noted in section 4.1.2, the choice of the rate coefficient does not have a large effect on the result. Figure 4.4 shows the altitude profiles of the rate coefficients. Overall, the variation among the rate coefficient is small. At an altitude of ~200 km, this variation becomes even smaller and converges. The main loss mechanism of O_2^+ is dissociative recombination of O_2^+. Therefore, due to the photochemical equilibrium, the change in the rate coefficient is balanced by the change in the O_2^+ density by the loss and production mechanisms [*Fox and Hać,* 2009].

IV.2.3. Vibrational distribution of O_2^+

As mentioned in a previous section (chapter 4.1.2; hot carbon source mechanism), O_2^+, is a homonuclear diatomic ion with zero net dipole moment. In the lower thermosphere, the vibrational levels of O_2^+ ions are in thermal distribution due to the high density of the background atmosphere. The infrequent-collision regime, the upper thermosphere, allows the nonthermal distribution of vibrational levels, where O_2^+ ions are likely to remain in the levels in which they are produced. A more detailed investigation of the vibrational levels of O_2^+ is described in the hot O study (chapter 8).

Most of O_2^+ ions (~99%) in the Martian atmosphere are in their electronic and vibrational ground state, which is assumed for the hot O study in this thesis [*Fox and Hać*, 2009]. Utilizing this assumption, figure 4.3 displays the energy distribution of nascent O from the dissociative recombination reaction at several different altitudes. The overall altitude dependency of the distribution is also shown with the color contour representing the probability density. The nascent O produced in the lower atmosphere is highly affected by the exothermicities of the source reaction, whereas at the high altitudes the peaks in the spectra are broadened to wider range of energy, as in the case of dissociative recombination of CO^+, due to the increasing ion temperature with increasing altitude [*Fox and Hać*, 2009].

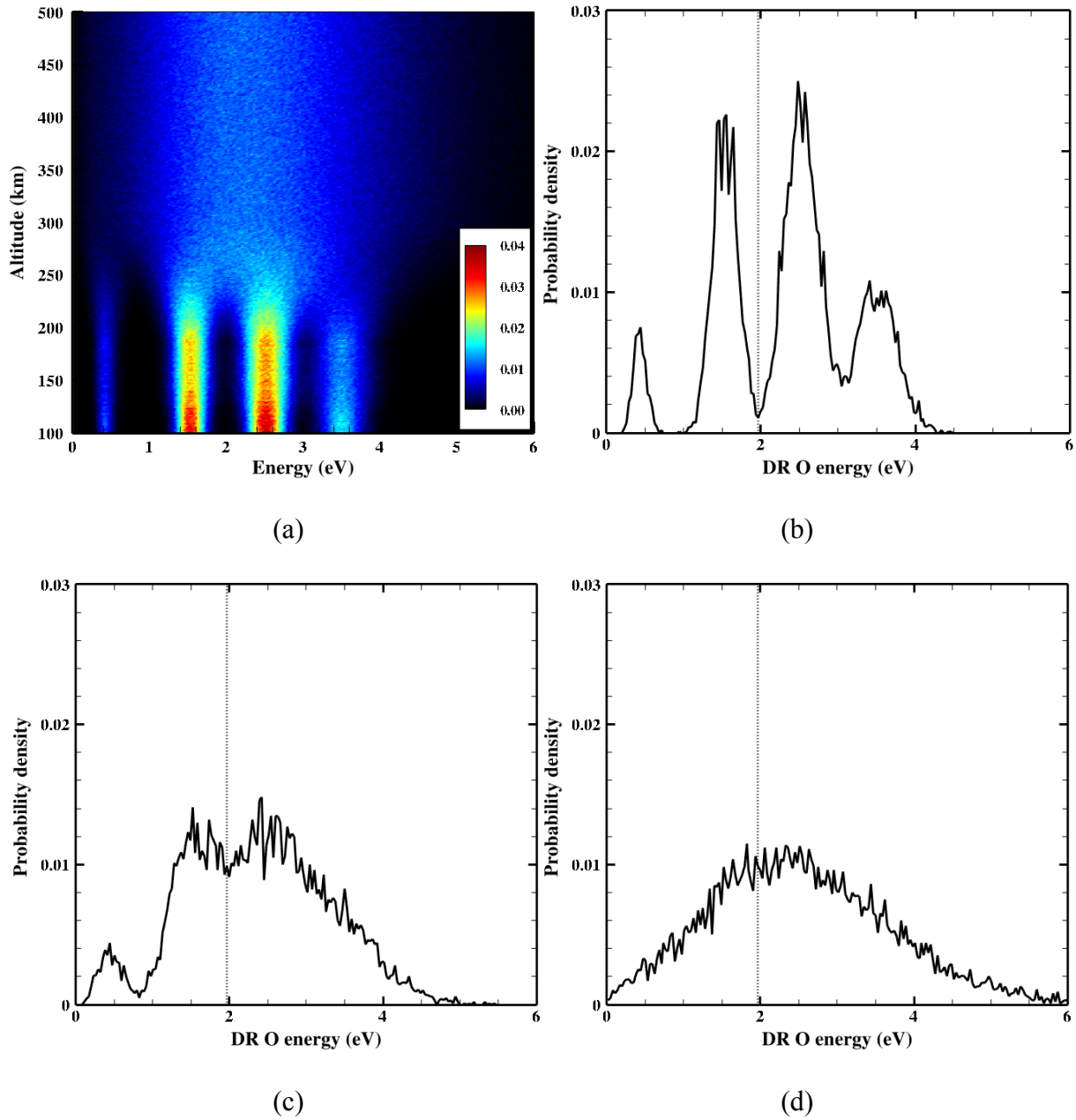

Figure 4.5. Energy distribution of nascent O computed from dissociative recombination of O_2^+. (a) 2D view of O energy distribution as a function of altitude and energy spectra at altitudes of (b) 190km, (c) 240 km, and (d) 300 km. The dotted vertical line indicates the escape energy of O (~1.97 eV).

IV.2.4. Possible other sources of hot O

IV.2.4.1. Dissociative recombination of CO^+

The daughter species of dissociative recombination of CO^+, $CO^+ + e \rightarrow C^* + O^*$ ($\Delta E = -0.33\ eV - 2.90eV$), are atomic carbon and oxygen as shown in equation 4.2. Although this reaction is heavily investigated in the hot C study, it is also a nonnegligible source of the Martian hot O corona. Depending on the mass of C and O, both of the nascent carbon and oxygen atoms can obtain energy to escape. The main branch among the exothermic channels in the reaction is the channel *C1*. *C1* produces a carbon atom and oxygen atom in triplet P state.

IV.2.4.2. Photodissociation of CO_2

CO_2 is the dominant constituent in the Martin thermosphere. The absorption of UV photons by CO_2 is one of the important mechanisms on Mars, and the relatively simple structure of CO_2 has enabled detailed investigation on both experiment and theory to be performed [*e.g., Lawrence,* 1972; *Fox and Dalgarno,* 1979; *Stolow and Lee,* 1992]. Photodissociation of CO_2 has also been mentioned in some studies [*e.g., Fox and Dalgarno,* 1979; *Hodges,* 2002; *Feldman et al. 2011*] as a reaction that also produces hot O in the Martian atmosphere. *Feldman et al.* [2011] reported that an additional constraint on hot O model may come from the forbidden OI 2972Å (^{1}S-^{3}P) line by both photodissociation of CO_2 and dissociative recombination of O_2^+, which is investigated by SPICAM UV limb data [*Simon et al.,* 2009]. CO_2 photodissociates into CO and O via two possible channels in the wavelength range 140 – 170 nm,

$$CO_2 + v \rightarrow CO(X^1\Sigma^+) + O(^3P), \quad (4.11)$$

$$CO_2 + v \rightarrow CO(X^1\Sigma^+) + O(^1D), \quad (4.12)$$

where the main branch produces $O(^1D)$ with excess energies of about 4.34 eV and 4.55 eV for the low and high solar activity cases, respectively. Figure 4.4, generated by *Fox and Dalgarno* [1979], shows the computed altitude profiles of the production rates of the major sources of $O(^1D)$ on Mars. The dominant source is the dissociative recombination reaction, and the production rate of photodissociation of CO_2 is lower by more than an order of magnitude at higher altitudes.

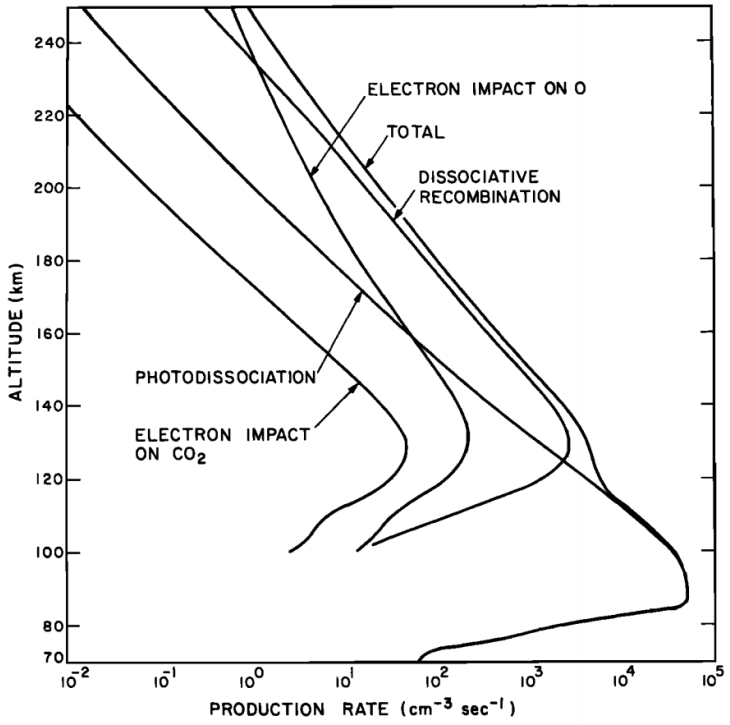

Figure 4.6. The computed production rate altitude profiles of the major sources of $O(^1D)$. This is the figure 11 in the study of *Fox and Dalgarno* [1979].

Chapter V

Hot carbon corona

– Mechanisms and Structure for Low Solar Activity at Equinox

This chapter focuses on the general mechanisms and structure of the Martian hot carbon corona that is simulated at a fixed condition: equinox and low solar activity. The variations of the hot carbon corona at other solar and seasonal conditions are described in chapter 6. The features in the thermosphere and ionosphere, which are important for the production and thermalization of hot C, will be addressed and followed by investigation of the simulated hot C corona. The simulation results presented in this chapter have already appeared in the refereed journal article by *Lee et al.* [2014a].

V.1. Introduction to hot carbon corona investigation

CO_2 is the major neutral species in the thermosphere. Its inventory at Mars is constrained by either the escape of carbon as an atom or molecule, such as CO_2, CO, or C, or C-containing ions [*Fox and Hać,* 1999], or the formation of carbonate mineral deposits to the crust by chemical interactions [*Jakosky*, 1991]. Among a number of escape mechanisms, only nonthermal processes can induce the creation of a carbon atom with energy above the escape energy of about 1.48 eV. A carbon atom is considered to be "hot carbon" when the excessive energy from the source mechanisms is added to a nascent carbon atom. Depending on the availability of enough

energy to escape, the hot carbon in the corona may escape to space or fall back to the atmosphere by gravitational attraction after traveling along its ballistic trajectory.

On Mars, the most important nonthermal reaction for the production of hot carbon is suggested to be photodissociation of CO [*e.g.*, *Fox*, 2004; *Fox and Bakalian*, 2001, *Nagy et al.*, 2001]. Among several other potential source mechanisms, dissociative recombination of CO^+ has been suggested as another nonnegligible source that must be considered in the computation of the total escape rate of hot carbon [*e.g.*, *Fox,* 2004; *Fox and Hać*, 1999; *Fox and Bakalian*, 2001, *Nagy et al.*, 2001].

Although the hot carbon corona at Venus has been observed by the UV spectrometer aboard the Pioneer Venus Orbiter [*e.g., Paxton*, 1985], the Martian hot carbon corona has not yet been observed. The new Mars Scout mission, Mars Atmosphere and Volatile EvolutioN (MAVEN), is presently on its way to Mars and is expected to expand our knowledge on the detailed structure of the Martian hot corona. For the atmospheric escape mechanisms, thorough numerical modeling has been developed for a better understanding of the atmospheric escape in both current and evolutionary aspects. However, most of the works have focused on the hot oxygen case [*e.g., Cipriani et al.*, 2007; *Fox and Hać*, 1997b; *Fox and Hać*, 2009; *Hodges*, 2000; *Kim et al.*, 1998; *Valeille et al.*, 2009a, 2009b, 2010a, 2010b; *Yagi et al.*, 2012]; only a few numerical approaches have been carried out for the hot carbon investigation [*Cipriani et al.*, 2007; *Fox,* 2004; *Fox and Bakalian*, 2001; *Fox and Hać*, 1999; *Nagy et al.*, 2001], and none have looked into the inherent 3D nature of the hot carbon corona.

Among many mechanisms, neutral species in the hot coronae can be ionized by photons, electron impacts or charge exchange reactions via the interactions between the upper atmosphere and the solar wind [*e.g.*, *Luhmann et al.*, 1992; *Jakosky et al.*, 1994; Johnson, 1994; *Leblanc and*

Johnson, 2001]. First observed by the PHOBOS-2 spacecraft [*Lundin et al.*, 1990, *Verigin et al.*, 1991], these heavy ions newly produced from the interaction of the solar wind with the exosphere can (1) be picked up by the convection fields of the solar wind plasma and directly lost to space or (2) reimpact the atmosphere and initiate the momentum transfer events, causing neutrals to escape from the hot coronae, known as sputtering [*Luhmann and Kozyra*, 1991]. This physics of the Mars-solar wind interaction has been successfully simulated and addressed by various models with unique techniques. Recent model studies have provided, for example, the upper limits to the outflow of heavy ions [*Fox*, 1997] and realistic descriptions of pickup O^+ ion distributions around Mars using multispecies 3D MHD models [*Liu et al.*, 1999, 2001; *Ma et al.*, 2004; Ma and Nagy, 2007; *Fang et al.*, 2008]. *Fang et al.* [2013] have carried out case studies of pickup ion precipitation under various extreme solar wind conditions, and *Curry et al.* [2013] have extensively assessed the different source mechanisms of pickup ions. In the investigation of nonthermal atmospheric loss, these studies can serve as a significant tool for understanding the sputtering of hot O and hot C.

A number of numerical approaches have been carried out to estimate the CO_2 loss from the Martian atmosphere. *Fox and Hać* [1999] used 1D (spherical) Monte Carlo calculations to investigate the altitude-dependent velocity distributions of hot C produced from dissociative recombination of CO^+ only. They used a fixed exobase for each solar activity case and studied the effect of using different upper atmosphere conditions. *Fox and Bakalian* [2001] calculated the escape fluxes by using the "exobase approximation" for various photochemical mechanisms and found that photodissociation of CO and dissociative recombination of CO^+ are the dominant source mechanisms of hot C. *Nagy et al.* [2001] used the two-stream approach to describe the hot C corona, which was also a one-dimensional study that adopted the production rates from *Fox*

and Hać [1999]. Interestingly, *Fox* [2004] included dissociative recombination reaction of CO_2^+ in their study and reported that the second most dominant source of hot C is electron impact dissociation of CO. *Cipriani et al.* [2007] used a 1D Monte Carlo test particle approach with the same thermospheric models as those of previous hot C studies. They reported a range of hot atom and molecule production and escape rates in the Martian upper atmosphere. Their reported escape rates of the hot C from dissociative recombination of CO^+ are somewhat lower than previously published values.

The Martian hot corona is formed from the upper thermosphere and ionosphere in which important mechanisms and dynamics take place. In order to model the Martian upper atmosphere self-consistently, a 3D global kinetic model is used to describe the physics of particle interaction and escape and a 3D thermosphere/ionosphere model to provide a description resolving the inherent limitations of the past 1D and 2D models. The model details, basic hot C corona structures, and resulting effects and advantages of a 3D atmosphere input have been discussed in the work of *Lee et al.* [2014a] to emphasize the need of inclusion of the thermosphere dynamics. *Lee et al.* [2014a] considered a fixed orbital position and solar cycle condition, the equinox and low solar activity case (EL), for the purpose of the rigorous investigation of the mechanisms in the upper atmosphere.

The Martian upper atmosphere and hot carbon corona are extensively described by a full 3D study of the exosphere presented here. The 3D Mars Thermosphere General Circulation Model (MTGCM) [e.g. *Bougher et al.*, 2006, 2009] provides all necessary thermospheric/ionospheric parameters as a set of inputs to the 3D kinetic particle simulator, AMPS [*Tenishev et al.*, 2008]. The framework of the coupled Mars-AMPS and MTGCM codes is addressed in detail in *Lee et al.* [2014a] and *Valeille et al.* [2009a, 2009b]. The first coupling

of the 3D AMPS and MTGCM with the 3D exospheric model has been successfully done to study the hot oxygen corona [*Valeille et al.*, 2009a, earlier version of the current model].

V.2. Characterization of the sources of hot carbon

V.2.1. Temperature and global winds

A strong coupling between the Mars lower and upper atmosphere has been confirmed by analysis of the aerobraking data from the Mars Global Surveyor (MGS) and Mars 2001 Odyssey (ODY) Accelerometer [*Bell et al.,* 2007; *Bougher et al.*, 1999, 2004, 2006; *Forbes et al.*, 2002; *Forget et al.*, 2009; *Keating et al.*, 2003; *Wilson*, 2002; *Withers et al.*, 2003]. Several physical processes also drive the solar cycle and seasonal variations of the Martian exospheric temperatures in the upper thermosphere and exosphere of Mars (at/above ~160 km). The dayside heat balance is primarily achieved by solar EUV-UV heating and molecular thermal conduction, with rather weak influence of CO_2 15-μm cooling [*Bougher et al.*, 1990, 1999, 2009, 2014a]. Mechanical adiabatic heating and cooling due to upwelling (dayside) and downwelling (nightside) motion from the global thermospheric circulation (including impact of tides and gravity waves) play a relatively important role in the thermospheric structure [*Bougher et al.*, 1990, 1999, 2000, 2009, 2014a].

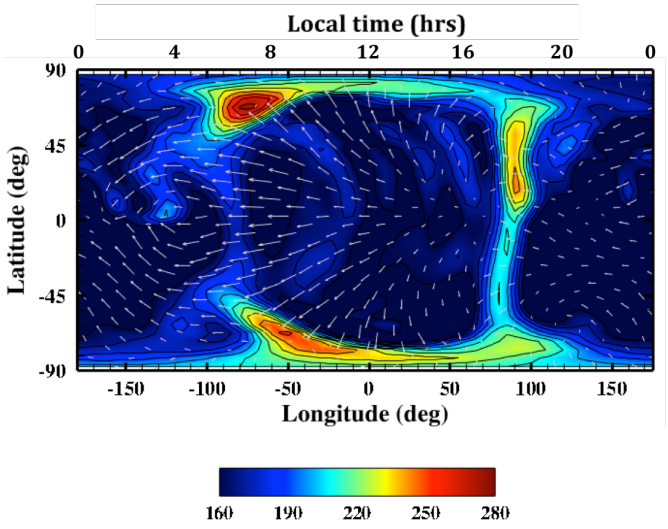

(a)

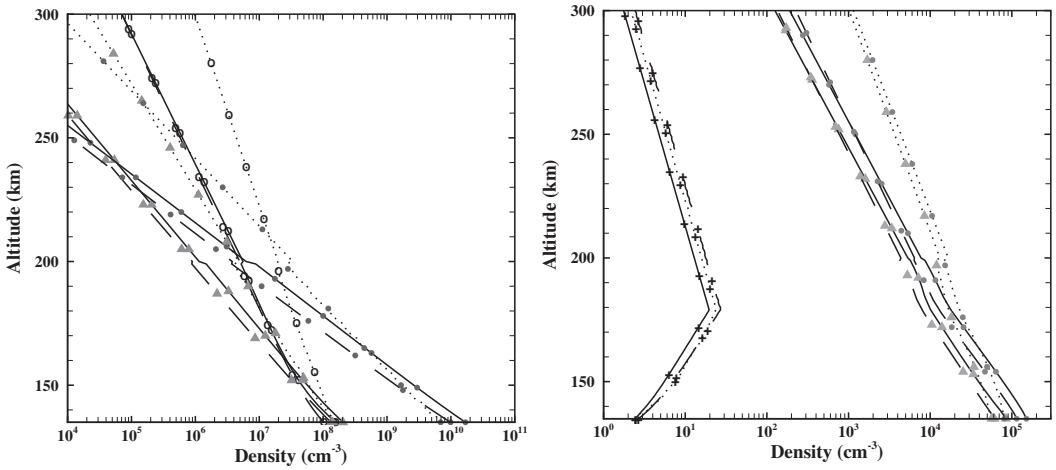

(b) (c)

Figure 5.1. (a) Neutral temperatures (T_n) near 200 km and density profiles of (b) neutral and (c) ion background species for three different SZA along the equatorial east (0°, solid; 60°, dashed; 80°, dotted) for the low solar and equinox case. Global wind magnitudes and directions are indicated as grey arrows. The highest temperature is ~270 – 280 K and shown in dark red. The contour shows the temperatures in units of K. In the profiles: CO (triangle), O (empty circle), CO_2 (filled circle), CO^+ (plus sign), O_2^+ (triangle), and electron (filled circle).

The background thermosphere and ionosphere are supplied by the MTGCM for corresponding solar activity and orbital position cases. According to this atmospheric input, the temperature of the Martian atmosphere increases slowly and becomes isothermal above ~160 -

200 km altitude (dependent on season), located near the bottom of the exosphere. The map of neutral temperature for the low solar activity and equinox case in figure 5.1a shows the high temperatures along the terminators and near the polar regions and the low temperatures in low and middle latitudes on the nightside. The highest temperature located near the North pole on the morning terminator is about 270 K, and the lowest temperature is about 110 K located near the anti-subsolar point and high latitudes on the southern hemisphere. The high latitude region and most of the dayside region are found to display the global average exospheric temperature of about 170 K. The Coriolis forces on the atmospheric circulation (as influenced by the planetary rotation) are evident; the zonal flow is minimum at the evening terminator and maximum at the morning terminator. Thermal lag, like that of Earth, appears as the offsets of peak temperatures from the subsolar point toward the mid-afternoon [*e.g., Bougher et al.* 1999, 2000]. The "heat island" is also shown (at about local time (LT) = 0200), which is due the convergence and adiabatic heating from subsiding flow by the modified thermospheric winds [*Bougher et al.*, 1990].

The input background atmosphere for this work consists of 3 neutral species (O, CO_2, and CO) and 3 ionospheric species (e^-, O_2^+, and CO^+). Their densities are provided from 135 km to 200 km, as mentioned previously in the framework description (chapter 3). Altitude profiles of the densities of thermosphere and ionosphere species are presented in figure 5.1b and 5.1c, respectively, for several different solar zenith angles. The local variation of the background temperatures influences the distribution of the local background densities. As a result, the scale heights of the neutral and ion densities profiles become larger as solar zenith angle increases. This scale height variation is larger along a meridian than along the equator, due to the larger

temperature variation (about a factor of 1.5 between polar region and equator regions) for the equinox condition, the specific orbital position considered in this work.

V.2.2. Background neutral atmosphere / CO density distribution comparison with O and CO_2

The major neutral constituents in the upper Martian thermosphere and exosphere are O atoms and CO_2 molecules. CO_2 is the dominant neutral species in the lower thermosphere up to an altitude of about 180 - 220 km, depending on the solar activity. Because of the mass difference, the O density (having a larger scale height) surpasses the CO_2 density and becomes the dominant species in the upper thermosphere. As shown in figure 5.2b, the maximum densities of CO_2 are situated in middle latitude in the North on the evening terminator and at high latitude near the pole regions. The O density reaches its maximum on the nightside, from about midnight to LT = 0400 from low to middle latitude due to the strong convergence of the global wind system, whereas the minima are in the regions where the winds are weak or diverging (*i.e.*, on the dayside from low to middle latitude, figure 5.2a). While the CO_2 density is well distributed spatially in accordance with the neutral temperature distribution (*i.e.,* the maxima and minima are in the locations of high and low temperatures, respectively), O atoms are more efficiently transported by the atmospheric circulation due to their relatively lighter mass compared with CO_2. As shown in figure 5.2a and 5.2b, the spatial variation of the O density shows anticorrelation with that of the CO_2 density since the O density tends to be more responsive to the global wind system than the background temperature.

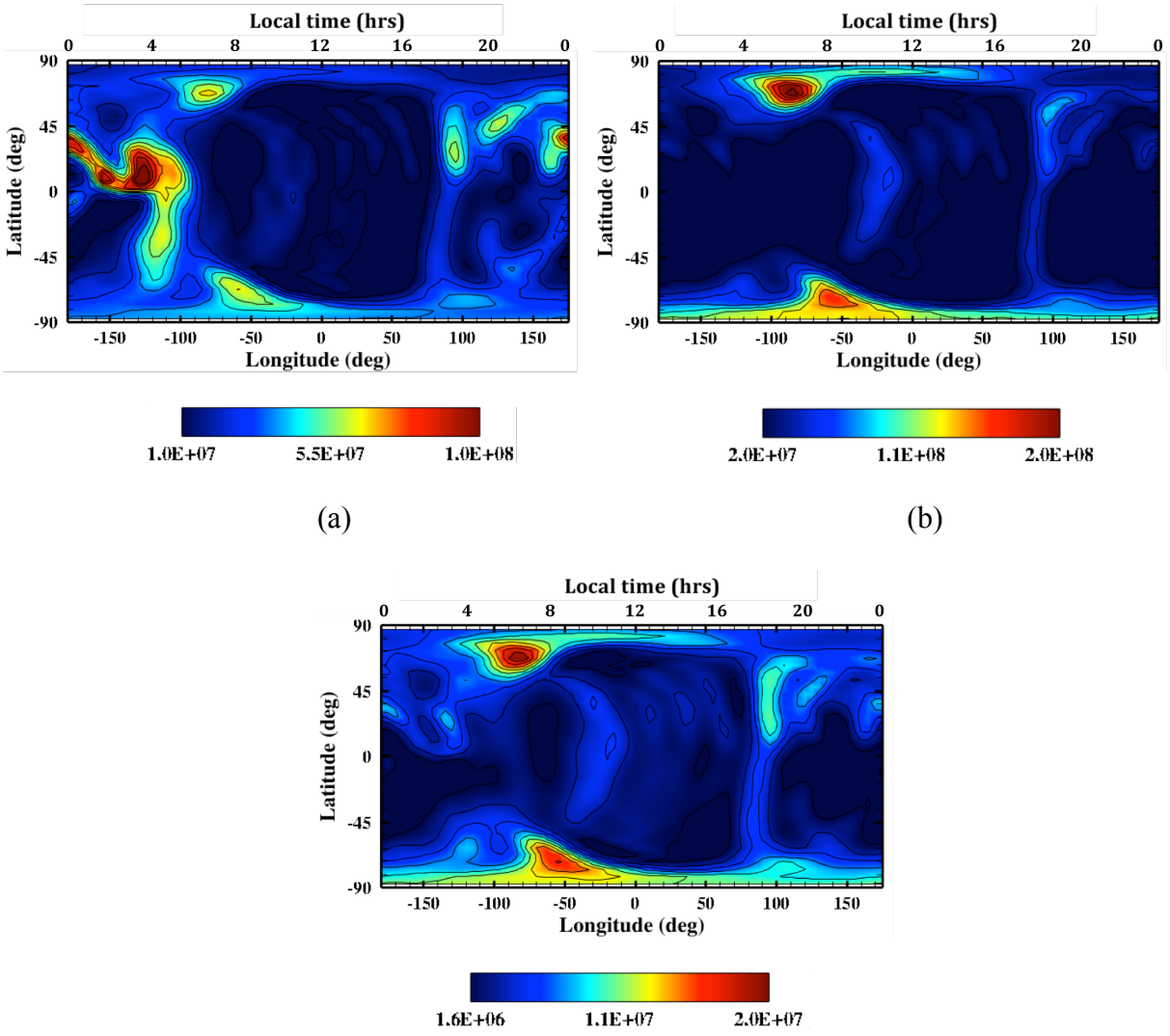

Figure 5.2. (a) Thermal O, (b) thermal CO_2, and (c) thermal CO density distributions for the low solar and equinox case near 200 km. The density is read as "(number on the contour) × 10^6 cm^{-3}." The maximum densities are ~ 210 × 10^6 cm^{-3}, 880 × 10^6 cm^{-3}, 47 × 10^6 cm^{-3} for O, CO^2, and CO, respectively, and are shown in dark red.

Carbon monoxide is one of the major neutral molecules and an important source of hot carbon as it is photodissociated by solar EUV in the upper thermosphere. As shown in figure 5.2c, the global distribution of CO exhibits features that reflect a mixture of the O and CO_2 distributions - more like CO_2 since CO is heavier than O, but slightly lighter than CO_2. The

maxima of the CO density coincide with those of the CO_2 distribution (figure 5.2b) plus some of the O maxima locations (figure 5.2a) in middle latitudes on the nightside. The minima are also in the low temperature and the diverging wind regions. The altitude profile of the CO density (figure 5.1b) shows the variation of the local density scale height at different solar zenith angles. The local scale height of CO density varies more along a meridian than along the equator. The local background temperature varies by about a factor of 1.5 from the subsolar point to the region near the North Pole. The corresponding local scale height of CO increases by a factor of ~1.3 as solar zenith angle increases. When the solar activity increases, the upper atmosphere absorbs more solar EUV flux and develops higher temperatures, stronger vertical winds, resulting in an expansion of thermosphere and enhancement of densities (*i.e.,* increase of scale heights). More detailed study on this solar cycle and seasonal variability in the thermosphere and ionosphere is discussed in chapter 6 (also in the submitted journal article *Lee et al.* [2014b]).

V.2.3. CO^+ ionospheric peak and its distribution compared with O_2^+

The major species in the Martian ionosphere, O_2^+, is produced through photodissociation of the major neutral species, CO_2, and charge exchange between CO_2^+ and O. *Valeille et al.* [2009a] showed that the horizontal distribution of O_2^+ density maxima are situated at the locations of CO_2 density maxima, where the peak density is found deep in the dayside thermosphere. Like O_2^+, CO^+ is a molecular ion, which follows a similar distribution pattern and variations with the solar cycle and seasons. The production of CO^+ is closely related to the densities of CO_2, the major background species below ~200 km altitude, and CO. The main source reactions in the Martian ionosphere are photoionization of CO and photodissociative ionization of CO_2,

$$CO + h\nu \rightarrow CO^+ + e, \quad (5.1)$$

$$CO_2 + h\nu \rightarrow CO^+ + O + e. \quad (5.2)$$

CO^+ is also produced by electron impact ionization of CO and electron impact dissociative ionization of CO_2. However, these last two reactions are not presently included in the MTGCM.

The major loss reaction of CO^+ ions is charge exchange between CO^+ and CO_2,

$$CO^+ + CO_2 \rightarrow CO_2^+ + CO, \quad (5.3)$$

which is a fast reaction. Charge exchange with O is another loss mechanism that removes CO^+ ions more effectively at higher altitude, where O is a major background species. As shown in the altitude profiles of the background densities from the input model (figure 5.1c), the major production of CO^+ takes place where the parent molecules, CO and CO_2, are abundant. At lower altitude regions, CO^+ ions are produced from the main source reactions and removed dominantly by charge exchange with CO_2. The CO^+ density keeps increasing up to an altitude of ~180 km (for the equinox and solar minimum case), because the rate of the loss process by charge exchange between CO^+ and CO_2 decreases faster than the rate of the production by photoionization of CO, while the loss process by O is negligible. At higher altitudes, the production rate by CO photoionization decreases faster than the dominant loss process rate by O (charge exchange with O), resulting in the CO^+ density decrease with altitude. The peak height of CO^+ varies as solar zenith angle increases and as solar activity and orbital position changes. As mentioned earlier, for the low solar activity and equinox case, the peak height is generally located above 200 km altitude because the effect of loss mechanisms on the net CO^+ density is minimized. Consequently, dissociative recombination of CO^+ is a nonnegligible source of nonthermal escape of hot carbon in the upper thermosphere and exosphere of Mars. On the

dayside, the existence of the CO^+ ionospheric peak in the upper thermosphere implies that the overall global escape rate of hot carbon resulting from dissociative recombination of CO^+ is quite sensitive to the background conditions (*i.e.*, T_e, T_n, T_i, and $n(CO^+)$) near/above ~200 km.

The MTGCM assumes photochemical equilibrium when solving for the ionosphere of Mars. Above an altitude of 200 km, the densities of all the ions are extrapolated in Mars-AMPS without considering ion transport. Ion transport at higher altitude strongly influences O^+, the major ionospheric species above about 200 km. O_2^+ as well as CO^+ densities also diffuse by ion transport at higher altitude. The extrapolated CO^+ density in the model already takes into account ion transport indirectly, since the referenced ion density profiles impose the upward velocity above an altitude where ion transport is important.

Figures 5.3b and 5.3c show the horizontal distribution of electron and O_2^+ densities near 200 km. These spatial distribution patterns resemble the neutral temperature distribution pattern on the dayside only, while CO^+ density pattern (figure 5.3a) shows the inverse relation. As for the altitude profile, the horizontal distribution of CO^+ is also linked to that of the parent molecules, CO and CO_2. The local CO^+ ions are effectively removed by the fast charge exchange with CO_2 and O. As a result, the spatial distribution of CO^+ displays anticorrelation with O and CO_2 distribution patterns.

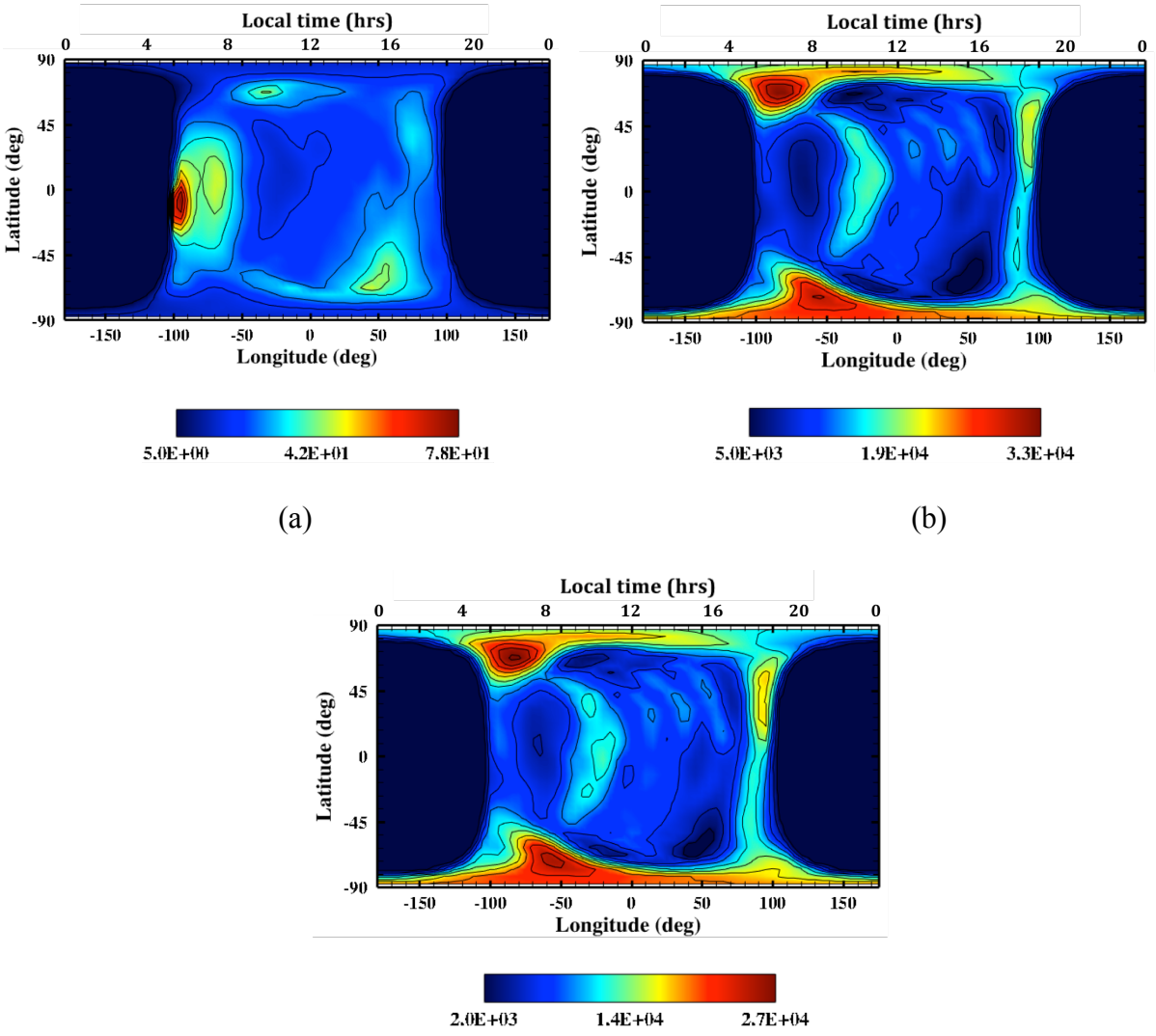

Figure 5.3. Density distributions near 200 km of (a) CO^+, (b) electron, and (c) O_2^+ for the low solar and equinox case. The density is read as "(number on the contour) × 10^3 cm^{-3}." The maximum densities are ~ 41 × 10^3 cm^{-3}, 45 × 10^3 cm^{-3}, 35 × 10^3 cm^{-3} for CO^+, electron, and O_2^+, respectively, and are shown in dark red.

The production rate of hot carbon from dissociative recombination of CO^+ is controlled by three factors: CO^+ and electron densities and the dissociative recombination coefficient, which varies as ${T_e}^{-0.55}$. Indeed, the hot carbon density peaks where the CO^+ density maxima and electron temperature minima are located. The maximum and minimum electron densities are

situated approximately at high and low neutral temperature regions. This is an additional implication of the analysis of the MGS occultations by *Bougher et al.* [2001, 2004], which showed that electron density peak heights could be a proxy for the longitudinal variations of the underlying neutral atmospheric structure over the seasons.

V.3. Model results and discussion

The global distribution of hot carbon resulting from the two main source reactions, photodissociation of CO and dissociative recombination of CO^+, is simulated. The coupled 3D Mars-AMPS and the 3D MTGCM codes provide a detailed description of the variations of the macroscopic parameters from a local to global perspective, which is essential for understanding the Martian hot exosphere more precisely and practically. As for the purpose of this work, the following discussion will investigate the different responses from the different source reactions and the spatial variation of the hot carbon corona for the specific solar condition and Mars season, low solar activity and equinox (F10.7 = 70; L_s = 180°).

V.3.1 Effects of the 3D thermosphere/ionosphere

As mentioned already, the hot carbon exosphere has been observed at Venus but not yet at Mars. Previous modeling efforts [*e.g., Fox and Hać*, 1999; *Nagy et al.*, 2001] have estimated and simulated the global loss of carbon. However, the previous models have lacked the important influences of the thermospheric and ionospheric structures and their variability, which can only be described by the 3D features of the atmosphere. These 3D features include the planetary rotation, global scale dynamics, sharp gradients near the terminators, hemispheric asymmetries, and polar warming effects. Mars rotates at a speed that is comparable to the average

thermospheric wind speed (zonal and meridional winds), which is about 240 m/s. This speed is fast enough to enable the rotation to be as effective (to the same degree) as the thermospheric winds for impacting the hot particle motion in the upper atmosphere, the structure of hot density profiles and, in turn, the return flux of hot particles back to the thermosphere [*Valeille et al.*, 2009a]. As mentioned earlier in this chapter, the full 3D description of hot corona using 3D thermosphere/ionosphere inputs allows one to capture more realistic features resulting from the main source mechanisms and interactions between hot species and the Martian upper atmosphere.

In addition to the effect of the planetary rotation and thermospheric winds, the spatial variation of hot carbon production is determined by the local thermospheric and ionospheric features. The production rate of hot carbon from photodissociation of CO follows the horizontal distribution of CO density. As mentioned, due to its slightly lighter mass (than that of CO_2), the distribution of thermal CO molecules exhibits the characteristics of both CO_2 and O, which are more responsive to the background temperature and the atmospheric circulation, respectively (section V.2.2, figure 5.2). In the same sense, different ionospheric asymmetries for the different ion species uniquely affect the spatial variations of the dissociative recombination of CO^+ production rate (section V.2.3, figure 5.3).

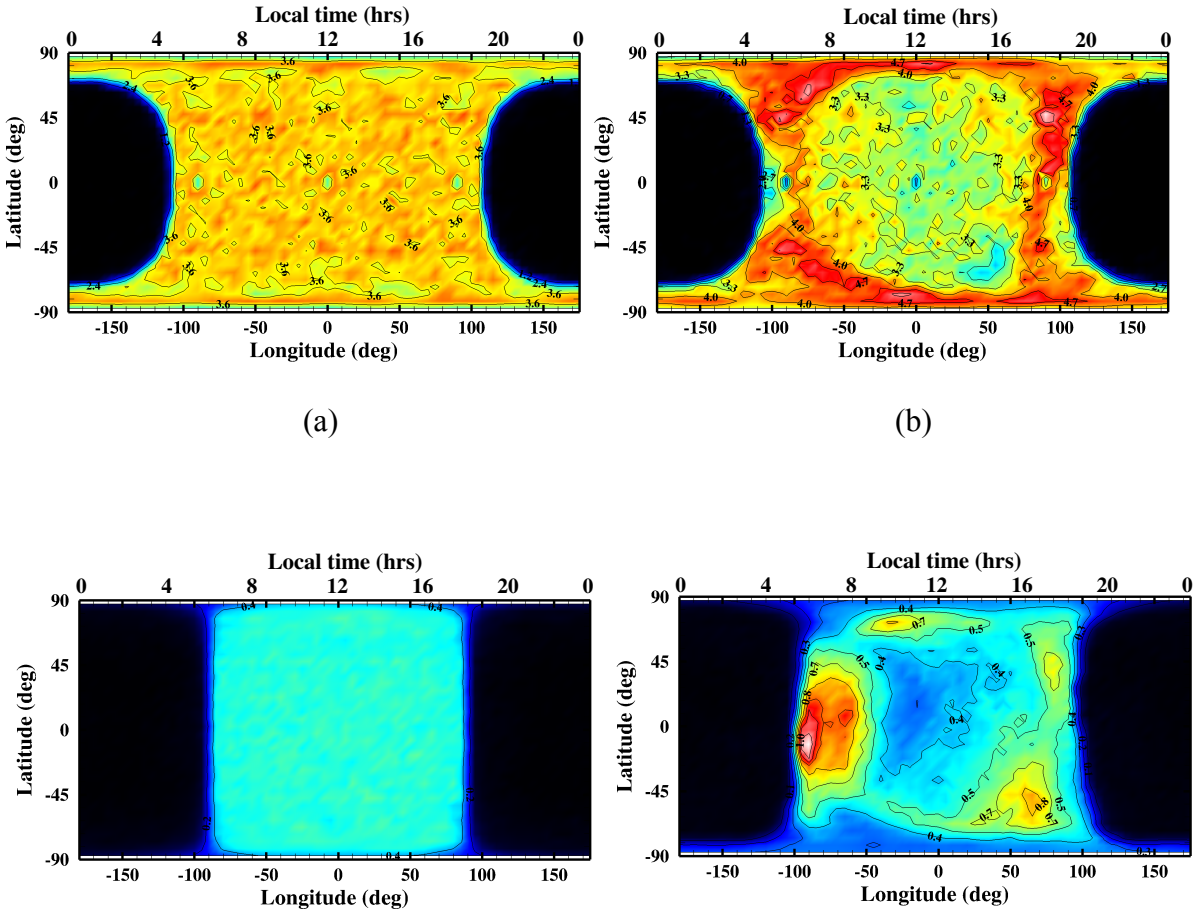

Figure 5.4. Latitude/longitude variations of simulated hot C density near 200 km in units of log density (cm^{-3}) produced from photodissociation of CO using 1D (a) and 3D (b) atmospheric inputs and from dissociative recombination of CO^+ using 1D (c) and 3D (d) atmosphere inputs.

Figure 5.4 shows the hot carbon density distributions by two source reactions (photodissociation of CO and dissociative recombination of CO^+) simulated with the atmosphere that is spherically symmetric over the dayside (1D, figure 5.4a and 5.4c) and full 3D atmospheric inputs (figure 5.4b and 5.4d). For the purpose of comparison between the effects of 1D and 3D atmospheric input, a column of atmosphere from the 3D atmospheric input at SZA 60° is extracted and distributed over the entire dayside. This particular column of the atmosphere is

chosen by assuming that the atmosphere at SZA 60° is the representative of the average over the dayside. Except for the small fluctuation of the density caused by the statistical noise in the 1D computation, the full 3D atmosphere input case evidently displays many important local features that the dayside-averaged case does not display.

As expected, the hot carbon density produced by photodissociation of CO (figure 5.4b) is spatially distributed in a pattern that is similar to the thermal CO distribution. The hot carbon atom production is continued onto the nightside (over the polar regions) except in the regions of the planet's shadow. Most of the escape happens on the dayside and is enhanced along the evening terminator, near the polar regions, and in middle and high latitudes on the morning terminator due to the subsiding atmospheric flow that impacts CO density.

The hot carbon resulting from dissociative recombination of CO^+ (figure 5.4d) is characterized by its local maximum escape located near the equator on the morning terminator, where the maxima of CO^+ density and the minima of electron temperature are located. The overall spatial distribution is very different from that of the hot oxygen, which is produced by dissociative recombination of O_2^+ (the major ion).

V.3.2. Hot carbon density

Hot carbon atoms are produced through various possible source mechanisms. As discussed in chapter 4, the majority of hot carbon is produced by photodissociation of CO. In this study, the next nonnegligible source is assumed to be dissociative recombination of CO^+ in this study. The different source reactions contribute different features to the Martian hot carbon corona along with the inherent planetary physics (*e.g.*, planetary rotation, orbital position).

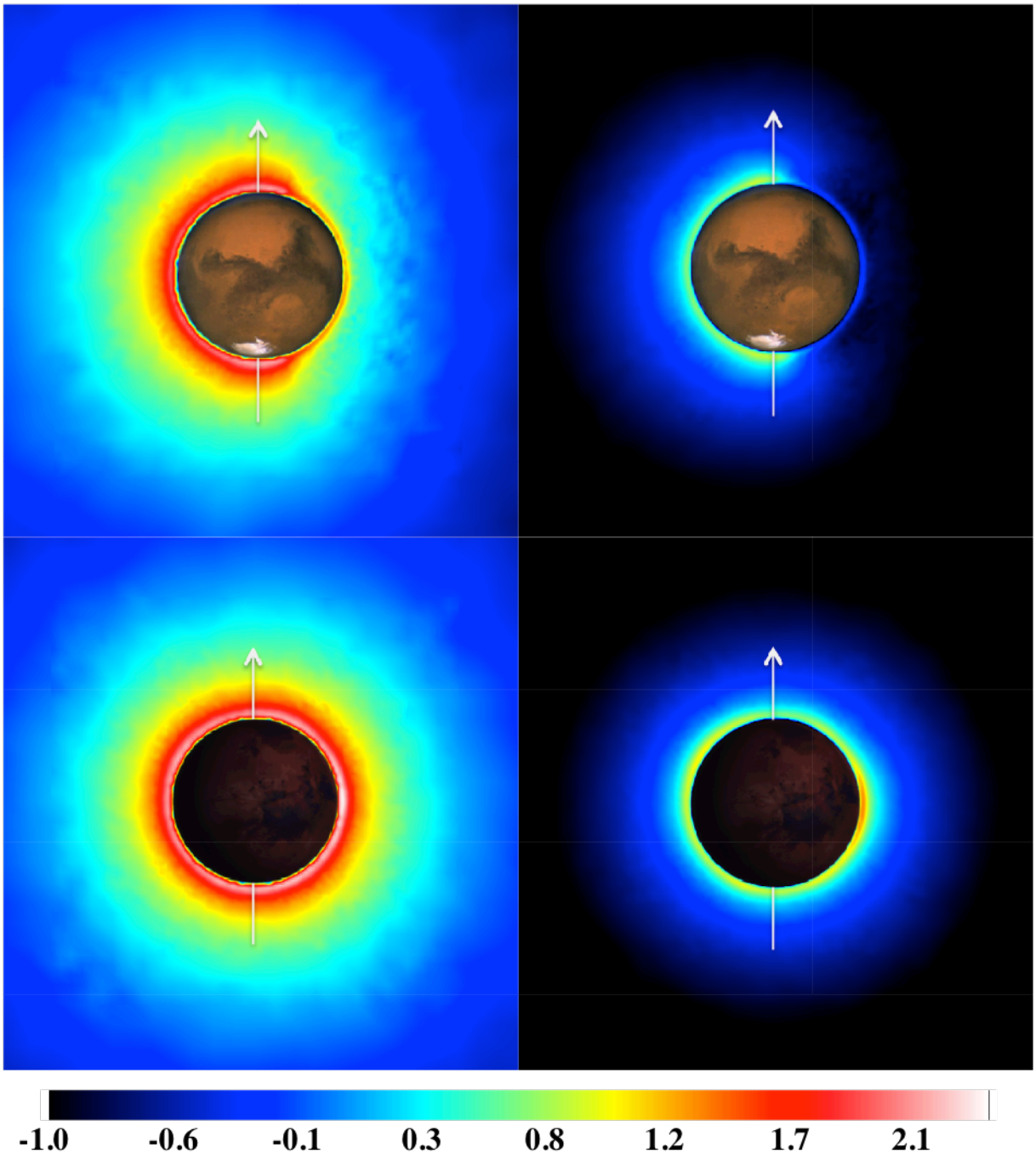

Figure 5.5. Sun-Mars meridian plane view of hot C density with the Sun on the left from (a, upper left) photodissociation of CO and (b, upper right) dissociative recombination of CO^+ and tail-to-Sun view of hot C density from (c, lower left) photodissociation of CO and (d, lower right) dissociative recombination of CO^+ for the solar low and equinox case.. The contours show the hot C density (cm^{-3}) in log scale.

One example of the characteristic features on the shape of hot corona related to the source reactions is shown in figure 5.5c and 5.5d. Unlike the near-symmetrical shape of hot corona (in tail-to-Sun view) in the photodissociation of CO case, dissociative recombination of CO^+ case displays a pronounced density enhancement on the morning terminator.

Figure 5.5 presents the hot carbon corona computed separately by each source reaction. It is logical to expect the overall shape of hot corona in the meridional plane to exhibit the nonaxisymmetric oblong shape. Since both source reactions are photochemical mechanisms, the density distributions from both reactions enhance globally over the dayside, decreasing exponentially with increasing distance from the planet. The sharp density gradients over the polar regions are shown where the hot density increases slightly near the terminators and decreases abruptly on the nightside. The production of hot carbon does not take place on the nightside, but the nightside hot population exists in the simulated results due to the hot carbon produced on the dayside, impacting the nightside and scattering back upward, or 'bouncing' as described by *Valeille et al.* [2009a]. The maximum hot carbon density produced by photodissociation of CO (figure 5.5a) on the dayside is ~3×10^2 cm^{-3} near the terminators. The density decreases by about an order of magnitude on the nightside. The dissociative recombination of CO^+ case also has similar diurnal variation but with the density maximum of ~1×10^1 cm^{-3} (figure 5.5b).

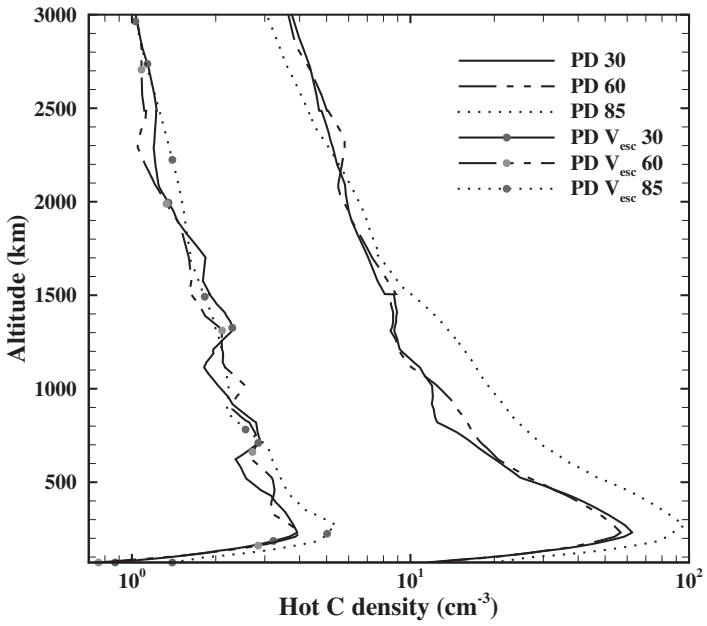

(a)

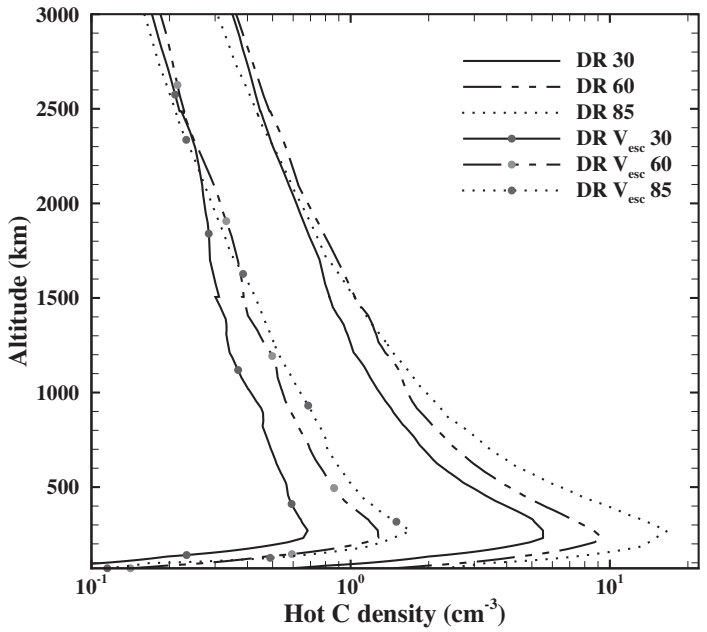

(b)

Figure 5.6. Density profiles of hot C (solid) and the fraction of hot C that have their velocity larger than the local escape speed (filled circle, V_{esc}) resulting from (a) photodissociation of CO, and (b) and dissociative recombination of CO^+ for different SZA (30° (solid), 60° (dash-dot-dot), and 85° (dotted)) for the solar low and equinox case. Hot C profiles are extracted North poleward (along the noon meridian) for the photodissociation of CO case, and along the equatorial west for the dissociative recombination of CO^+ case.

The structure of the hot carbon density profile at lower altitudes is affected mostly by the thermospheric winds and planetary rotation. Figures 5.6a and 5.6b show the density profiles of the hot carbon produced from photodissociation of CO and dissociative recombination of CO^+, respectively, for the different solar zenith angles. In each plot, the hot carbon density is calculated with two different settings for $V_{threshold}$; twice the local thermal speed as usual and the local escape speed specifically to obtain the fraction of the total hot carbon population. The hot density from both source reactions peaks above ~270 km altitude for the low solar activity and equinox case. The peak altitude of the hot carbon density increases from about 250 km to 300 km as the solar zenith angle increases since the altitude of the source peaks (thermal CO and CO^+) increases with solar zenith angle. The nascent hot carbon that exceeds the local escape speed is ~10% of the local hot carbon population near the peak altitude of hot carbon density for both source reactions.

Thermal atomic carbon is one of the minor neutral atoms in the Martian atmosphere. According to figure 5 in *Fox* [2004] (density profiles of the minor neutral species for the low solar activity model), the peak altitude of the thermal carbon density is at ~140 km altitude, and the density decreases to about 2×10^2 cm^{-3} at 400 km. Compared to the modeled hot carbon density, which peaks at around 250 - 300 km, the thermal C dominates the carbon population over hot C by more than about 2 orders of magnitude near 200 km. Since the thermosphere/ionosphere input model does not simulate thermal C, the thermal (cold) C profile is estimated by using the Chamberlain model [*Chamberlain*, 1963] (figure 5.7). As a parallel study of the total O density profile by *Valeille et al.* [2010a], figure 5.7 shows the altitude profiles of hot and cold C for the approximated transition region, where the C population makes transition from the cold to the hot dominated regimes. This transition region is considered to be

between 230 km – 900 km for the C population for the case considered in this work. The altitude of this region is expected to vary with solar activity or orbital position. The ratio of hot C to cold C densities is estimated to become over 1 above the altitude of about 550 km. Therefore, the total carbon population below about 500 km altitude is considered to be dominated by thermal C.

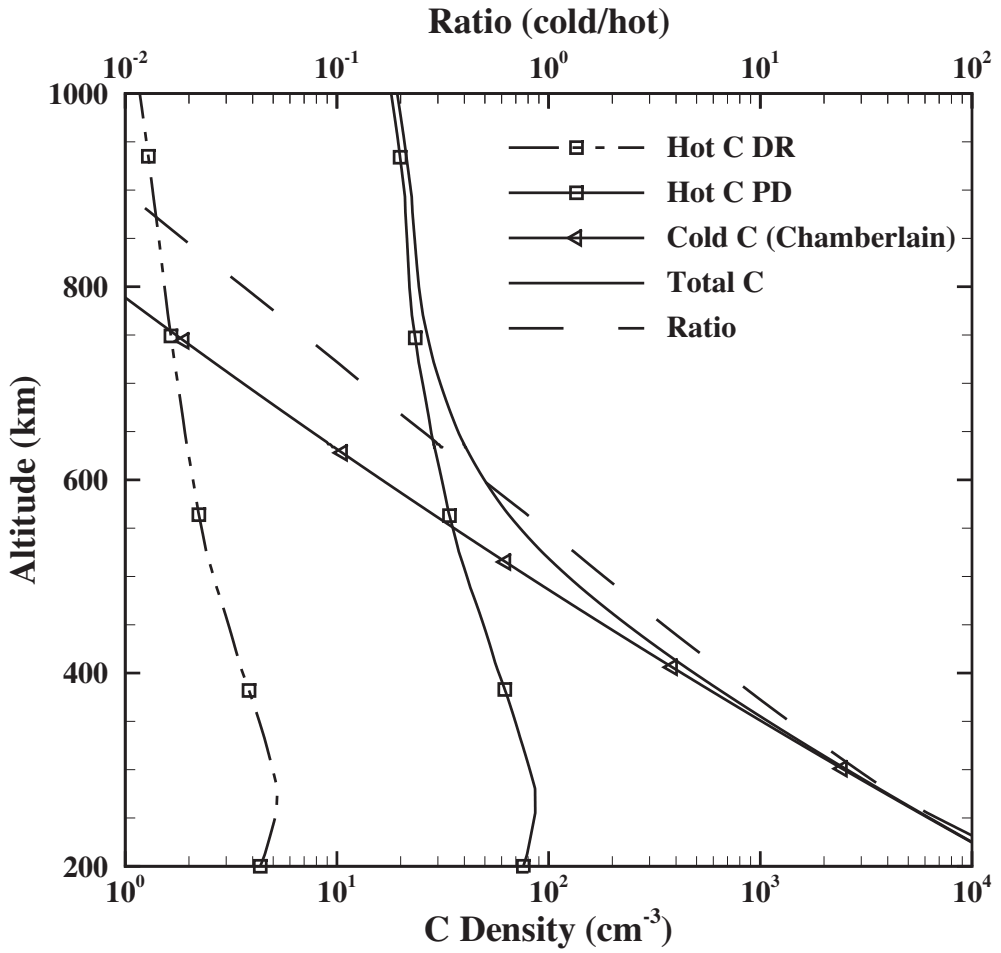

Figure 5.7. Total C (solid) density profile for the solar low and equinox case. Density profiles of the hot C produced from photodissociation of CO (solid, square) and dissociative recombination of CO^+ (dash-dot-dot, square) are extracted at SZA 60°. Thermal C (cold C) density profile (solid, triangle) is estimated by using the Chamberlain model. The cold C/hot C ratio is shown in black dash line.

Figure 5.8 presents the escape flux computed for each source reaction at 3 Mars radii as a function of solar zenith angle. Although hot carbon production does not take place on the nightside, the effect of gravity and the ubiquitously cumulative collisional interaction in the transitional region result in the escape flux over the nightside (bouncing effect).

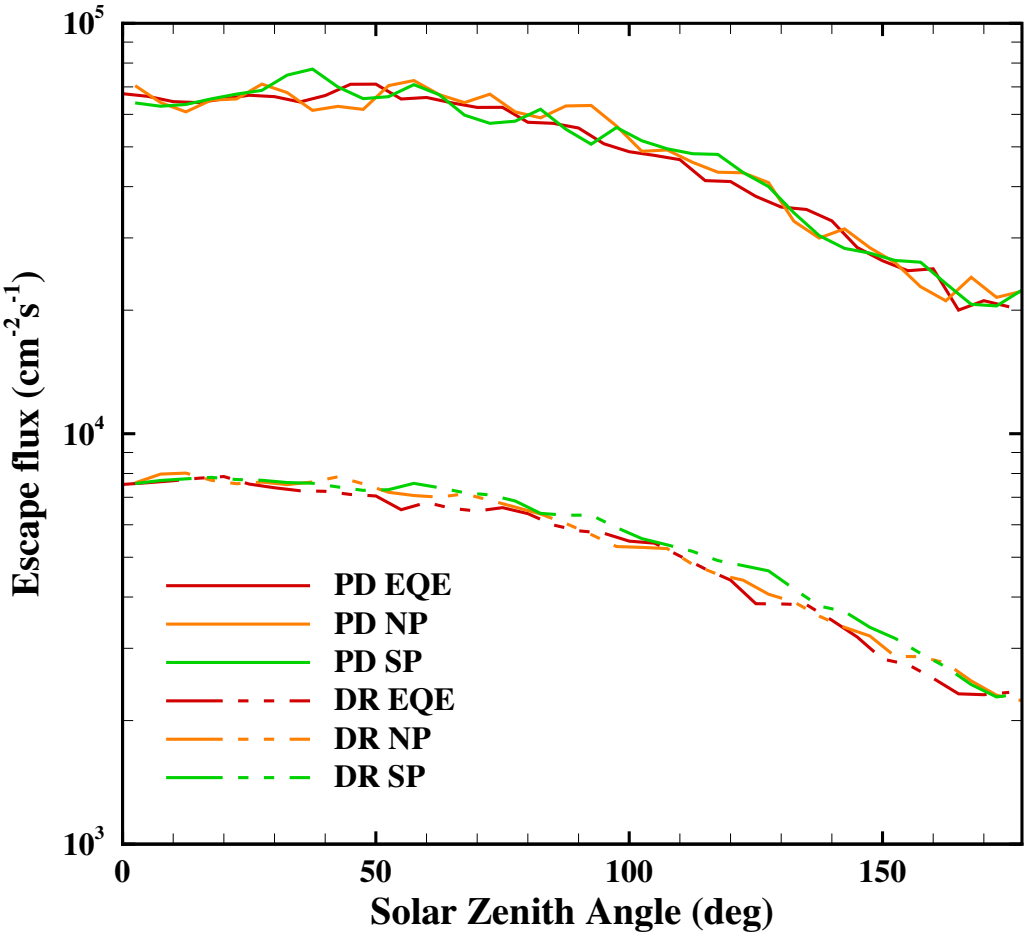

Figure 5.8. Escape fluxes of hot C produced by two sources, photodissociation of CO (solid) and dissociative recombination of CO^+ (dash-dot-dot), are calculated at different locations around the planet as a function of SZA at an altitude of 3 Mars radii. Computations have been done over the equatorial east (EQE, red), the North pole (NP, orange), and the South pole (SP, green).

Escape Flux (10^4 cm^{-2} s^{-1})[a]	Solar Zenith Angle (SZA)				
	30°	60°	90°	120°	150°
Photodissociation of CO	6.63	6.60	5.56	4.11	2.64
Dissociative recombination of CO^+	0.74	0.68	0.58	0.40	0.28

Table 5.1. Escape fluxes of hot carbon from two sources at different solar zenith angles at an altitude of 3 Mars radii.

[a] Fluxes are in 10^4 cm^{-2} s^{-1}, computed over the equatorial east direction.

Three different extreme locations are chosen to compute the escape fluxes: equatorial eastward, North poleward (along the noon meridian), and South poleward (along the noon meridian). Since the local parameters are averaged over a larger area as the distance from the planet increases, the interhemispheric variation is negligible in the computation. The tabulated escape fluxes (table 5.1) with respect to SZA in 30-degree increments show that the diurnal difference is about a factor of 3.2 for both source reaction cases. The effect of photodissociation mechanisms on the escape flux is about an order of magnitude larger than that of dissociative recombination.

The hot carbon corona is visualized in 3D in figure 5.9. The iso-surfaces at different altitudes exhibit the near-spherical shape of the distribution over the dayside and abrupt decrease over the terminators and nightside. The shape of iso-surface shows the lesser degree of the oblong appearance with the increasing distance from the planet.

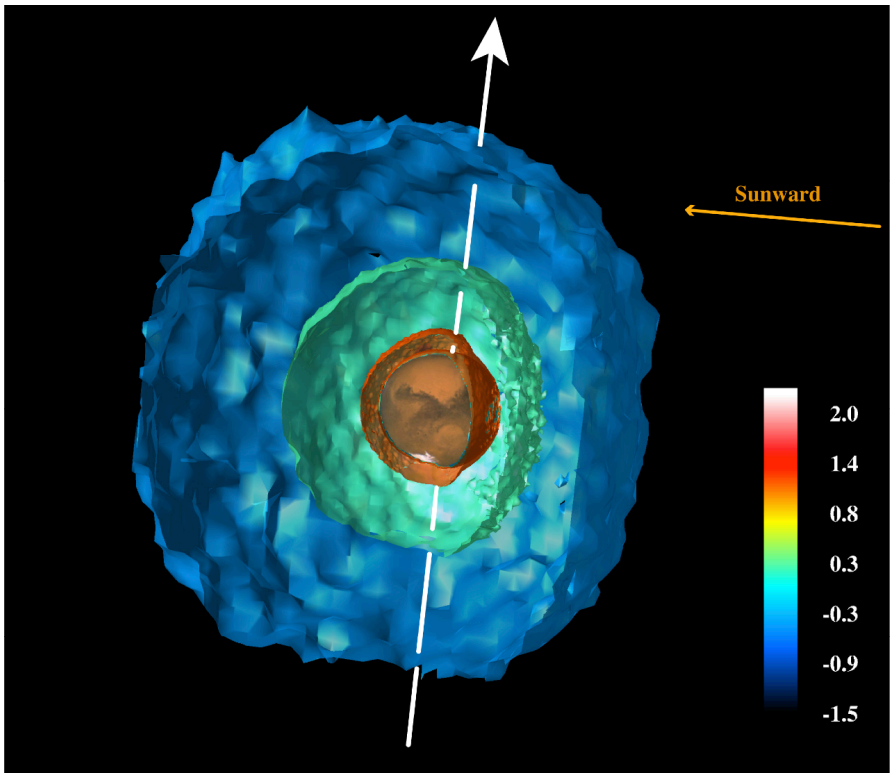

Figure 5.9. 3D view of hot carbon corona with the Sun in the direction in which the orange arrow points. The white arrow points to the North pole of the planet. Three iso-surfaces represent the log density of hot carbon density surfaces both from photodissociation of CO and dissociative recombination of CO^+. Iso-surfaces are at $\log_{10}$ (cm^{-3}) = -0.5 (~0.3 cm^{-3}), 0.2 (~1.6 cm^{-3}), and 1.2 (~15.8 cm^{-3}).

Chapter VI

Hot carbon corona

– Solar cycle and seasonal variability

In order to study the variation of the hot carbon corona for different solar cycle and seasons, two solar activity (low and high solar activities) and three seasons (aphelion, equinox, and perihelion) are pre-simulated by the atmospheric model. This chapter addresses the variability of the upper atmosphere and exosphere that is relevant to the production and thermalization of hot C. The global escape rates of C and model comparison will follow.

VI.1. Solar cycle and seasonal variability

In this study, the solar cycle and seasonal variability of the hot carbon corona are first simulated with the MTGCM (yielding thermosphere and ionosphere fields), utilizing parameters specifically chosen for the Martian seasonal and solar cycle conditions. The two solar cycle cases considered are for low (F10.7 = 70) and high (F10.7 = 200) solar activity conditions. The seasons are represented by three different orbital positions of Mars: aphelion ($L_s = 70°$), equinox ($L_s = 180°$), and perihelion ($L_s = 250°$) corresponding to summer, autumn, and winter in the northern hemisphere, respectively. The coupled MTGCM and Mars-AMPS simulations are categorized into five cases: perihelion solar low and high (PL and PH), equinox solar low and high (EL and EH), and aphelion solar low (AL). The solar cycle variability is effectively evaluated by a comparison between the solar low and high cases (EL and EH or PL and PH).

Since the aphelion case does not have a solar high condition, the seasonal variability is evaluated by a comparison of solar low cases, AL, EL and PL only. These cases are the same as those explored by *Valeille et al.* [2009b] for the variation of the hot oxygen exosphere during the current epoch.

VI.2. Description of background atmosphere

VI.2.1. Temperature and wind variation

As the F10.7 index increases, the magnitude of the neutral temperature increases, but the horizontal distributions of the low and high temperature regions do not change, for example, as shown in the EH (figure 6.1c) and EL (figure 6.1b) cases. According to *Bougher et al.* [1990, 1999, 2009], the Mars thermospheric circulation serves as an efficient thermostat that regulates the dayside temperature driven by solar EUV heating. Global winds play a vital role in modifying thermospheric temperature [*Bougher et al.*, 2000]. Upwelling diverging winds adiabatically cool the dayside, and subsiding converging winds heat the nightside. This effectively redistributes the heat in the day-night flow, reducing the enhancement of the diurnal contrast. The larger contrast seen in the contour plots on the dayside implies the faster response of the dayside temperature to the advance of the solar cycle, which increases the temperature by about 80 – 100 K, while the nightside temperature increases by about 40 – 50 K.

Much more than on Earth, the Martian seasons are defined also by the change in heliocentric distance, due to its highly elliptical orbit as well as its rotational axial tilt. Over the course of the Martian year, the solar EUV flux reaching the top of the thermosphere varies by about ±22% according to the axial tilt of ~25° [*Bougher et al.*, 1999]. As a result, the temperature and global circulation structures change significantly. The peak dayside (low SZA)

temperatures vary from about 180 K for the AL case (figure 6.1a) to about 230 K for the PL case (figure 6.1d). The high temperature regions are situated in the middle latitudes LT = 1000 for the AL case. For the EL case (figure 6.1b), the high temperature region expands to the morning and evening terminators and the high latitudes near the polar regions and emerges toward the southern hemisphere for the PL case with the highest temperatures located in the middle latitudes on both hemisphere. With the minimum solar flux and the largest heliocentric distance, the zonal and meridional wind gradients in the AL case are much weaker than those of the other seasons, due to the less pronounced day-night pressure gradient. As a consequence, diurnal temperature variation is about 80K for the AL case, while this variation is larger in the PL case, which it is about 120 K.

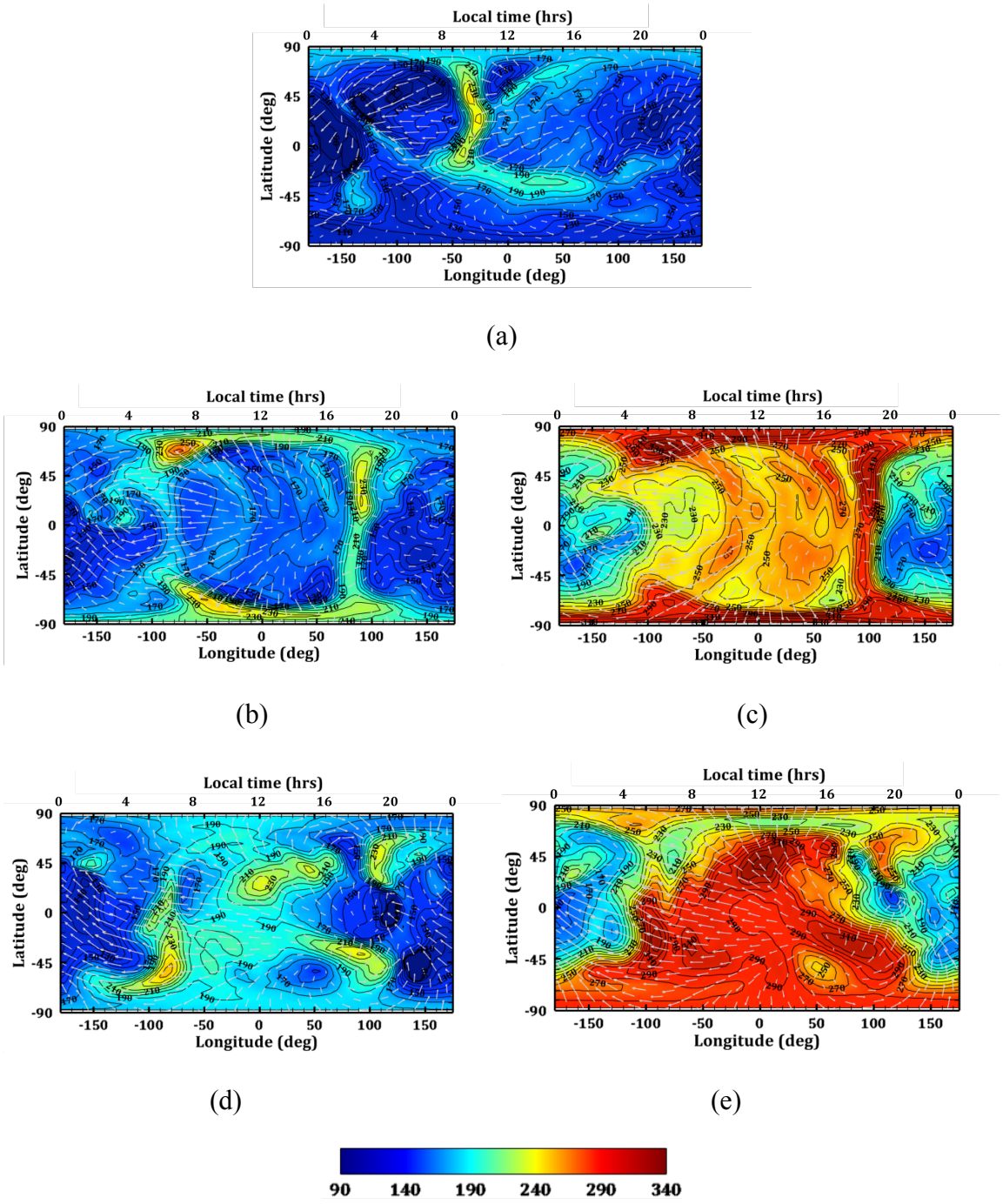

Figure 6.1. Neutral temperatures (T_n) for the (a) AL, (b) EL, (c) EH, (d) PL, and (e) PH cases. The effects of global circulation are indicated by the white streamlines. The contours show the temperatures in units of K.

VI.2.2. Neutral atmosphere variation / CO density distribution

CO_2 is the major neutral species in the Martian thermosphere up to an altitude of between ~180 – 220 km, depending on solar activity and season. As discussed in detail in *Lee et al.* [2014a] and in chapter 5, O becomes more responsive to the global atmospheric circulation than does CO_2, resulting in an enhanced O population on the nightside, where the convergence and downwelling of the circulation occur. CO is an important neutral species that also exhibits density enhancement on the nightside (like the O density). However, in general, CO responds more closely to the local background temperature distribution (like the CO_2 density). These different global responses from different neutral species uniquely define their own horizontal distributions, which are important for the overall structure and shape of the thermosphere, ionosphere, and hot corona.

Figure 6.2a shows the horizontal distributions of O, CO_2, and CO for the EL and EH cases at an altitude near 200 km. The CO density is spatially distributed in a pattern that combines features of both the O and CO_2 density distributions. For the low solar activity case, the maxima of the CO density are located near the polar regions on the morning terminator, while the minima are situated mostly on the nightside at low latitude region. When solar activity increases, the spatial distribution retains much the same pattern, but the whole thermosphere is enhanced by the solar EUV flux, resulting in an increase in the CO density of about a factor of 2.1 – 3.1.

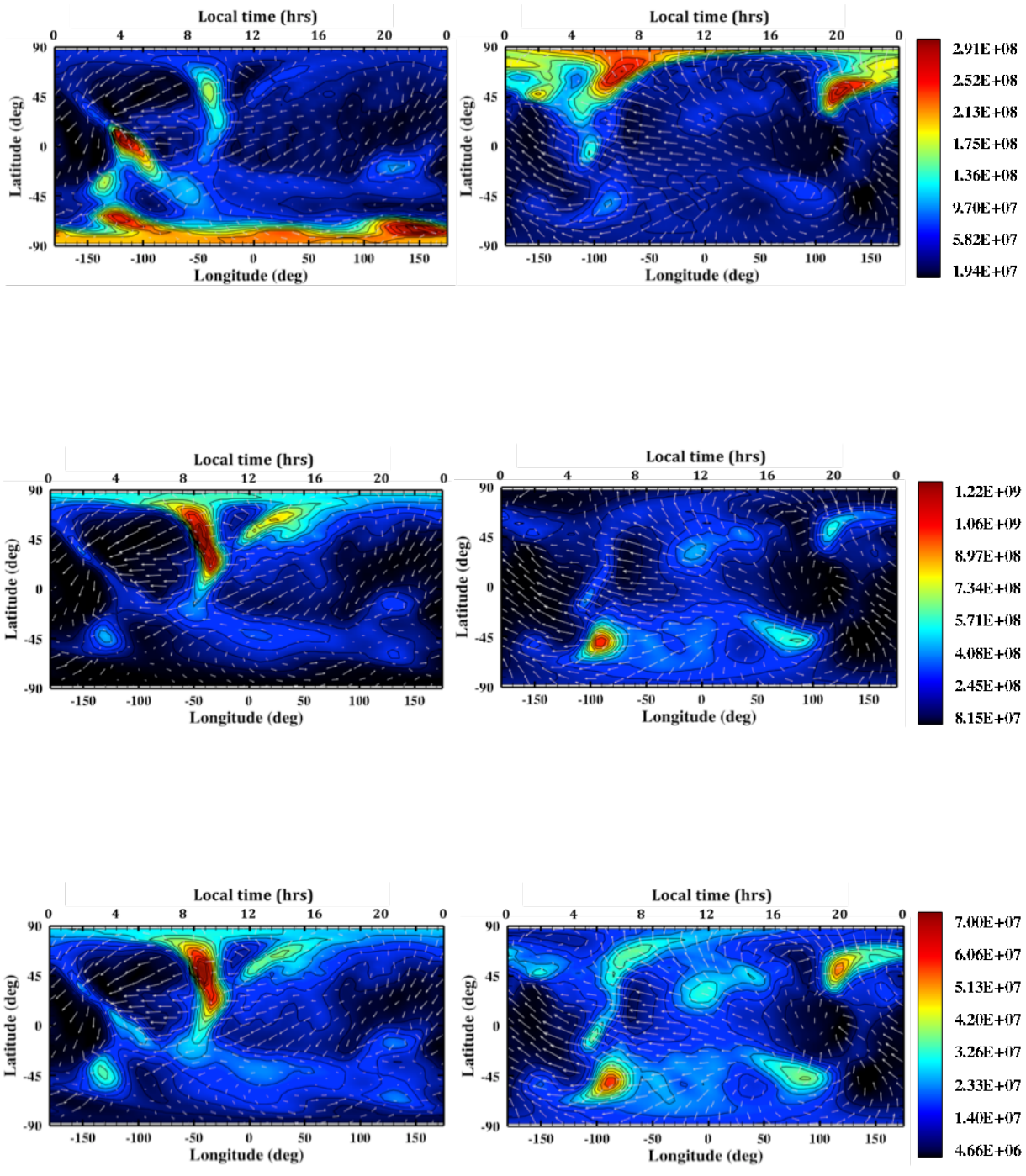
Local time (hrs)
0 4 8 12 16 20 0
Latitude (deg)
90 45 0 -45 -90
Longitude (deg)
-150 -100 -50 0 50 100 150
2.91E+08
2.52E+08
2.13E+08
1.75E+08
1.36E+08
9.70E+07
5.82E+07
1.94E+07
1.22E+09
1.06E+09
8.97E+08
7.34E+08
5.71E+08
4.08E+08
2.45E+08
8.15E+07
7.00E+07
6.06E+07
5.13E+07
4.20E+07
3.26E+07
2.33E+07
1.40E+07
4.66E+06

(a)

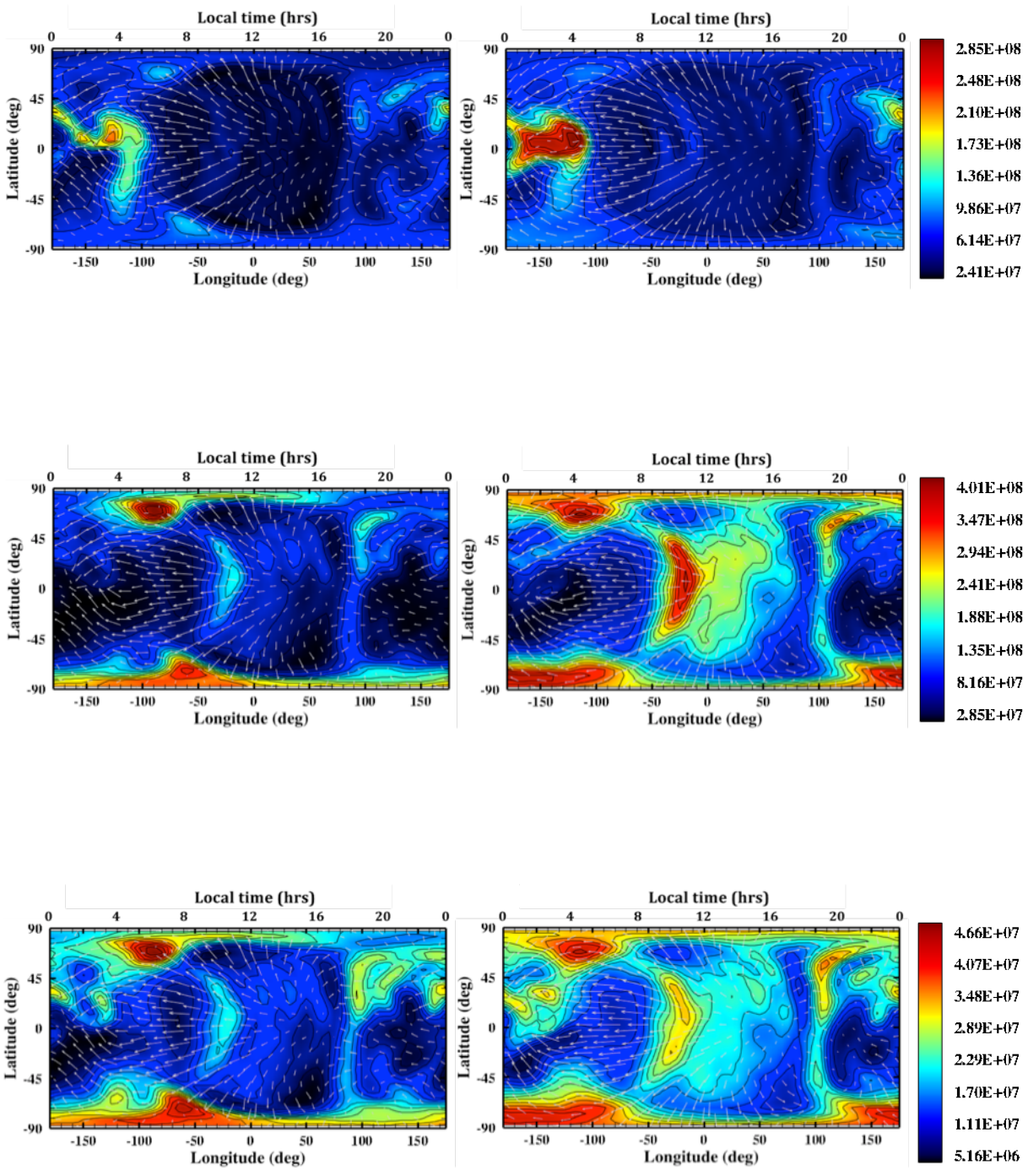

(b)

Figure 6.2. Thermal O (top), CO_2 (middle), and CO (bottom) density distributions for (a) the AL and PL cases, and (b) for the EL and EH cases.

The seasonal influence is quite strong on the spatial distributions of the neutrals. Two extreme cases, the AL and PL cases, for O and CO_2 are shown in Figure 6.2b. For the AL case, the O concentration reaches a maximum at the south pole, which is the winter pole during aphelion, while the CO_2 concentration has its maximum near the north pole. For the PL case, the O maximum is located near the north pole, the winter pole during perihelion, on the nightside, and the CO_2 maximum is on the dayside near the south pole. These characteristic special distributions of O and CO_2 also appear in the CO distribution pattern. The maxima and minima of CO_2 and CO are correlated in most of the places over the seasons.

Figure 6.3 shows the seasonal variation of the O mixing ratio, $O/(O+CO_2)$. The white streamlines indicate the atmospheric circulation (global winds). The overall bulk flow of the atmosphere is the summer-to-winter interhemispheric flow during both perihelion and aphelion, with an upwelling vortex circulation toward the summer pole. This flow converges in the winter polar region on the nightside. The adiabatic heating from this subsiding flow is dominant during perihelion, due to the stronger meridional winds, which results in the Martian thermospheric winter polar warming [*Bougher et al.*, 2006].

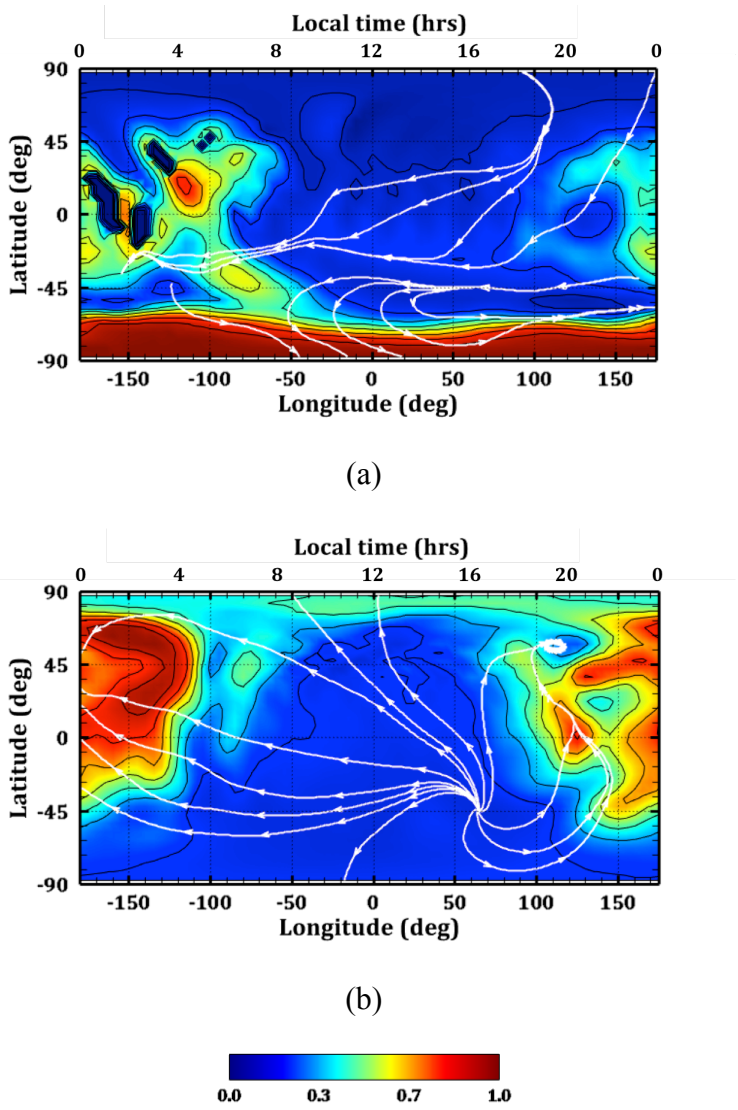

Figure 6.3. Thermal O mixing ratio, $O/(O+CO_2)$, for the (a) AL case and the (b) PH case. White streamlines indicate the global winds.

VI.2.3. CO^+ ionospheric peak and its distribution compared with O_2^+

The CO^+ ion distribution differs from that of the major ion, O_2^+, in several ways. The CO^+ ionospheric peak is located above an altitude of approximately 210 km and 240 km for low and high solar activity, respectively. Compared to the O_2^+ peak height (~135 km), the CO^+ density near its peak height is more sensitive to solar activity variation since the density peak is situated where the solar EUV radiation is more effectively absorbed by the background